Title
Modeling neutrophil chemotaxis in multiple chemoattractant gradients

Author
Erickson, Keith Allen

Publication Date
2005

Peer reviewed|Thesis/dissertation

Modeling Neutrophil Chemotaxis in Multiple Chemoattractant Gradients

by

Keith Allen Erickson

DISSERTATION

Submitted in partial satisfaction of the requirements for the degree of

DOCTOR OF PHILOSOPHY

in

Bioengineering

in the

GRADUATE DIVISIONS

of the

UNIVERSITY OF CALIFORNIA SAN FRANCISCO

and

UNIVERSITY OF CALIFORNIA BERKELEY

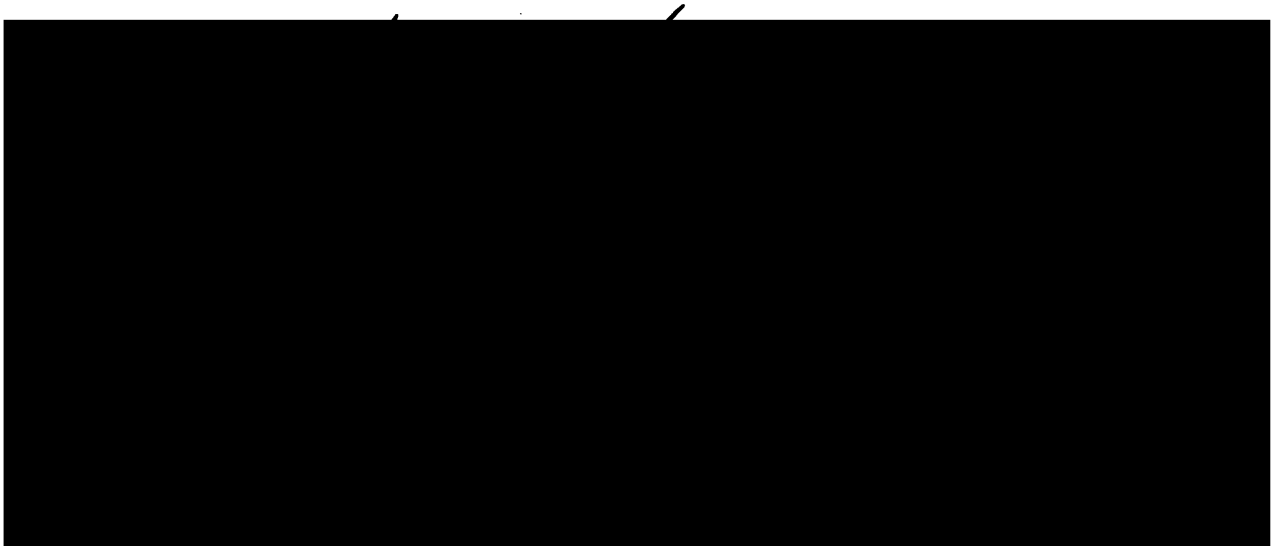

Degree Conferred: .....

Acknowledgments

I remember standing on a hill one sunny day six and a half years ago looking out over Berkeley and the San Francisco Bay knowing that this was the place for me. Not only is it one of the most beautiful and geographically diverse areas in the world, but the combination of the two UC schools makes it one of the most intellectually challenging. I have overcome many personal and professional obstacles and am grateful for every day of my stay here thanks mostly to the amazing people that have helped me along the way.

First among these people is my graduate advisor Adam Arkin. Like me, Adam has many interests and refuses to give up on any of them. He gave me tremendous freedom to falter and flourish, and through it all, his support was unwavering. He also attracted a diverse and brilliant group of people to his lab. Chris Rao is one of the most dedicated scientists I know. He provided tremendous assistance on this project, primarily by believing in me, and is the kind of scientist that I aspire to become. I enjoyed coming to the lab if for nothing else than to talk with Shilpa Shroff about science, politics or whatever. Sergey Plyasunov, my comrade-in-arms, provided patient explanations on stochastic principles over pho. I would like to thank Eric Alm for teaching me the art and strategy of the ancient masters. Gwyneth Terry, Alex Gilman, Robin Osterhout, and Timothy Ham were very entertaining.

Despite space constraints, Dan Fletcher welcomed me into his lab, exposing me to a rich array of experimental tools and his team of dedicated young scientists. Martijn van Duijn is a jack-of-all-trades, master trouble-shooter and deserves much credit for helping me get the experiments working. Joshua Shaevitz has a great sense of humor and a tremendous ability to break a problem down to the fundamentals. Sapun Parekh is a quick

learner and has a tremendous amount of focus. Allen Liu, Wendy Hansen, Wilbur Lam, Ovijit Chaudhuri, and Mike Rosenbluth have helped make my last year among the most enjoyable.

I am extremely lucky to have moved in with Christopher Hobart shortly after I arrived. My housemate for five years and best man, Chris exposed me to fine cuisine, accompanied me on several amazing road trips, and spent countless hours philosophizing with me. He also introduced me to Peter Gold. Pete, more than anyone, has brought me out of my shell and for that I am grateful. He introduced me to Latin America and officiated my wedding. I am going to miss you guys.

My family has provided an excellent foundation on which to pursue my academic endeavors. They have always been supportive and have demonstrated their love regardless of my difficulties. I hope that I have provided the same love to them.

Finally, I would like to thank my wife, AmyH. She has been extremely patient, moving to New York at my suggestion and setting up a forward operating base. We have lived apart for one and a half years and the greatest reward for me in achieving my doctorate is to spend the rest of my life with her.

Abstract

Neutrophils constitute the largest class of leukocytes and are the front line of cellular immune defense. They are able to sense and migrate up concentration gradients of chemoattractants in search of primary sites of inflammation in a process termed chemotaxis. Chemoattractants include formylated peptides, complement factors, and various chemokines. Each chemoattractant binds to a specific receptor that activates a number of responses including chemotaxis. While there is much information on the molecular interactions and signaling pathways that respond to these stimuli, how the pathways process multiple signals to effect migration in the appropriate direction is not understood. The primary motivation behind the work presented here is to understand the engineering rules by which neutrophils combine multiple signals to choose a direction to move and efficiently locate a target in a complex environment.

For this purpose, we have developed an assay system and novel image processing techniques, along with a modeling framework in which to compare the results. We used the micropipette assay for generating the gradients and tracked changes in cell densities over time. This represents the first use of the micropipette assay toward studies of neutrophil chemotaxis in multiple chemoattractant gradients. The modeling framework is based on an Ornstein-Uhlenbeck (OU) process which has been successfully used to describe neutrophil migration paths in uniform chemoattractant concentrations. We modified the OU process by including a term to describe chemotactic bias resulting from chemoattractant gradients. We assumed that this bias is the result of a vector sum of multiple gradients as sensed by neutrophils through their receptors. In developing the

model we compared experimental results and applied these results toward parameter estimation and model validation.

Using this framework, we were able to relate experimentally observable cell migration paths to the physical principles involved in receptor-ligand binding. Our main results quantify signal processing and prioritization based on binding parameters such as receptor quantities and dissociation constants. Overall, this dissertation represents a tight coupling of experimental and modeling techniques toward understanding how neutrophil chemotaxis has been engineered by evolution.

Professor Adam Arkin, Graduate Adviser

Table of Contents

List of Tables

List of Figures

Chapter 1

Background on Neutrophil Chemotaxis

1.1 Introduction

Chemotaxis is the directed movement of cells in response to a concentration gradient of a chemoattractant and plays an important role in many cellular processes including development, wound healing, angiogenesis, immunity, and metastasis. It enables amoebae of *Dictyostelium discoideum* to hunt bacterial prey or aggregate into multicellular fruiting bodies under starvation conditions. It is also used in the mating response of the budding yeast *Saccharomyces cerevisiae*. One area of particular importance in humans is the neutrophil chemotactic response to chemical signals released by invading bacteria or damaged cells. Neutrophils, the most abundant of the phagocytes in the innate immune system, rapidly attach to activated endothelial cells near sites of infection and migrate through the endothelial layer in a process termed diapedesis. Once in the tissue, neutrophils process and respond to a variety of diffusing and adherent signals to hunt and phagocytose their targets. The mechanisms by which neutrophils perform these functions likely involve hundreds of proteins and small molecules and thousands of reactions. The development and coordination of these reaction events has been engineered by evolution over millions of years to produce a robust response that is critical to host immune protection. Reverse engineering these mechanisms to gain a detailed understanding of how neutrophils perform their functions will require a wide range of biophysical, biochemical, and computational techniques. This dissertation

presents a modeling framework incorporating many different techniques toward reverse engineering the mechanisms that enable neutrophils to correctly process and respond to multiple chemoattractant gradients.

Before developing the modeling framework, we present in this chapter a concise review of the experiments and models that have moved us closer to an engineering level understanding of neutrophil chemotaxis. We begin with a brief discussion of the main observations and primary components of the chemotaxis network. We then review the experiments that have identified key players in the network and have highlighted their roles in regulating cell polarity, a requirement for chemotaxis. We follow this review with a presentation of models of signal transduction, focusing on how these models have assisted in uncovering the mechanistic details. We then discuss phenomenological models and the link between these high level descriptions of chemotaxis and the lower level biochemistry. Finally, we turn to the work presented in this dissertation, discussing how it advances an engineering level understanding of neutrophil chemotaxis. The main questions that we address include: What are the control laws that allow a cell to use gradient information to find a target? For multiple signals representing different target priorities, what are the optimal ways a cell can read these signals to efficiently find the target in complex environment? How do the molecular networks of signal transduction components implement a controller that is necessary and optimal?

1.2 Main Observations

Figure 1.1 displays a polarized cell migrating in response to a chemoattractant. In their response, neutrophils develop a distinctive polarized morphology with a wide actin-

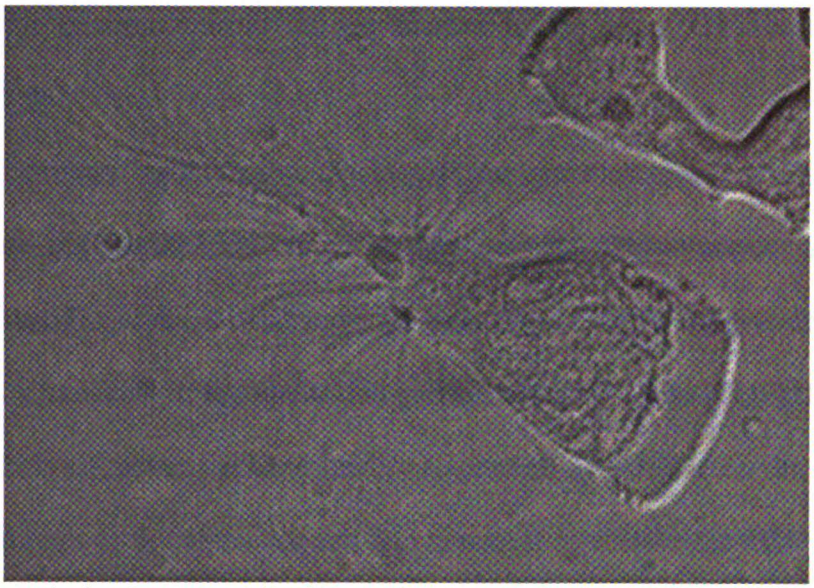

Figure 1.1: A polarized neutrophil-differentiated HL-60 cell migrating in the direction of the lower right corner of the frame.

rich leading edge, or lamellipod, in the front and a contractile tail, or uropod, in the back. In a gradient of chemoattractant, a neutrophil aligns its polarity with the gradient; if the concentration is uniform, the polarity is oriented in a random direction. This response is initiated by binding of chemoattractant molecules to receptors embedded in the cell membrane and displayed on the surface. Chemoattractants include formylated peptides such as fMLP, secreted by infecting bacteria, complement factors such as C5a, which opsonize foreign particles, and chemokines such as interleukin-8 (IL-8) and the lipid leukotriene B4 (LTB4), which are secreted by activated host cells. These signals play different roles in guiding neutrophils through the blood vessel wall and to their targets. Each chemoattractant binds to a more or less specific receptor that activates a variety of responses including chemotaxis. These receptors all fall into an important category of receptors known as G protein-coupled receptors (GPCRs). It is estimated that 3% of all genes in the human genome encode GPCRs [Bourne and Meng, 2000] and a large

majority of all pharmaceuticals on the market today target GPCRs in some way [Lefkowitz, 2004].

Two common traits shared by all GPCRs are that they consist of 7 helical transmembrane regions and they bind to and activate heterotrimeric G proteins. G proteins consist of an alpha, a beta, and a gamma subunit. In the inactive form, the alpha subunit binds a molecule of the nucleotide guanosine diphosphate (GDP). In response to binding of chemoattractant, a conformational change is induced in the receptor that propagates through to the alpha subunit and causes it to release the GDP. The GDP is quickly replaced by a molecule of guanosine triphosphate (GTP) which is present in much higher concentrations inside the cell. The receptor thus acts as a guanosine nucleotide exchange factor (GEF). The G protein is subsequently released from the GPCR and dissociates into alpha and beta-gamma subunits which then activate a wide variety of downstream effectors. The signal is shut off when the alpha subunit (a GTPase) cleaves the GTP into GDP and phosphate and rebinds to the beta-gamma subunit and GPCR, thus completing the cycle. Several of the downstream effectors activated by the alpha and beta-gamma subunits propagate signals that converge on the actin cytoskeleton, inducing polarity and regulating cell migration and chemotaxis.

Observations made almost 30 years ago by Sally Zigmond showed that neutrophils could orient correctly in gradients as shallow as a 1% difference in chemoattractant concentration across their bodies [Zigmond, 1977]. Optimal gradient detection occurs when the mean concentration is approximately equal to the receptor dissociation constant. Further observations showed that correct orientation occurs over a range of concentrations that correspond to binding to a saturable receptor [Zigmond and

Sullivan, 1979]. The level of orientation was observed to be proportional to the difference in the number of bound receptors across the cell after correcting for receptor down-regulation [Zigmond, 1981]. Once polarized, neutrophils display an increased sensitivity in the front and a decreased sensitivity in the back [Zigmond et al., 1981]. Rather than reforming the leading edge when exposed to a change in the direction of the gradient, neutrophils migrate in wide U-turns to point their existing leading edge up the gradient. These observations led to many questions that are still being explored today: How does a neutrophil transduce a shallow external chemoattractant gradient into a dramatic internal gradient of actin and myosin? How does a neutrophil maintain a sensitive front and an insensitive back and still manage to detect small changes in the direction of a chemoattractant gradient?

1.3 The Chemotaxis Network

Cell migration has been described as a continuous cycle of three main occurrences [Alberts et al., 2002]. First, actin polymerization against the membrane at the leading edge of the cell causes a lamellipodial protrusion that extends the cell forward. Second, adhesive contacts are formed between the substratum and the newly extended lamellipod. Finally, contraction of myosin II along actin filaments at the trailing edge pulls the cell forward and releases focal adhesions from the back of the cell. These events are tightly coordinated and highly regulated, enabling neutrophils to migrate rapidly to sites of infection.

Recent experiments using human neutrophils, *Dictyostelium discoideum*, and HL-60s, a myeloid leukemia that can be differentiated into a neutrophil-like state [Collins et

al., 1977; Hauert et al., 2002], have identified aspects of the chemotaxis network that are responsible for pointing cells in the appropriate direction and regulating their motility. We present here a brief review of the key experiments that have highlighted these components. The interested reader is referred to a number of excellent reviews for more detailed information [Devreotes and Zigmond, 1988; Parent and Devreotes, 1999; Rickert et al., 2000; Devreotes and Janetopoulos, 2003; Ridley et al., 2003].

What are the initial components of the chemotaxis network that cause polarization? Chemoattractant receptors and G proteins tagged with green fluorescent protein (GFP) maintain a uniform distribution around the cell during chemotaxis [Xiao et al., 1997; Servant et al., 1999]. Several proteins containing pleckstrin homology (PH) domains show strong asymmetric localization during chemotaxis [Parent et al., 1998; Meili et al., 1999; Servant et al., 2000]. These proteins reside in the cytoplasm of unstimulated cells and are transiently localized to the inner leaflet of the plasma membrane in cells exposed to uniform chemoattractant concentrations. Once these transients have decayed, or in response to stimulation with chemoattractant gradients, these proteins preferentially localize to the leading edge [Postma et al., 2003]. This localization is independent of actin polymerization since it still occurs in cells exposed to latrunculin-B, a toxin that sequesters monomeric actin [Parent et al., 1998; Servant et al., 2000]. Localization does depend, however, on the activity of one or more Rho GTPases [Servant et al., 2000]. The Rho GTPases Rac, Cdc42, and Rho are important mediators of signaling to the actin cytoskeleton [Xu et al., 2003]. It also depends on the activity of phosphatidylinositol (PI) 3' kinase (PI3K) as indicated by studies using *pi3k*-null *D. dictyostelium* mutants or the PI3K inhibitor LY294002 [Servant et al., 2000; Funamoto et

al., 2001]. Activation of PI3K leads to production of the phospholipid PI 3,4,5-triphosphate (PIP3) in the plasma membrane, which is bound by PH domains. Thus PI3K and its lipid product appear to be the initial components of the chemotaxis network that display polarity. But how is this polarity generated and how is it regulated?

Evidence suggests that the reciprocal activity of PI3K and the PIP3 phosphatase, PTEN, regulate polarization of PIP3 [Iijima and Devreotes, 2002; Funamoto et al., 2002; Iijima et al., 2004; Janetopoulos et al., 2004; Li et al., 2005]. In an unstimulated cell, PTEN is uniformly distributed on the inner leaflet of the plasma membrane, bound to PIP2 through an N-terminal binding motif, while PI3K resides in the cytoplasm. In response to a chemoattractant gradient, PTEN localizes to the back and sides of the cell where it inhibits production of PIP3, while PI3K moves to the leading edge and produces PIP3. The resulting polarization of PIP3 is further amplified by a positive feedback loop that acts through PI3K and one or more Rho GTPases [Weiner et al., 2002]. The distribution and activity of PTEN are regulated by RhoA and its downstream effector RhoA-associated kinase (Rock) [Li et al., 2005], which have been shown to regulate myosin contraction at the trailing edge of migrating cells [Xu et al., 2003]. But what causes PI3K and PTEN and their mediators to develop this reciprocal activity?

The data indicate that there are divergent, opposing "frontness" and "backness" signals that are generated in chemotactic cells in response to a chemoattractant gradient [Xu et al., 2003]. The frontness signal acts through the Gi G protein, PI3K and PIP3, Rac and F-actin, and the backness signal acts through the G12 and G13 G proteins, Rho, Rock, and myosin II. The protrusive and contractive structures are functionally incompatible which causes them to segregate into separate domains in the front and back

of the cells, respectively. The stability of the leading edge is regulated by Cdc42 [Srinivasan et al., 2003]. Inhibition of PI3K and actin polymerization [Wang et al., 2002], or Rho and Rock activity [Xu et al., 2003] disrupts the segregation of these two signaling pathways, leading to cells that cannot polarize as effectively and migrate in jerky trajectories.

Multiple chemoattractant gradients

In vivo, neutrophils are often confronted with complex and conflicting arrays of chemoattractant signals emanating from endothelial cells lining the capillary wall, activated cells near sites of inflammation or sources of inflammation. The response to these signals depends on where they converge in the biochemical processing machinery. In many cases, the response arises from a simple summation of the signals [Foxman et al., 1997]. Neutrophils have been shown, however, to prioritize chemotactic signals such as fMLP by migrating up gradients of these chemoattractants against gradients of IL-8, LTB4, or C5a [Foxman et al., 1997; Campbell et al., 1997; Foxman et al., 1999; Heit et al., 2002]. Although this prioritization may be attributable to a weighted sum of the signals, as explored in more detail in Chapter 4, several alternative hypotheses have been advanced.

One set of experiments demonstrated that the response to fMLP is generated along a MAPK pathway, whereas the response to IL-8 is generated along a PI3K pathway [Heit et al., 2002]. Activation of the MAPK pathway led to a reduction in the level of phosphorylation of the signaling protein Akt generated by the PI3K pathway. In the presence of fMLP, IL-8, and a MAPK inhibitor, however, Akt phosphorylation was greater than with IL-8 alone. The presence of IL-8 also enhanced migration toward

fMLP, suggesting further interplay between these pathways. The role of Akt in chemotaxis is currently unclear, and it may serve only as a read-out of up-stream processes. In contrast, observations on HL-60 cells showed sensitivity of fMLP-generated chemotaxis to PI3K inhibitors [Wang et al., 2002]. Richardson et al. (1995) showed that the receptors for IL-8 (IL8R) and C5a (C5aR) are phosphorylated in response to fMLP while the formylated peptide receptor (fPR) is not phosphorylated in response to IL-8 or C5a. Receptor phosphorylation has been demonstrated to lead to desensitization in other G protein-coupled receptors, such as the β-adrenergic receptor [Lefkowitz et al., 1992], but does not seem to play a role in chemotaxis. Interestingly, the results of Richardson et al. also show that the Ca^{2+} mobilization response is cross-inhibited between all three chemoattractants. Calcium, however, has been shown to be unimportant for chemotaxis [Zigmond et al., 1988]. The results outlined here suggest several interesting questions regarding the processing machinery for different signals and cellular functions. How does this machinery enable a cell to efficiently find a target? How does signal prioritization occur and how might it be different for other responses that are important for neutrophil function? What are the control laws that govern these processes and how are they implemented?

1.4 Models of Signal Transduction

Many models have been created that are quite useful in shedding light on the inner workings of the neutrophil chemotaxis machinery. These models take a bottom-up approach, offering the detailed, low level engineering descriptions similar to those that one might find for a car to describe the operation of the cooling system or carburetor.

They catalog key experimental observations, providing a platform on which to compare future mechanistic models and hypotheses. They also enable a simple exploration of the interplay between controllable and observable variables that can be useful during experimental design.

Adams et al. (1998) describe a deterministic model that includes receptor desensitization and G protein activation to explain experimental observations regarding ligand binding and actin polymerization dynamics such as peak concentrations and response times. Using a few dozen rate parameters obtained from the literature, they fit the model to the responses by adjusting six remaining parameters. The model is analyzed to attempt to validate the hypothesis that a percentage of the receptors exist in a state pre-bound to G proteins. They could not, however, get values for the six parameters that led to model agreement with all of the experimental observations and instead had to make 'compromise' fits. This compromise indicates that either their hypothesis or the parameters they obtained from the literature are incorrect. Nevertheless, it highlights one of the key difficulties in modeling: parameter estimation. Often these parameters are obtained from studies on different types of cells under widely different conditions. Lauffenburger and Linderman (1993) discuss several methods for minimizing some of these errors, using thermodynamic relations, for instance, to account for temperature effects on the rate parameters, but often the only way to guarantee good estimates is through the judicious combination of models and experiments under relevant conditions that isolate the parameters.

Riccobene et al. (1999) highlight another difficulty in modeling cellular responses to ligands. They use a model similar to that of Adams et al., focusing on the ligand-

specific rates of receptor desensitization and conformational selectivities to explain dose-response curves for the alpha-adrenergic, mu-opioid, and dopamine D_1 receptors of several species. Their results suggest that full or partial agonists and antagonists differ predominantly in their conformational selectivities. The difficulty arises when they try to model the effects of two different formylated peptides on the oxidant production response in human neutrophils. The independently measured parameters do not lead to agreement between their model's prediction and experimental observations. While they admit that temperature effects may play a role, they offer up the possibility that downstream mechanisms are responsible for the discrepancy. In the models discussed so far, these mechanisms are largely ignored. These investigators use a series of nonlinear hyperbolic functions, or stimulus response chains [Trzeciakowski, 1996], to represent the downstream signaling cascade and clear up the disagreement. These chains, however, are not mechanistic and neglect potentially important dynamics such as feedback.

Both of the models discussed above do not account for spatially segregated events and are thus unable to describe polarization and chemotaxis observed in migrating neutrophils. The models that do account for polarization make a number of simplifying assumptions regarding the intracellular environment. Although often unstated, they mainly consider the components of interest to exist within well-mixed, not very concentrated aqueous solutions.

Rather than deal with the actual biochemical mechanisms, Meinhardt (1999) first postulates a set of reactions that lead to key behaviors observed in eukaryotic chemotaxis. These behaviors include a sensitivity to signal asymmetry that is independent of the absolute concentration of signal, adaptation to changes in the signal orientation, and

formation of polarization in the absence of signal. The reactions include a self-enhancing activator, providing amplification, coupled to a globally-diffusing inhibitor, providing adaptation, and a local inhibitor with a longer time constant, providing sensitivity to directional changes. This set illustrates a minimal realization of the observed behaviors. The actual biochemical mechanisms behind the behaviors must agree with this set of reactions. Indeed, many of the models that have come out since, that deal specifically with gradient sensing and biochemical polarization do in fact agree with this minimal realization.

Narang et al. (2001) base their model of polarization on phosphoinositide dynamics. Inositol, the global inhibitor, stimulates the reduction in membrane phosphoinositides, which act as the self-enhancing activator by stimulating their own production, amplifying the external asymmetry. Local inhibition occurs via depletion of phosphoinositide precursors in the endoplasmic reticulum. These investigators show that the shape of the peak in membrane phosphoinositides on the up-gradient side of the cell is invariant to different external signal concentrations and relative gradients but does depend on the production and decay rates. Slower decay produces a broader peak and leads to increased sensitivity of the cell to smaller gradients. Postma and Van Haastert (2001) formally define the ability of a second-messenger to amplify a gradient based on its dispersion range. Small dispersion ranges, resulting from either low diffusivities or high decay rates, provide greater amplification. Based on available evidence, they suggest that membrane lipids, such as phosphoinositol, fit the criteria for this second messenger. Further amplification is achieved through binding and activation of a diffusive component that further stimulates production of second messenger. Sensitivity to ever

smaller gradients can occur by including additional diffusing second messenger stimulators, similar to the stimulus-response chains discussed above. Global inhibition occurs via depletion of the first diffusive second messenger stimulator. While these authors do not discuss sensitivity to directional changes in the gradient, they do incorporate receptor-ligand complexes in the activation of the second messenger, thus preventing signal-independent amplification. Levchenko and Iglesias (2002) have incorporated a specific circuit-breaking mechanism in their model using a substrate supply-based positive feedback to prevent signal-independent amplification. The readout, membrane-bound PIP3, leads to production of its substrates PIP and PIP2 through small G proteins such as the Rho GTPases. In the presence of a chemoattractant gradient, the substrates amplify the PIP3 gradient. When the gradient is absent, production of PIP3 is halted, and its substrates gradually decay. Global inhibition occurs via the rapid diffusion of the PIP3 phosphatase, PTEN. This model led to experiments in *D. discoideum* showing that fluorescently labeled PTEN is distributed uniformly throughout the membrane except in the lamellipod, where it is excluded [Iijima et al., 2002; Funamoto et al., 2002]. Recent evidence shows a similar role for PTEN in neutrophils [Li et al., 2005]. Rappel et al. (2002) model a temporal mechanism whereby the side of the cell that is exposed to chemoattractant first becomes the leading edge. They use three membrane states: quiescent, activated, and inhibited. Quiescent membrane becomes activated in response to an external signal, leading to production of an internal signal that diffuses through the cell and causes quiescent membrane to become inhibited. There is no polarization in uniform external concentrations, but gradients lead to an asymmetry that is caused when the internal diffusive element inhibits membrane at the trailing edge before the external

signal activates it. Based on these results, the authors suggest an experiment in which two signals are introduced on opposite sides of the cell at different times. If this time difference is large, polarization occurs; if it is small, polarization is prevented.

All of the models outlined above present different instantiations of the same basic behaviors discussed by Meinhardt (1999). While Narang et al. (2001) and Levchenko and Iglesias (2002) focus more on mapping these mechanisms onto the biochemistry, the others highlight general principles regarding biochemical polarization. Narang's model is the only one that includes receptor dynamics. None of these models account for observations related to the physical migration of neutrophils such as persistence times and U-turns. They also do not account for random polarization in a uniform chemoattractant field, or for neutrophil response to multiple chemoattractant signals. The physical and molecular basis of a neutrophil's ability to sense multiple cues, decide on which direction to move, and actuate the decision through polarization and other mechanical processes have become far clearer in recent years, and the recent models of amoeboid chemotaxis have been helpful in suggesting control laws by which the cell might process chemical cues and generate a response.

1.5 Phenomenological Models

The models presented in this section differ from those presented above in that they mostly ignore the inner workings of the biochemical machinery and take a top-down approach, focusing on the overall behavior of cells or populations of cells. These models are the high level engineering descriptions that show the expected direction of migration based on phenomenological parameters such as the random motility coefficient (similar

to a diffusivity) for a population of cells, or cell speed and persistence time for individual cells. An excellent treatise exists on this work that also describes details on linking the two levels of models [Lauffenburger and Linderman, 1993].

One of the most widely used mathematical models of chemotaxis, derived from statistical arguments, uses partial differential equations to describe the density of a population of cells [Keller and Segel, 1971]. The random motility coefficient μ, describing the cell diffusivity, and the chemotaxis coefficient χ, describing the effect of a chemoattractant gradient on the flux of cells, were introduced in this work and have served as standard measures ever since. Attempts have been made to improve and expand on this model and, in general, make it more applicable to experimental results [Alt, 1980; Othmer et al., 1988]. Several notable studies have developed each of the measures to relate them to individual cell migration parameters such as speed, persistence time, and chemotactic index, and even mechanistic parameters such as receptor numbers and dissociation constants [Tranquillo et al., 1988; Rivero et al., 1989; Farrell et al., 1990]. The persistence time describes the average time a cell spends moving in one direction and the chemotactic index is the ratio of the distance a cell migrates up a gradient to the total path length of the cell.

Moghe and Tranquillo (1994) go even further in linking the two levels of models by specifically modeling stochasticity in receptor dynamics to explain the behavior of neutrophils as they migrate randomly in uniform concentrations of chemoattractant or display biased random walks in gradients. These dynamics include multiple-affinity states between receptors and chemoattractants, as well as receptor internalization and recycling. As with all models, certain simplifying assumptions are made: the cell

maintains a distinct polarity, migrates at a fixed speed, and has a leading edge that is separated into two compartments. Turns in the direction of migration are made according to the difference in concentration of a downstream diffusive component between the two compartments, multiplied by a sensitivity factor. The model is analyzed to show the dependence of observations such as persistence time to the rate constants behind the receptor dynamics and the level of noise in the sensory system.

An Ornstein-Uhlenbeck (OU) process is a stochastic model describing Langevin's Brownian motion and has been used successfully to describe the migration paths of individual cells [Dunn, 1983; Stokes et al., 1991; Ionides et al., 2004]. This model uses two terms to describe a change in the velocity of a cell: one for random accelerations and another for decay in the movement velocity. The position of the cell is found by integrating the velocity. The two parameters in the OU process (one for each term) are related to the speed and persistence time via simple equations. Stokes et al. (1991) expanded on the OU process by including a third term in the description of the change in velocity that accounts for chemotactic bias. They assumed that this bias was proportional to the spatial gradient of bound receptors across the cell. The proportionality constant is called the chemotactic responsiveness. They simplified this model further by assuming that the number of bound receptors is linearly proportional to the chemoattractant concentration. They then estimated the two parameters in the original OU process by fitting an equation derived from the OU process that describes the mean-squared displacement of a cell [Doob, 1942] to experimental data collected from observations of microvessel endothelial cells migrating in uniform chemoattractant concentrations. They

estimated the chemotactic responsiveness by comparing the results of simulations of their model to experimental observations of cells migrating in gradients of chemoattractant.

1.6 Dissertation Overview

In this chapter, we have presented a concise review of the experiments and models that have moved us closer to an engineering level understanding of neutrophil chemotaxis. As discussed, many of the signaling components have been identified and a number of lower level models have revealed potential ways in which these components may be interconnected. Phenomenological models have made important advances in linking these lower level mechanisms to observations regarding neutrophil migration behavior. Nevertheless, fundamental questions remain: What are the control laws regulating neutrophil chemotaxis? How are multiple signals processed and prioritized? How are these functions implemented in the signal transduction network?

The work presented here focuses on understanding how neutrophils process and prioritize multiple signals. To do this, we expand on the model developed by [Stokes et al., 1991] in two important ways. We first relax the assumption that the number of bound receptors is linearly proportional to the chemoattractant concentration. We use a model of receptor-ligand binding and account for the gradient of bound receptors across the cell over a wide range of chemoattractant concentrations. We assume that spatial polarization occurs in response to this gradient. This model enables us to explore the effects on cell migration caused by shallow chemoattractant gradients, different values for the receptor-ligand binding parameters, and receptor saturation. For the second expansion of the model, we modify the chemotactic bias term to account for two chemoattractant

gradients. As discussed in greater detail in Chapter 4, we assume that the chemotactic bias is the result of a simple vector sum model of signal integration. This assumption enables us to explore the effects of the relative values of the receptor-ligand binding parameters for each chemoattractant as well as the spatial positioning and orientation of the two gradients. The primary goal of this work is to develop a modeling framework in which to explore hypotheses about how neutrophils process and respond to multiple chemoattractant gradients. As such, we develop and present experimental methods using the micropipette assay at each step that are useful for estimating model parameters. We show how the micropipette assay is superior to previous assays for studying chemotaxis to multiple chemoattractant gradients. We also perform simulations using parameter estimates and compare and contrast experimental and simulation results.

We present in **Chapter 2** methods and results for estimating the values of speeds and persistence times for cells performing chemokinesis, which is migration in uniform chemoattractant concentrations. These values are used in simulations of the simple OU process without chemotactic bias. The results suggest that speeds and persistence times may be functionally dependent on the chemoattractant concentration in ways that can have a significant impact on chemotaxis. In **Chapter 3** we include chemotactic bias and present several methods for estimating the chemotactic responsiveness. We also explore how different models of the chemoattractant concentration gradient and receptor-ligand binding can affect the results. The main result here is that our simple descriptions of chemotactic bias based on receptor-ligand binding cannot completely explain the experimental data. We present several recommendations for dealing with the discrepancies. **Chapter 4** presents the vector sum model of signal integration, and

experimental methods and results for cells migrating in two chemoattractant gradients. We examine here the effects that different spatial arrangements of the gradients and different values for the receptor-ligand binding parameters have on vector sum migration or signal prioritization. We also show how the micropipette assay is better suited than previous assays for studying chemotaxis to multiple gradients because it allows for dynamic modifications of the gradients. Finally, in **Chapter 5**, we present our main conclusions and make specific recommendations for developing the modeling framework.

Chapter 2

Neutrophil Migration in Uniform Chemoattractant Concentrations

2.1 Introduction

In this chapter, we begin development of our modeling framework by presenting a simple version of the OU process along with experimental and computational methods for exploring chemokinesis, or random migration, using this model. Chemokinesis is commonly described as a persistent random walk and is amenable to description using the OU process, as described in the previous chapter. The main purpose of this chapter is to demonstrate and apply methods to quantify the speeds and persistence times from experimental traces of cell migration paths so that we can substitute these values into the OU process and simulate these paths. We also wish to explore the functional dependence of the speed and persistence time on the chemoattractant concentration.

The OU process uses two terms to describe differential changes in cell velocity as follows

$$d\vec{v} = -\beta\vec{v}dt + \sqrt{\alpha}d\vec{W} \qquad (2.1.1)$$

where $\vec{v}$ (mm/min) is a two-dimensional velocity and $\vec{W}$ is a two-dimensional Weiner, or white-noise, process. The two parameters in this equation, α and β, are related to the

speed S (μm/min) and persistence time P (min) by the equations $S = \sqrt{\alpha/\beta}$ and $P = 1/\beta$ [Stokes et al., 1991]. The first term describes decay in the velocity, while the second term describes random accelerations. The two-dimensional position of the cell, $\vec{x}$, is found by integrating the velocity over time, to give

$$\vec{x} = \int_0^t \vec{v} dt \qquad (2.1.2)$$

The speed of a cell is most simply defined as the distance it migrates divided by the time it takes to migrate this distance. The difficulty in accurately measuring the speed of a neutrophil is in choosing an appropriate reference point on the cell. Neutrophils often migrate in somewhat jerky paths and can form pseudopods at various locations on their surface that make it difficult to obtain this reference point. Although still somewhat arbitrary, the centroid of the cell is commonly used and we will use it here [Dunn and Brown, 1987; Stokes et al., 1991].

Further difficulties arise when measuring the persistence time. The most general definition of the persistence time is the time that a cell crawls before making a significant change from its original direction. The degree of significance is arbitrary and an angle of 90° has been used previously [Foxman et al., 1999]. A more rigorous mathematical definition is that the persistence time is the inverse of the rate of change in the direction of migration [Dunn, 1983; Othmer et al., 1988]. Methods are available for estimating the persistence time based on this definition.

A more rigorous method for determining the speed and persistence time of a cell is to use fit equations describing either the mean squared displacement or, alternatively, the variance of the position via nonlinear regression. These equations have been derived directly from the OU process and are presented below [Doob, 1942; Gillespie, 1996].

There are two main types of chemokinesis based on the effects of the chemoattractant concentration on the speed and persistence time [Tranquillo and Alt, 1990]. These may play a significant role in how a cell behaves in a chemoattractant concentration gradient. The first type, termed orthokinesis, occurs when the speed of the cell varies with the chemoattractant concentration. If the speed is lower in higher concentrations, for instance, a cell will spend more time in the higher concentrations because it will, in essence, become trapped. The second type, termed klinokinesis, occurs when the persistence time varies with chemoattractant concentration. If the persistence time is lower in higher concentrations, for instance, a cell will also become trapped in high concentrations because it will tend to migrate around in circles more. The net effect of chemokinesis could be to drive cells to higher chemoattractant concentrations. This would be analogous to temporal gradient sensing in bacterial cells [Berg and Purcell, 1977]. Although the effect of chemokinesis is the same, this behavior is not accurately described as chemotaxis because it is independent of the concentration gradient. Bacterial cells adapt their rate of tumbling based on the difference in concentration between two points. No such mechanism for making these comparisons is known to exist in neutrophils.

2.2 Materials and Methods

2.2.1 Cells and chemoattractants

Human neutrophils were isolated from a drop of blood collected by a finger prick, as in [Zigmond and Sullivan, 1979]. After obtaining approval from the UC Berkeley Committee for the Protection of Human Subjects (CPHS #2004-11-34), volunteers were recruited. A drop of blood was obtained using a capillary blood sampling lancet (BD Biosciences, 23G needle) and allowed to clot on a 70% ethanol-cleaned coverslip (Fisher Scientific) in a humid chamber placed in a 37 °C, 5% CO_2 incubator. The humid chamber was made by placing a small Petri dish, holding the coverslip, in a larger one containing a layer of distilled water. An adhesive rubber gasket was stuck to the bottom of the small Petri dish to make it easier to remove the coverslip. After 45 minutes the coverslip was removed and placed in a live cell chamber, custom-made in the UC Berkeley machine shop. The clot was rinsed using modified Hanks Balanced Salt Solution (mHBSS) (150 mM NaCl, 4 mM KCl, 1.2 mM $MgCl_2$, 1.4 mM $CaCl_2$, 10 mg/mL glucose, 20 mM HEPES, and 10 mg/mL human serum albumin (Sigma-Aldrich)) until the solution was clear. A layer of HBSS was placed over the neutrophils that remained adhered to the coverslip. To study chemokinesis, cells were stimulated at room temperature with uniform concentrations of fMLP. A stock solution containing 10 mM fMLP (Sigma-Aldrich) in DMSO was diluted to the desired concentration. The final concentrations used were 10 pM, 1 nM, 100 nM, 10 μM, and 100 μM. Control experiments were also performed in which no chemoattractant was added.

2.2.2 Image acquisition and processing

Phase contrast images were taken with a QImaging Micropublisher 3.3 RTV camera on a Zeiss Axiovert 25 microscope using a 10x objective. The cells were first focused and the correct exposure determined using the QCapture software. The images were acquired every 10 seconds for 1 hour and saved in the tiff format using a program written in National Instruments LabVIEW 7.1. The raw images were acquired using the entire area of the CCD and were then sampled using code written in Matlab by taking the average over 4x4 groups of pixels, resulting in images that were 512 x 384 pixels (sample code can be found in appendix A.1). This produced images of a more manageable size and smoothed contrast artifacts resulting from the color CCD. A calibration slide containing 100 lines/mm was imaged under the same conditions to convert cell paths from pixels. The size of each pixel was determined to be 0.35 μm and this was multiplied by 4 for application to the binned image.

2.2.3 Cell tracking

Cells were tracked manually using code written in Matlab (sample code can be found in appendix A.1). In each image sequence, greater than 50% of the cells did not move more than one cell diameter. Ten cells were selected for tracking from each sequence primarily based on their migration distance. While this likely biases the estimates for speeds and persistence times, the same method was used for each sequence (concentration) so the effect of the concentration should still be observable. Our attempts to dilute the cells to prevent interactions were unsuccessful. As such, most, if not all of the cells tracked interact in some way with neighboring cells. The effect of these collisions is unclear. For every cell tracked, the images from the sequence were displayed

consecutively with a pause between each to allow for the user to estimate and click on the centroid position of the cell. The x and y positions of each click were recorded and stored.

After converting all the tracks to μm from pixels and adjusting them so they started from the origin, the x and y positions were smoothed in time to eliminate noisy artifacts introduced by manual tracking. To smooth the positions, a window in time around each position was fit to a second order polynomial using the Matlab command polyfit. The corresponding polynomial was then evaluated at each position (sample code can be found in appendix A.1). A window of 12 points on either side of the position being evaluated was determined to give the best smoothing without losing important features. For points close to the ends, the available data was used for the polynomial fit. Figure 2.1, below, shows 10 cell tracks and the x and y positions over time both before and after smoothing and converting from pixel units.

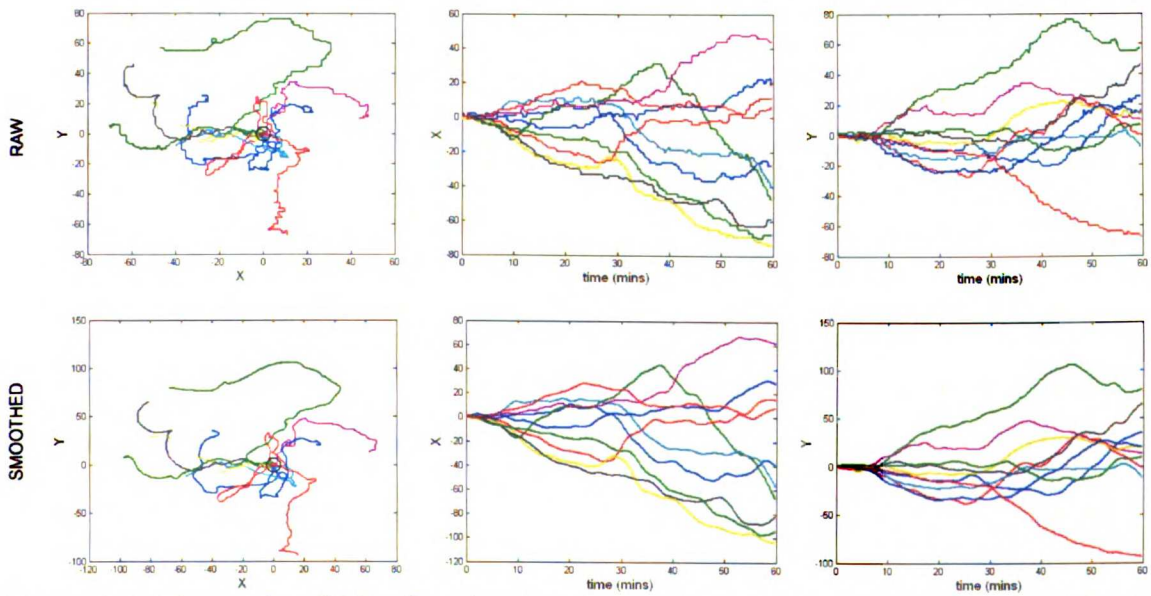

Figure 2.1: The tracks of 10 cells migrating in a uniform concentration of 1 nM of fMLP, adjusted to start at the origin. The top row shows the raw cell tracks and the bottom row shows the tracks after smoothing and converting from pixel units.

2.2.4 Estimating speed and persistence time

The speeds S (μm/min) and persistence times P (min) were estimated from the smoothed cell tracks using three different methods and compared. To further test the methods, the speeds and persistence times were estimated from simulated cell tracks using the same methods and compared to the known values used in the simulations.

The first method, outlined in [Stokes et al., 1991], fits an equation first derived by [Doob, 1942] to data from individual cell tracks. This equation describes the mean square displacement $\langle D^2 \rangle$ for the one-dimensional O-U process:

$$\langle D^2 \rangle = S^2 P^2 \left(\frac{T}{P} - 1 + e^{-T/P} \right) \qquad (2.2.1)$$

For two dimensions, Eq. (2.2.1) is multiplied by 2. The independent parameter T is the interval time. For a cell track containing 360 points taken at 10 seconds intervals, the mean square displacement corresponding to an interval of 10 seconds is taken from the 359 available displacements. For an interval of 20 seconds, there are 358 available displacements to determine the mean and so on until, for the longest interval time of 360 x 10 seconds there is only one displacement to determine the mean. As such, the experimental and predicted mean square displacements deviate from each other at longer interval times. To avoid this deviation, the equation is fit for interval times corresponding to half the total time of the image sequence. We will also pool the data from all cell tracks here to improve the statistics.

The second method fits a similar equation that describes the variance in the displacement in one dimension [Lemons, 2002] to the combined cell tracks over the elapsed time t, rather than the interval time:

$$\mathrm{var}\{x(t)\} = S^2P^2\left[\frac{t}{P} - 2\left(1-e^{-t/P}\right) + \frac{1}{2}\left(1-e^{-2t/P}\right)\right] \qquad (2.2.2)$$

This equation and Eq. (2.2.1) can actually be fit separately to the x and y data and the resulting speeds and persistence times can be compared. This is because the x and y displacements are assumed to occur independently and can thus be described by two independent OU processes. Notice that for $t << P$ and $T << P$ in Eq. (2.2.1) these equations are equivalent and show that the mean square displacement and variance are both linearly proportional to the elapsed or interval time, respectively. For larger times, the two equations deviate from each other by a constant value of one half. This deviation is discussed in more detail below. Both equations above were fit to the data using Matlab's nlinfit command, which uses the Gauss-Newton method (sample code can be found in appendix A.2). To use this command, initial estimates of the parameters to be fit are necessary. The initial estimates used here correspond to literature estimates suggesting a speed of 10 μm/min and a persistence time of 3 minutes. The standard deviations on the best fit lines were determined using Matlab's nlparci command.

The third and final method for determining the speeds and persistence times is to calculate them directly from the data using equations similar to those discussed in [Dunn, 1983]. The equation for the speed of the cell is given by

$$S = \lim_{\tau \to 0} \frac{\langle \delta^2 \rangle^{1/2}}{\tau} \qquad (2.2.3)$$

where δ is the distance displaced over the time interval τ. Clearly the frame rate will constrain our ability to take this limit. The important point is that the cell displacement over smaller intervals will be negligible. With a speed on the order of 10 μm/min and a cell diameter of approximately 10 μm, we can expect that there will be a displacement of about 1 cell diameter per minute. At an interval of 10 seconds per frame, we are justified in using this equation since a displacement of $1/6^{th}$ of a cell diameter is negligible. Estimating the centroid by eye can incorporate error up to as much as one half a cell diameter. This also justifies smoothing the data as described above. The equation for the persistence time in direction is calculated in a similar manner using

$$P = \lim_{\tau \to 0} \frac{2\tau}{\langle \phi^2 \rangle} \qquad (2.2.4)$$

where ϕ is the angle between subsequent displacements. We are again constrained by the frame rate in determining the persistence using this equation. As above, we expect small displacements at small times that will exclude turns of a significant angle. The persistence time is especially sensitive to the manual tracking method and is further justification for smoothing the data. The Matlab script used to calculate these values can be found in appendix A.2 included in the script used for the nonlinear parameter estimation.

The random motility coefficient μ ($\mu m^2/min$) found in population chemotaxis equations described in Chapter 1 is related to the speed and persistence time by

$$\mu = \frac{1}{2} S^2 P \qquad (2.2.5)$$

The random motility coefficient was determined from estimates of the speed and persistence time. The mean free path of a cell is the product of the speed and persistence time. This value was also calculated from the estimates.

2.2.5 Model simulation

Simulations were performed using approximate updating formulas for the velocity and position of an OU process [Gillespie, 1996]. The updating formula for the velocity in the x direction is given by

$$V_{x,i+1} = V_{x,i}\left(1 - \frac{\Delta t}{P}\right) + S\sqrt{\frac{\Delta t}{P}} N(0,1) \qquad (2.2.6)$$

where i indicates the step, Δt is the time step size, and $N(0,1)$ is a normally distributed random number with a mean of 0 and a variance of 1. Since the velocities can be described by separate OU processes, a similar updating formula was used for the velocity in the y direction with an independent normal random number for each step. The x position of the cell was then determined by numerical integration of Eq. (2.2.6) to give

$$X_{i+1} = X_i + V_i \Delta t \qquad (2.2.7)$$

A similar formula was used to calculate the y position. Although exact formulas are available, the error between the approximate and exact formulas is negligible for small values of the time step size. We set the step size to 0.01 seconds to minimize this error and sample the results at every 10 seconds to match the experimental sample rate. The reason for not using the exact formulas here is because the approximate formulas are more easily related to the speed and persistence time and will be used to describe chemotaxis in the next chapter by including a bias term on the velocity. The Matlab script used to simulate the OU process can be found in appendix A.4. The methods used to estimate the speeds and persistence times are similar to those described above.

2.2.6 Similarity measures

The cell paths resulting from the simulation were compared to the experimental paths by direct examination of the estimated speeds, persistence times, mean free paths and random motility coefficients. Further comparisons were made by calculating the correlation coefficients between the experimental and simulated data for the x and y positions separately at each time step (Matlab code can be found in appendix A.2). To test this method, we find the correlations with additional simulated paths using values for the speed and persistence time equal to half those used in the first simulation. We compare the results between the two simulations and also compare figures showing the resulting migration paths to estimate the accuracy of the results.

2.3 Results and Discussion

Five different concentrations of the formylated peptide fMLP were used in the neutrophil chemokinesis experiments ranging from 10 pM to 100 μM, along with an experiment in which there was no chemoattractant. In the absence of chemoattractant, the neutrophils appeared to ruffle continuously, but did not crawl. In the lowest and highest concentrations, the cells also ruffled and crawled, but never more than one cell diameter. Due to the difficulty in getting accurate statistics, cells in these concentrations were not tracked. The smoothed tracks for 10 cells in each of the three remaining concentrations (1 nM, 100 nM, and 10 μM) are displayed in Figure 2.2, below. All cell paths are adjusted to start from the origin which is indicated by a small black circle in each plot. Notice that the scales on the x and y axes are the same for the three different concentrations. In analyzing this figure, there does not appear to be a clear trend in the migration paths of the cells based on the chemoattractant concentration. If the speed or persistence time were dramatically different at different concentrations, for instance, we would expect to see more significant differences in the overall cell paths. The mean free paths of the cells may be similar, however, while the speed and persistence time vary. Further analysis is needed to make this distinction.

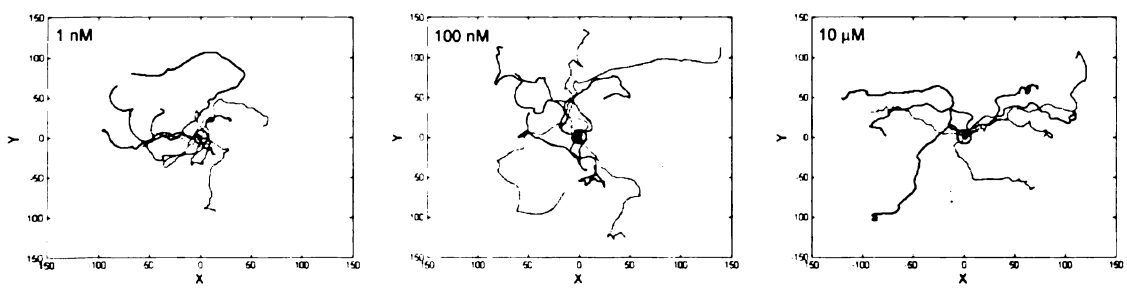

Figure 2.2: The smoothed tracks of 10 cells in each of three different concentrations of fMLP. The tracks are adjusted to start at the origin which is indicated by a small black circle.

Figure 2.3, on the following page, shows the data obtained from the cell paths used to estimate the speeds and persistence times. Each column corresponds to one of the three different concentrations and resulting paths shown in Figure 2.2. The top row shows the mean squared displacement found by pooling data from all cells plotted against the interval time. The dashed lines are the mean-squared displacements predicted by Eq. (2.2.1) after fitting the equation to the experimental data to obtain estimates for the speeds and persistence times. The second and third rows show the variances in the x and y positions of all cells in each concentration plotted against the elapsed time. The dashed lines are the variances predicted by Eq. (2.2.2) (and a similar version for the variances in y) after fitting to the data.

Table 2.1, on the following page, shows the speeds and persistence times and their standard deviations found by nonlinear parameter estimation as discussed in the Materials and Methods section. Notice that the fits are much better and the standard deviations are smaller for the method that uses the mean-squared displacement. This is because the mean-squared displacement is found by averaging the displacements over 10 cells and many time intervals. The mean-squared displacement calculated for an interval time of 30 minutes, for example, is found from 10 cells and 59 available 30 minute intervals.

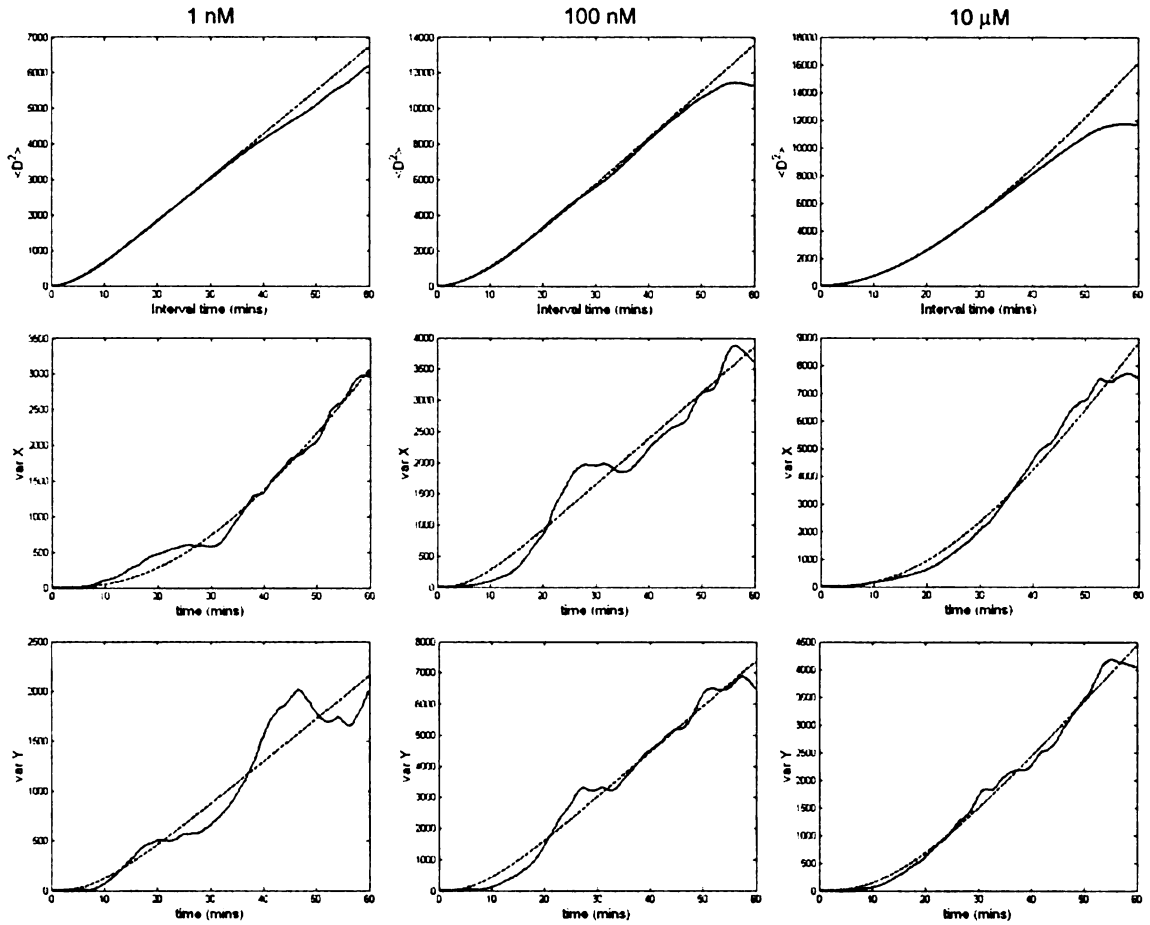

Figure 2.3: The data obtained from the cell paths used to estimate the speeds and persistence times. Each column corresponds to a different uniform concentration of fMLP as indicated at the top of the columns. The first row is the mean-squared displacement over the interval times. The second and third rows show the variance of the x and y positions over the elapsed time, respectively. The dashed lines indicate the best fit to the data.

Table 2.1: The speeds and variances of migrating cells, and standard deviations estimated from the data. Method 1 uses the mean-squared displacement; method 2x and 2y use the variances in x and y, respectively; and method 3 uses the direct calculations.

	1 nM		**100 nM**		**10 μM**	
Method	S (μm/min)	P (min)	S	P	S	P
#1	3.44 +/-0.02	5.20 +/-0.08	3.97 +/-0.04	8.4 +/-0.3	2.84 +/-0.01	29.0 +/-0.4
#2 x	2.14 +/-0.01	24.6 +/-1.5	3.8 +/-0.2	5.0 +/-0.6	3.73 +/-0.03	19.3 +/-1.3
#2 y	2.56 +/-0.15	6.5 +/-1.1	4.8 +/-0.1	6.3 +/-0.5	3.01 +/-0.03	11.4 +/-0.5
#3	3.4 +/-0.3	0.3 +/-0.3	4.3 +/-2.1	0.3 +/-0.3	3.4 +/-1.7	0.25 +/-0.29

In contrast, the variance in the x position for an elapsed time of 30 minutes is only found from the positions of 10 cells at this time point. The standard deviations found using the Matlab nlparci command are quite low, most notably on the estimates found using the mean-squared displacement. A more thorough error analysis can be performed by fitting the equation to the lines corresponding to the mean-squared displacement at each interval plus or minus one standard deviation.

An examination of the speeds between the different concentrations does not indicate any trend that would be consistent with an orthokinesis. Note that the speeds determined from all three methods are fairly consistent. The persistence times, however, vary dramatically. The persistence times determined from the third method are quite low. This observation, along with the problems discussed earlier, suggests that this method may not be suitable for accurate estimation. The persistence time estimated from the 1 nM data using the variance of the x position is also considerably different than that predicted from the same data using the variance of the y position or the other methods. By examining the paths in Figure 2.2, we see that there does seem to be a bias toward the negative x direction that could be causing this. The reason for this bias is unclear. The conditions are assumed to be isotropic so that there should be negligible difference between the parameter estimates for the x and y directions. There also appears to be a higher persistence time for the highest concentration of 10 μM with a significant difference in the estimates using the various methods. Given that the speeds at this concentration are similar to the speeds at the other concentrations we would expect to see a larger mean free path for these cells in Figure 2.2 that would cause them to migrate

greater distances from their starting points. The discrepancy could be caused by the estimate of the standard deviation as discussed above.

Table 2.2 displays both the mean free path and the random motility coefficient calculated from the top three rows displayed in Table 1.1 for each of the three different concentrations (the fourth row was not included for reasons discussed above). The only discernible trend comes from looking at the data in the first row. Both the mean free path and the random motility coefficient increase with increasing concentrations. This is caused by a similar trend in the first row of Table 1.1 for the persistence times. This is actually unexpected. Previous results from rat alveolar macrophages show a peak in the random motility coefficient at intermediate concentrations that drops off on either side (Farrell et al., 1990). While it is possible that human neutrophils behave differently, it is difficult to come to any solid conclusions without performing more repetitions over a wider range of concentrations.

Table 2.2: The mean free paths of migrating cells determined from estimates of the speeds and persistence times in three different uniform concentrations of fMLP.

	1 nM		**100 nM**		**10 μM**	
Method	Mean free path (μm)	μ (μm^2/min)	Mean free path	μ	Mean free path	μ
#1	17.9	123.1	33.3	264.8	82.4	467.8
#2x	52.6	225.3	19.0	144.4	72.0	537.0
#2y	16.6	85.2	30.2	290.3	22.9	206.6

To further test the methods used above for estimating the speed and persistence time, we turn now to simulations of the OU process. For an initial run, we choose a speed of 4.2 μm/min and a persistence time of 6.5 minutes. These values roughly correspond to the estimates determined from the data for cells migrating in 100 nM fMLP. Figure 2.4, on the following page, shows the simulated migration paths of 10 cells and the x and y positions of the cells over time. Notice that the scales on the x and y axes of the plot showing the paths are the same as those in Figure 2.2, above. The appearance of the simulated paths is similar to those of the experimental paths with the notable exception that at least one simulated cell crawls out of the frame and another crawls very close to the edge.

Figure 2.5, below, shows the data obtained from the cell paths used to estimate the speeds and persistence times along with the best fit lines. The first frame uses the equation for the mean-squared displacement and the second and third frames use the equation describing the x and y variance, respectively.

Table 2.3 shows the estimated speeds and persistence times and their standard deviations that correspond to the best fit lines in Figure 2.4. The mean free paths and random motility coefficients are also displayed. The estimates are all fairly close to the true value used in the simulations, especially for the estimates obtained using the y variance. The estimates found using the equation for the mean-squared displacement are slightly higher. As above, the standard deviations using this method are fairly small and can probably be more rigorously determined. The mean free path and random motility coefficient are also similar to those displayed in Table 2.2, above, for the cells migrating in 100 nM fMLP.

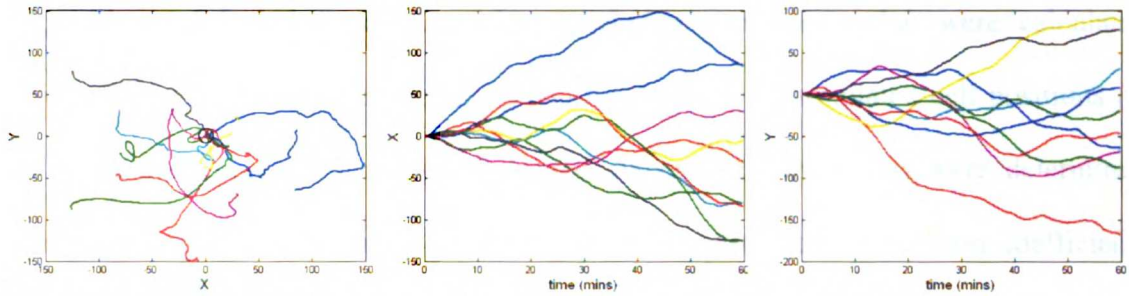

Figure 2.4: Simulated migration paths of 10 cells starting from the black circle, and the x and y positions of these cells over time.

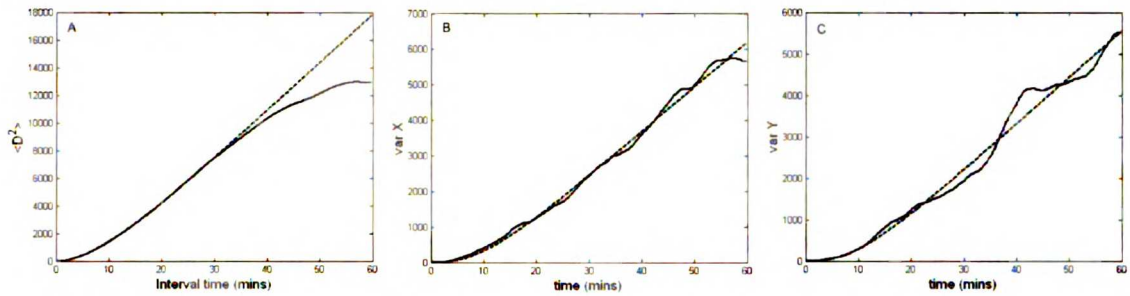

Figure 2.5: The data obtained from the simulated cell paths used to estimate the speeds and persistence times. A) The mean-squared displacement over the interval times. B) The variance of the x and C) y positions over the elapsed time, respectively. The dashed lines indicate the best fit to the data.

Table 2.3: The speeds and variances of migrating cells and their standard deviations estimated from the simulated data, along with the mean free paths and the random motility coefficients calculated from these estimations. Method 1 uses the mean-squared displacement and methods 2x and 2y use the variances in x and y, respectively. Compare to literature estimates suggesting a speed of 10 μm/min and a persistence time of 3 minutes.

Method	S (μm/min)	P (min)	Mean free path (μm)	μ (μm^2/min)
#1	4.49 +/-0.01	8.63 +/-0.04	38.75	348.0
#2x	4.20 +/-0.05	7.1 +/-0.3	29.8	250.5
#2y	4.0 +/-0.1	7.0 +/-0.5	28.0	224.0

Figure 2.6, below, displays the correlation coefficients that were calculated between the experimental cell positions and the two sets of simulated cell positions (A and B) at each point in time. As discussed above, the correlations were determined separately between the x and y positions. For comparison, the correlation coefficients were calculated between the two sets of simulated cell positions (C). Each set of simulations was run using the same seed in the random number generator which likely contributed to the high correlation. Notice the y-axes in these plots are scaled between 0.75 and 1 to enhance the details. The conclusion from this figure is that we cannot use the correlation coefficient to make a determination as to the degree of similarity between the experimental and simulated cell paths. A better test is to visually compare the cell migration paths directly using Figure 2.7, on the following page. Note that the x and y axes are similar in each plot for the three sets of migration paths. Clearly the first two sets are more closely related to each other than either one is to simulation set #2. Parameter estimates obtained as above for simulation set #2 gave results that were fairly close to the actual values used in this case.

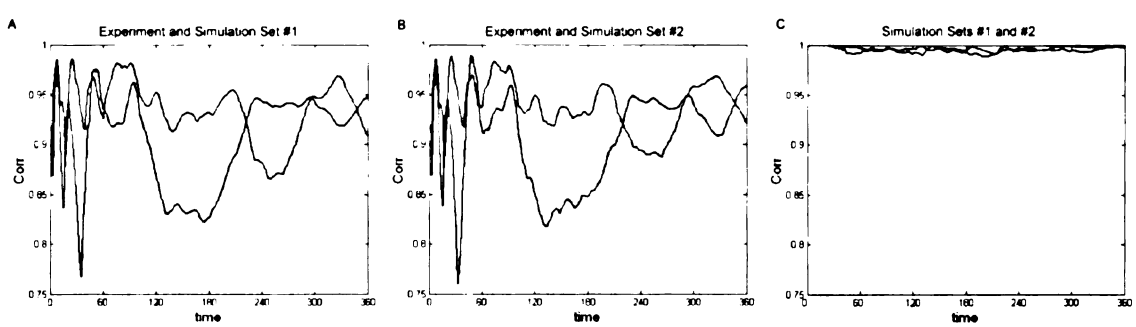

Figure 2.6: A) The correlation coefficients between experimental and simulated cell positions at each point in time. The blue line corresponds to the x positions and the green line corresponds to the y positions. B) The correlation coefficients between experimental and simulated cell positions for simulations using half the speed and persistence time. C) The correlation coefficients between the two sets of simulated cell positions.

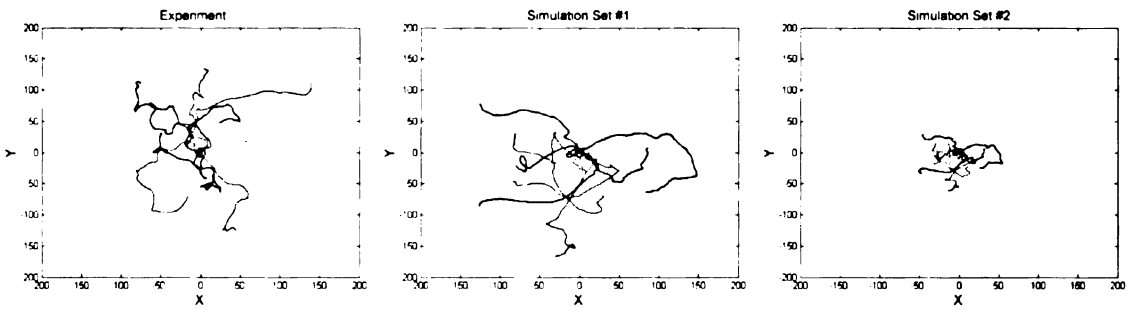

Figure 2.7: Cell migration paths from an experiment using 100 nM fMLP, and from simulations using a time step of 0.01 sec. in which the speed and persistence time were estimated from the experimental data (set #1) or were set equal to half the estimated speed and persistence time (set #2).

2.4 Conclusions

In this chapter we presented methods for estimating the speed and persistence time in uniform chemoattractant concentrations. We also demonstrated the substitution of these estimates into the OU process to simulate cell migrations paths. We do not have clear evidence to suggest the dependencies of the parameters on the chemoattractant concentration. As a result, we make no conclusions regarding the types of kineses that neutrophils exhibit. Evidence suggests that persistence time is a more sensitive parameter. We have developed a framework to further explore these issues. In particular, more experimental data is needed to increase the number of samples and our confidence in parameter estimates and to develop the functional dependencies. Once these functions are determined they can easily be included in the simulations. We also have not explored how these parameters may depend on the type of chemoattractant. This raises several interesting questions: How will the dependence on chemoattractant type be included in the model? What happens when cells are simultaneously exposed to two chemoattractants in uniform distributions? We will put these questions aside for future work and turn now to developing the model to account for single chemoattractant gradients.

Chapter 3

Chemotaxis in the Micropipette Assay

3.1 Introduction

The purpose of this chapter is to develop the OU process to study neutrophil migration in chemoattractant gradients. As discussed in Chapter 1, we use a modified form of the OU process originally proposed by [Stokes et al., 1991] that includes a term to describe the chemotactic bias. These researchers assumed that this bias was caused by a gradient of bound receptors across a cell and further assumed that the bound receptor gradient was linearly proportional to the chemoattractant gradient. We relax this last assumption to attempt to account for important physical aspects of receptor-ligand binding such as the receptor quantities and binding affinities that affect saturation and likely play roles in determining the range of concentrations and gradients in which neutrophils display sensitivity, as discussed in [Zigmond, 1977].

The modified OU process that we use to account for neutrophil chemotaxis is given by

$$d\vec{v} = -\frac{\vec{v}dt}{P} + \frac{S}{\sqrt{P}} d\vec{W} + \kappa d_{cell} \nabla C \qquad (3.1.1)$$

where we have substituted α and β from Eq. (2.1.1) with the speed and persistence time defined earlier. The bias term on the end is one possible model that accounts for the

difference in the number of bound receptors across a cell. This difference is the product of the diameter of the cell, d_{cell} (μm), and the gradient in bound receptors, ∇C (#/cell/μm). We develop and examine several possible models based on receptor-ligand binding for the chemotactic bias, obtaining estimates for the binding parameters from the literature [Zigmond, 1977; Lauffenburger and Linderman, 1993; Adams et al., 1998]. The proportionality constant κ (μm/min/#/cell) is defined as the chemotactic responsiveness and is used as a fitting parameter. Ideally this parameter would be constant and any observed differences in migration paths would be strictly attributable to the effects of the chemoattractant concentration on the speed and persistence time or the resulting gradient of bound receptors.

We use the micropipette assay to study the response of neutrophils to chemoattractant gradients. This assay has typically been used to study specific components of the chemotaxis network [Weiner et al., 1999; Iijima and Devreotes, 2002], and this represents the first attempt that we know of to apply it to a higher level model. The under-agarose assay is more common in these types of studies [Farrell et al., 1990; Foxman et al., 1999]. The micropipette assay offers several advantages over the under-agarose assay: it enables real-time monitoring of the chemoattractant gradient via a fluorescence tracer; it provides more reproducible gradients; it is relatively easy to set up and use; and it enables an exploration of the temporal response of neutrophils to changing gradients. We wish to use the experimental results to make estimates of the chemotactic responsiveness and to develop the structure of the model for chemotactic bias so that we can, with the speed and persistence time from the previous chapter, predict cell migration paths in chemoattractant gradients. Although we were unable to estimate the chemotactic

responsiveness for reasons that are discussed below, we present several methods that can be used in future studies. We also present novel methods for quantifying the experimental data.

3.2 Materials and Methods

3.2.1 Cells and chemoattractants

The cells were isolated from a drop of blood collected by a finger prick, as described in [Zigmond and Sullivan, 1979] and in section 2.2.1, above. All of the procedures were the same as described in section 2.2.1 with the exception of the preparation of the chemoattractant. Stock solutions of 10 mM fMLP (Sigma-Aldrich) or 100 mM of the carboxy-terminal agonist analogue of C5a, N-Met-Phe-Lys-Pro-D-Cha-Cha-D-Arg (ChaCha; ElimBio) in DMSO were diluted to the desired concentration and loaded into a micropipette as described below. In each micropipette, 100 μM of the fluorophore carboxyfluorescein (FITC), diluted from a 10 mM stock solution in ethanol, was included to monitor the concentration profile.

3.2.2 Chemoattractant gradients

There are a number of assays available for studying neutrophil chemotaxis [Boyden, 1962; Nelson et al., 1975; Zigmond, 1977; Li Jeon et al., 2002]. In choosing the assay, we were constrained by our ability to reproducibly quantify the resulting chemoattractant gradients. In this section we describe our attempts to use several assays that showed promise in satisfying this constraint. In the end, we chose to use the micropipette assay for reasons that will become clear in the later discussion.

Microfluidics devices

We initially attempted to study chemotaxis of neutrophil-differentiated HL-60 cells using microfluidics devices. Introduced in [Li Jeon et al., 2002] for studying chemotaxis, microfluidics devices enable reproducible formation of temporally and spatially stable gradients in a variety of configurations. This is a critical improvement over previous assays that have proved difficult to control. These devices contain mixing channels and a main channel, or cell chamber, molded into polydimethylsiloxane (PDMS) bonded to a glass coverslip. The devices are produced using soft lithography as outlined in Figure 3.1, below.

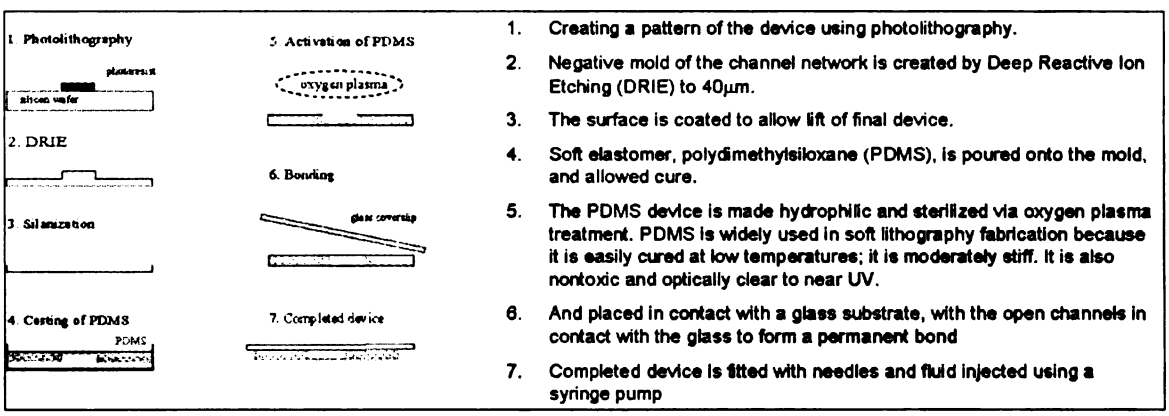

Figure 3.1: Outline of the steps involved in making microfluidics devices using soft lithography. (With Shilpa M. Shroff).

Figure 3.2A, on the following page, shows the entry ports and an upstream portion of the mixing channels in a microfluidics device before insertion of needles that allow for introduction of chemoattractant solutions. Figure 3.2B shows a microfluidics device in operation. Three needles are inserted through the PDMS into the entry ports and are attached by tubing to syringes containing different concentrations of chemoattractant. The flow into the device is driven by a syringe pump. A single needle is also connected to the exit port to allow for drainage. The concentrations used in the syringes determine the

profile of the concentration gradient ultimately created in the cell chamber. Figure 3.2C shows a schematic of the channels in the microfluidics device. The three entry ports at the top allow for injection of the solutions containing different chemoattractant concentrations. These solutions flow through the mixing channels to produce multiple streams containing intermediate concentrations that merge in the cell chamber. The resulting concentration profile is perpendicular to the fluid flow. The floor of the channels is created by the glass coverslip bonded to the PDMS. Cells are made to adhere to the coverslip in the cell chamber which is coated with an extracellular matrix (ECM) protein. A laminar flow rate insures that further mixing between merged streams occurs via diffusion, thus smoothing the profile downstream. Laminar flow also prevents the shear stress on the cells from becoming too high.

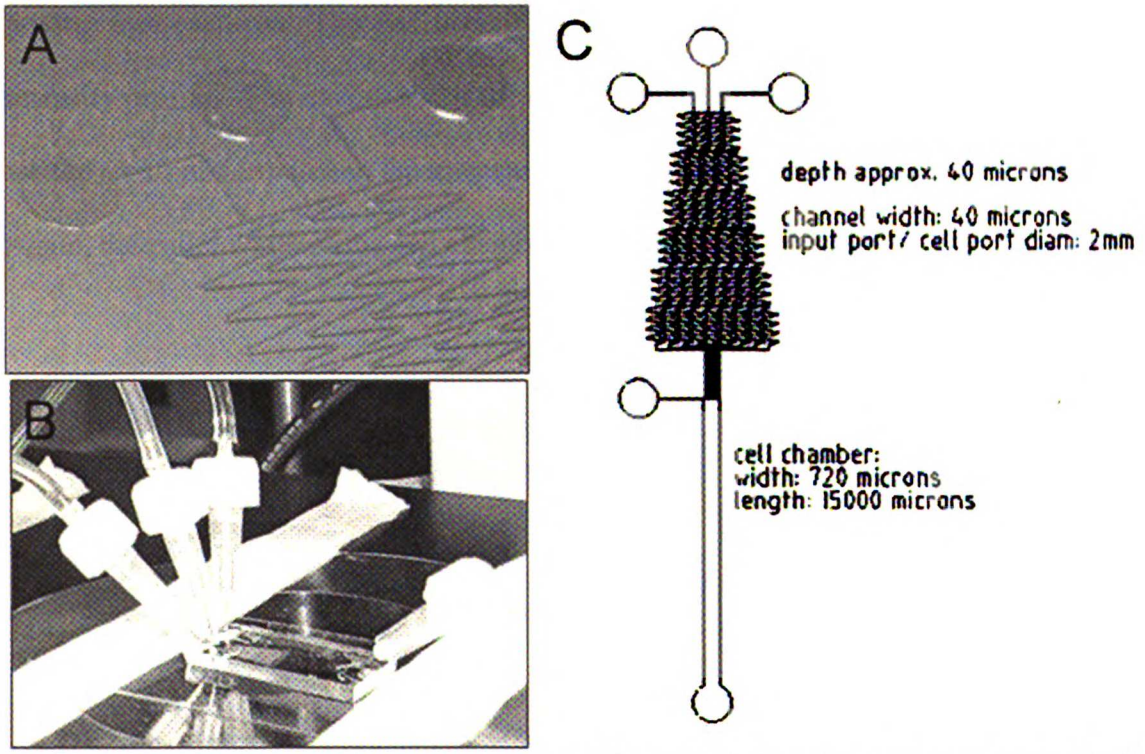

Figure 3.2: A) Entry ports and upstream portion of mixing channels in a microfluidics device before connecting external tubing. B) A microfluidics device in operation. C) A schematic of the channels contained in a microfluidics device. (With Shilpa M. Shroff).

To characterize the devices, we injected three different concentrations of the FITC and imaged the intensity profiles that developed in the cell chamber. The concentrations we used were 10 μM, 5 μM and 0 μM which would theoretically produce a linear profile. The results are displayed in Figure 3.3, on the following page. Figure 3.3A and B show the intensity image and profiles along a portion of the width of the entrance of the mixing channels into the cell chamber. Notice that only a portion of the entire width of the cell chamber is imaged due to limitations on the field of view. The blue lines are the profiles at various positions within the intensity image 0 – 400 μm downstream of the entrance. The discrete steps shown in these profiles are caused by the merging of the streams containing different concentrations of FITC. Figure 3.3C and D show the intensity and profiles 1400 – 1800 μm downstream. The profile is much smoother here since diffusive mixing has occurred. The red dots in B and D indicate the theoretically predicted intensity profiles. The deviations of the experimental profiles from the predicted profiles are the result of normalizing the intensities based on the maximum intensity in the image. Again, the entire width of the cell chamber is not imaged.

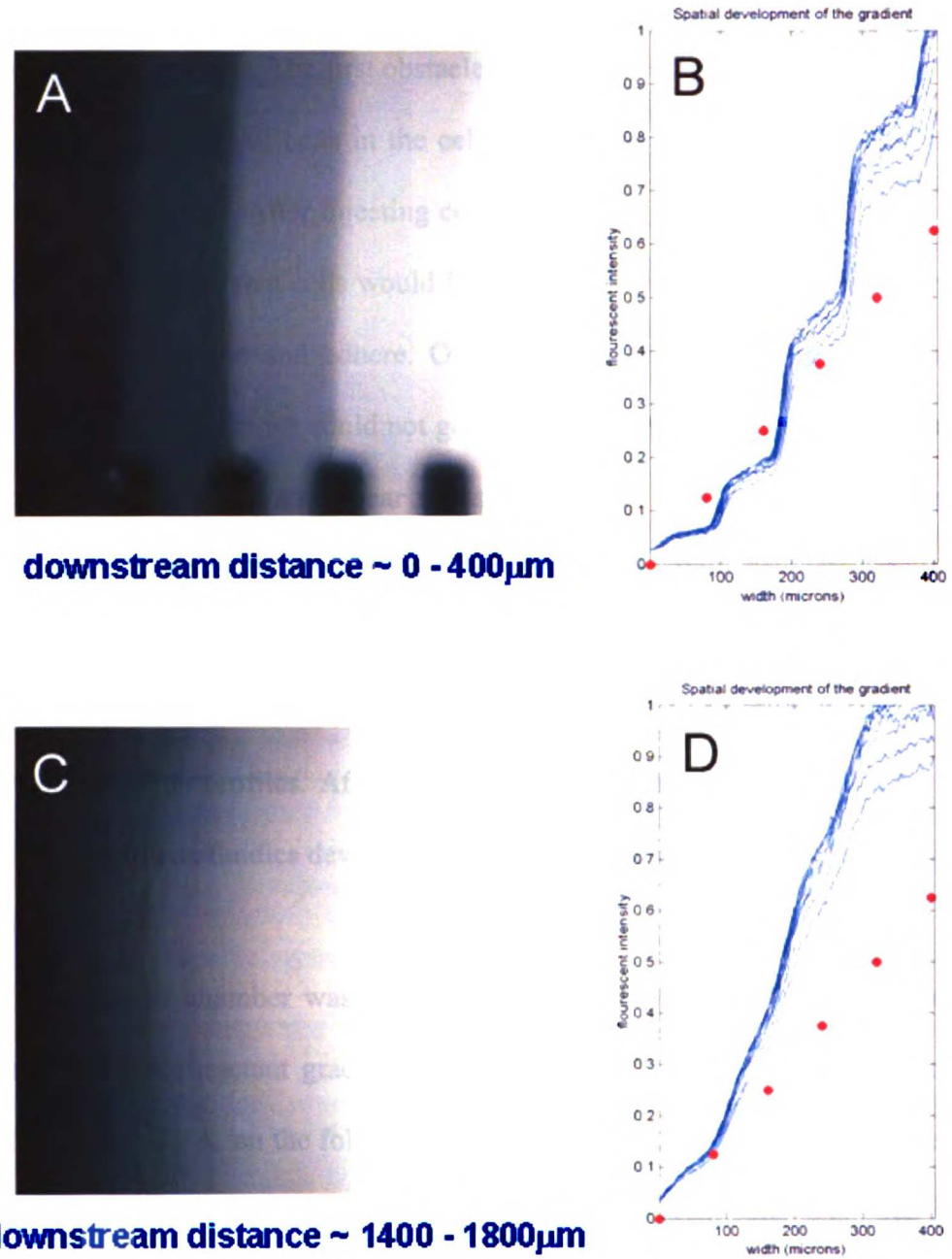

Figure 3.3: Fluorescent intensity profiles produced in the cell chamber of a microfluidics device. The three concentrations of FITC injected in the device were 10 µM, 5 µM, and 0 µM. A) The upstream portion where the mixing channels connect to the cell chamber. B) The corresponding normalized intensity profile at various positions (solid blue lines), and the predicted profile (red dots). C) A portion of the cell chamber 1400-1800 µm downstream of the entrance of the mixing channels. D) The corresponding normalized intensity profile at various positions (solid blue lines), and the predicted profile (red dots). (With Shilpa M. Shroff).

Several difficulties were encountered during our attempts to use the microfluidics devices to study chemotaxis. The first obstacle involved seeding cells into the devices. To obtain a good distribution of cells in the cell chamber we had to equalize the pressure between the various ports. After injecting cells into one of the ports, the pressure had to be controlled precisely so that cells would first flow into the cell chamber and then stop, giving them time to settle and adhere. Once we overcame this obstacle (with much practice) we discovered that we could not get enough cells to remain adhered to the floor of the chamber. Despite the low shear stresses, once the flow of chemoattractant was started cells would gradually detach from the surface and flow downstream. We also noticed that in the process of preparing the devices several of the mixing channels would become clogged with bits of PDMS or cellular debris. This had a dramatic effect on the resulting concentration profiles. After many attempts and much deliberation, we finally decided to put the microfluidics devices aside and attempt another assay.

Zigmond chamber

The Zigmond chamber was the first assay to allow direct visualization of cells responding to chemoattractant gradients [Zigmond, 1977]. A picture of the chamber is displayed in Figure 3.4A, on the following page, and a side and top view of the device in operation is displayed in Figure 3.4B. A coverslip with adherent cells is clipped into the device so that the cells rest over the bridge which resides between the two channels. A chemoattractant solution is placed in one groove and a media is placed in the other groove. The resulting difference in concentration drives diffusion and sets up a concentration gradient over the bridge. The profile evolves in time as the concentration equilibrates between the two grooves, as described in [Lauffenburger et al., 1988].

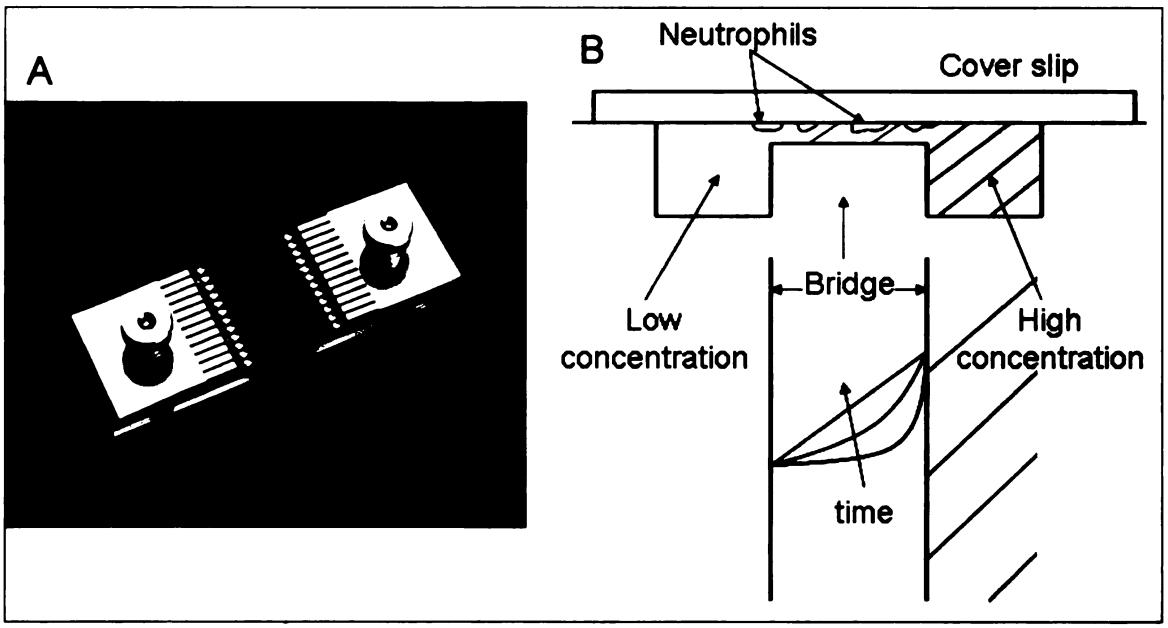

Figure 3.4: A) A picture of the Zigmond chamber (from http://www.neuroprobe.com). B) A schematic of the Zigmond chamber in operation, showing both side and top views.

Figure 3.5, on the following page, shows fluorescence intensity images and profiles taken at different times from an experiment to measure the gradient across the bridge. We used 0.2 μm diameter PC-Red beads as the fluorophore in this experiment. The higher concentration of beads was placed in the groove on the right in these images. Notice the peak in intensity that occurs along the left side in the images. This peak is caused by the integration of fluorescence throughout the depth of the channel. Over time this peak decreases and spreads out as the fluorophore diffuses throughout the channel. We also noticed a significant amount of convection, evidenced here by the visible blurring in the image taken at 0 minutes. Analysis of the corresponding movie shows that this convection periodically reverses due to unknown reasons. The concentration profiles, shown in Figure 3.5B, indicate that this convection may have a significant effect on the resulting gradient. After many failed attempts to correct this behavior, we decided to discard the Zigmond chamber and attempted to use the micropipette assay.

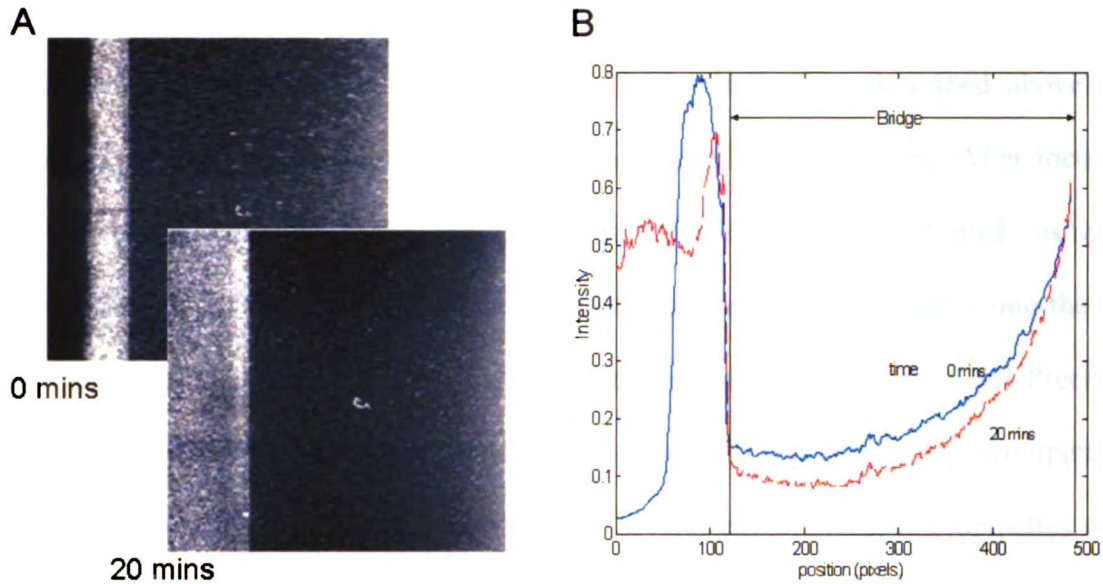

Figure 3.5: A) Intensity images taken at different times of 0.2 μm diameter PC-Red beads diffusing across the bridge in the Zigmond chamber. B) The corresponding intensity profiles along the width of the images, superimposed over a drawing of the bridge. The higher concentration was placed in the groove on the right side of these images.

Micropipette assay

Micropipettes were pulled from a borosilicate capillary with an outer diameter of 1.0 mm and an inner diameter of 0.5 mm containing a microfilament using a model P-97 Flaming/Brown Micropipette Puller (Sutter Instruments, Novato, CA). The two main conflicting constraints for choosing settings on the puller were that the tip had to have a small enough opening to enable precise control over the flow rate, but not so small that the micropipette would be susceptible to clogging. The settings that gave good results were as follows: step 1: heat = 660, pull = 50, velocity = 10, time = 250; step 2: heat = 600, pull = 70, velocity = 50, time = 250. The micropipettes were held in a vertical position and loaded by placing a 2 μL drop of a chemoattractant/FITC solution on one end. After several minutes, the drop moved to the tip by capillary forces. This method of loading excluded air bubbles. To insure that there was no particulate matter that would

clog the tip, the chemoattractant/FITC solutions were centrifuged for approximately 10 minutes before loading. Adherent neutrophils were obtained as described above and placed in the custom live-cell chamber discussed in section 2.2.1, above. After focusing on the plane containing the cells, the micropipette was positioned using a micromanipulator (Narishige). The flow rate of the chemoattractant solution into the live cell chamber was controlled through a pressure line connected to a 0-15 psi Precision Pressure regulator (McMaster). A picture of the live cell chamber and micropipette in operation is displayed in Figure 3.6, below. In several experiments, micropipettes were changed mid-experiment either to test a different concentration or to replace a clogged micropipette.

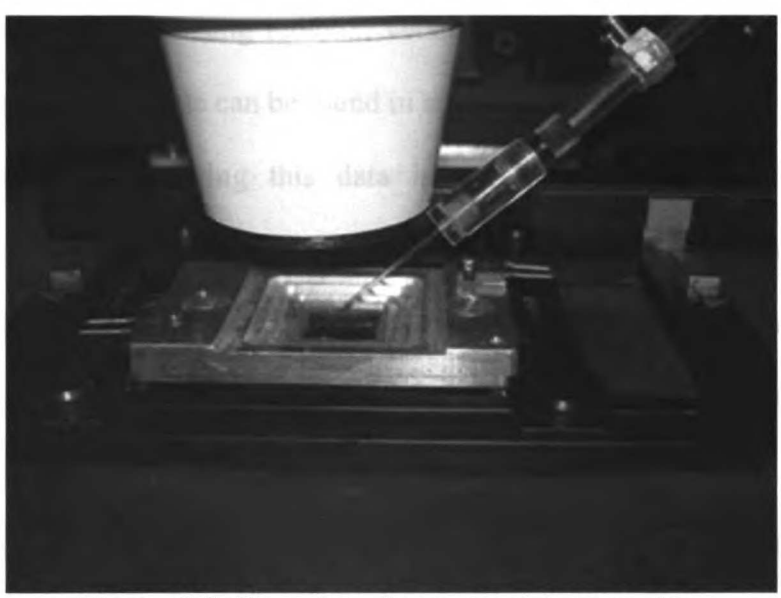

Figure 3.6: The micropipette assay in operation.

3.2.3 Image acquisition

All images were taken with a CoolsnapHQ camera (Photometrics) on a Zeiss Axiovert 200 using a Zeiss Plan-Neofluar 10x/0.3 NA objective at bin 3. The condenser had a 26 mm working distance and a 0.55 NA. The fluorescent images were taken using FITC cube filters (Ex D470/40 Em D535/40). Phase contrast and fluorescent images were taken every 15 seconds over a range of times that depended on the response. Images were captured using Metamorph (Molecular Devices Corporation, Sunnyvale, CA).

3.2.4 Image processing

In migrating to the micropipette tip, neutrophils interact and overlap much more than in the chemokinesis assay discussed in Chapter 2. As such, it was difficult to manually track individual neutrophils, thus necessitating the use of other methods for quantifying the data. In this section, we discuss several novel methods we developed for tracking an approximation of the cell density. All the image processing was performed using Matlab's Image Processing toolbox, version 3.1 (The Mathworks, Natick, MA). Samples of all processing code can be found in appendix A.1.

The goal in quantifying this data is to correlate cell migration with the chemoattractant concentration and concentration gradient. One of the issues we faced in developing suitable methods was that there was significant convection in the micropipette assay. This resulted in intensity profiles that, rather than being uniformly distributed in two dimensions around the micropipette tip, often contained long tails in random and occasionally fluctuating directions. While convection in the Zigmond chamber caused us to discard that assay, we were able to develop methods for dealing with convection in the micropipette assay.

For the first method, we account for non-uniformities in the concentration profile by averaging the intensities over time to produce a single intensity image. This method effectively accounts for persistent non-uniformities and averages out rapid fluctuations that we assume have little effect over the time scales of cell migration. From this averaged intensity image, we produced a contour plot showing regions of similar intensities. We used this contour plot to produce a series of masks; each mask corresponds to one of the contours. For instance, for the mask corresponding to a certain intermediate intensity value which we will call I_3, each pixel in the mask is set equal to 1 if that pixel's intensity in the averaged intensity image falls within a certain range of I_3. Otherwise the pixel value in the mask is set equal to 0. Figure 3.7, on the following page, shows a contour plot superimposed on an averaged intensity image, along with three of the masks produced using this method. The number of masks is an adjustable parameter in the processing code and is set to 20 here. The masks define the regions in which we tracked the density of cells over time, as discussed below. Notice that a portion of several masks will be attributable to the micropipette; we neglect these effects here.

Figure 3.8, on the following page, shows an example that outlines the steps taken in processing the phase contrast images. We began with a raw 16-bit image of the cells (A; this image is frame 236 out of 266 in the time-lapse sequence). We first needed to correct for variations in the intensity within the frame. We began by converting the 16-bit image to a double, producing pixel values that fell between 0 (black) and 1 (white). Using the *imadjust* command, we normalized the contrast by stretching the existing grayscale values over the entire range of allowable grayscale values. We then performed a

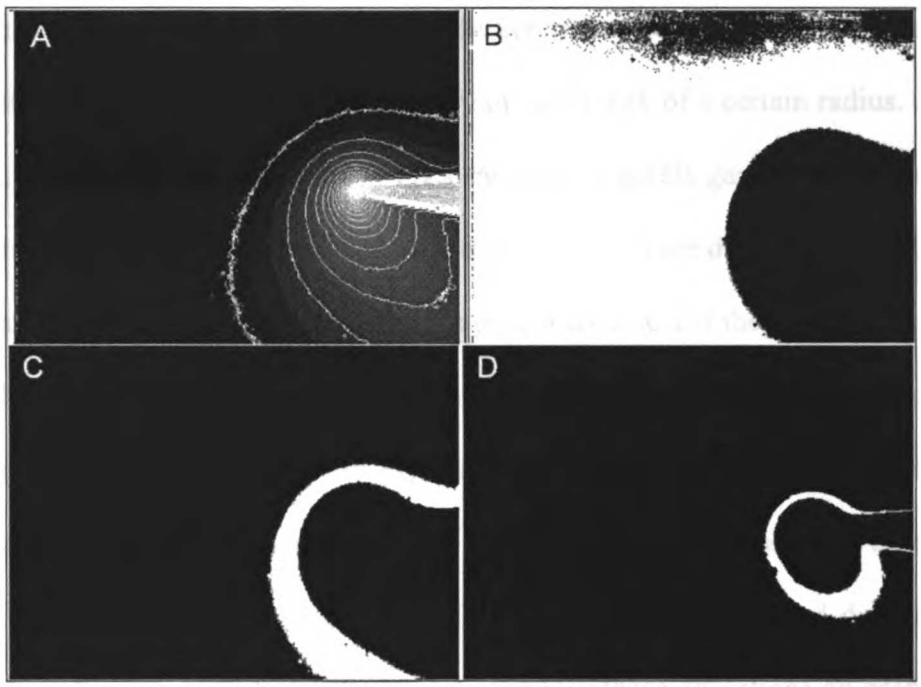

Figure 3.7: A) A contour plot superimposed on an intensity image averaged over 266 frames. B, C, D) Masks created from three of the contours in A.

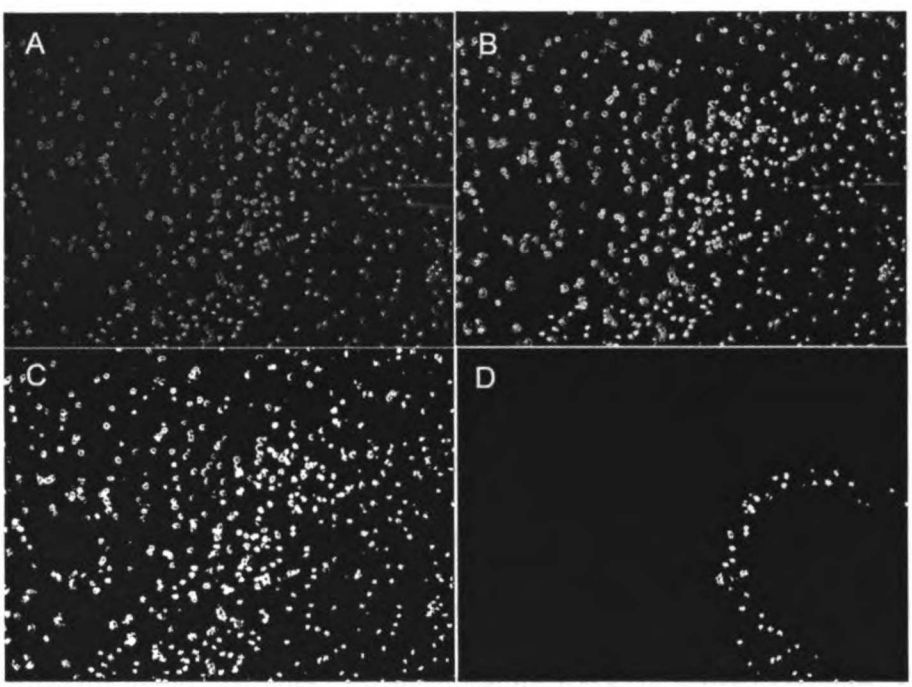

Figure 3.8: The steps taken in processing phase contrast images. A) A raw image. B) The same image after normalizing the intensity and subtracting the background. C) The thresholded image. D) The image after multiplication using one of the region-defining masks.

background subtraction. The background was determined by using the *strel* function to exclude all objects that could not completely contain a disk of a certain radius. After trial and error, we determined that a disk with a radius of 5 pixels gave the best results. The result from these operations performed on the image in (A) are displayed in (B). We then applied thresholding to the image, setting the pixel values to 1 if they had intensity values greater than 0.3, and 0 if they had intensity values less than 0.3 (C). Finally, we multiplied the thresholded image by each mask in the set defined above (D shows the results from one mask). The density in each region defined by a mask was calculated by summing all the pixel values from the masked, thresholded image and dividing by the total number of pixels in that region. After performing these operations on each image in the time-lapse sequence, we plotted the density in each region over time. Note that the densities are only approximate since the cells may overlap in many of the images, reducing the number of pixels that are occupied by cells.

The idea behind this method of quantifying the data was that it would allow us to distinguish regions where the chemoattractant concentration and concentration gradient were optimal and would lead to the greatest cellular response. Cells within these regions would crawl up the gradient, moving into and increasing the density of new regions while reducing the densities in the regions from whence they came.

One of the problems with the method of mask production described above is that it produces large regions far from the micropipette tip, such as the one shown in Figure 3.7B, and small regions near the tip where the fluorescence intensity changes more dramatically. This greatly reduces the resolution for tracking density changes. The second method we used for quantifying the data is similar to the first method, but overcomes this

issue by defining annular regions based a series of concentric circles around the tip of the micropipette. As shown if Figure 3.9, below, this method enables us to track the densities with greater resolution, but it suffers from losing any relevance to the convective patterns displayed by the fluorescence intensity images. We will present and discuss, below, results from both methods.

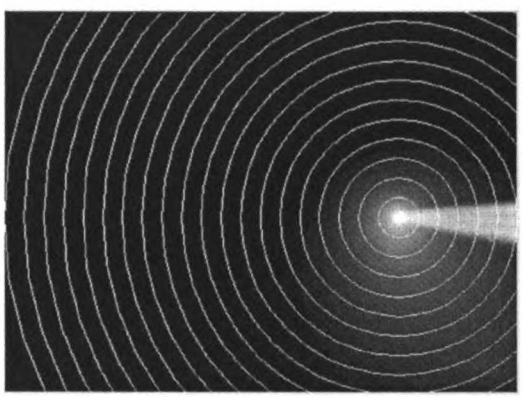

Figure 3.9: Concentric circles defining regions for tracking cell density superimposed on an intensity image averaged over 266 frames.

3.2.5 Parameter estimation

In the absence of data providing individual cell paths in chemoattractant gradients, it becomes difficult to estimate the chemotactic responsiveness parameter in the bias term of the modified OU process. Nevertheless, we present two measures here for use in future work for quantifying this parameter. We can also use these measures for exploring differences between simulations run under various conditions. To compare experimental results with model predictions we rely on qualitative similarity measures, as discussed in more detail below.

The first measure is the chemotactic index, discussed briefly in Chapter 1, defined as the ratio of the distance a cell migrates up a concentration gradient to the total path

length [McCutcheon, 1946]. This index takes values between -1, for a cell migrating directly against the gradient, to +1, for a cell migrating directly up the gradient. In ideal conditions of chemoattractant concentration and concentration gradient, we would expect the chemotactic index to be high. In non-optimal conditions, we would expect the index to be closer to 0, indicating that the cell has no directional preference.

The second measure is the correlation between the vector pointing in the direction of cell migration and the vector pointing in the direction of the chemoattractant gradient. This is fairly similar to the chemotactic index in that it will take a value of -1 for migration directly down the gradient and +1 for migration directly up the gradient. The advantage of this measure is that it can be used when there are changes in the chemoattractant gradient, caused either by experimental design or convective fluctuations.

To estimate the value of the chemotactic responsiveness we would apply the method described in [Stokes et al., 1991]. We first run a number of simulations using different values for the chemotactic responsiveness. We then calculate the simulated chemotactic indices or correlations and plot them against the chemotactic responsiveness. Once we have experimental data, we can calculate the measures above and reference the figures from the simulations to estimate the value of the parameter.

The parameters used in the model of receptor-ligand binding were obtained from literature estimates.

3.3 Experimental Results

The methods described above to process the experimental images were designed to provide objective measures that would be amenable to presentation and comparison with model predictions. While these methods were mostly successful, we include our interpretation of the results based on a qualitative analysis of the time-lapse sequences. One of the primary goals in performing these experiments was to estimate the chemotactic responsiveness in the bias term of the modified OU process. In light of the difficulties discussed above, we were unable to perform this task. We could, however, achieve another goal which was to qualitatively determine the degree of response in different concentrations and gradients. This is important for comparing the results to model predictions and for designing experiments to test the chemotactic response in multiple chemoattractant gradients, as will be discussed in the following chapter.

We measured the neutrophil chemotactic response in 10 experiments using different concentration of either fMLP or the C5a analogue ChaCha. The results for an experiment using 100 pM fMLP are displayed in Figure 3.10, on the following page. Each column corresponds to one of the methods discussed above for producing masks that define the regions in which cell densities were tracked. In (A) a contour plot of the fluorescence intensity is superimposed over the average fluorescence intensities from 77 frames taken with 15 second intervals. Each contour defines a region and the density in each region is tracked over time in (B). The ordinate of this plot does not give absolute values of the density, but is designed to enable comparisons of the relative densities in each region over time. The lines are ordered to correspond with the intensity values, so that the lowest line tracks the density in the largest and weakest intensity region and the

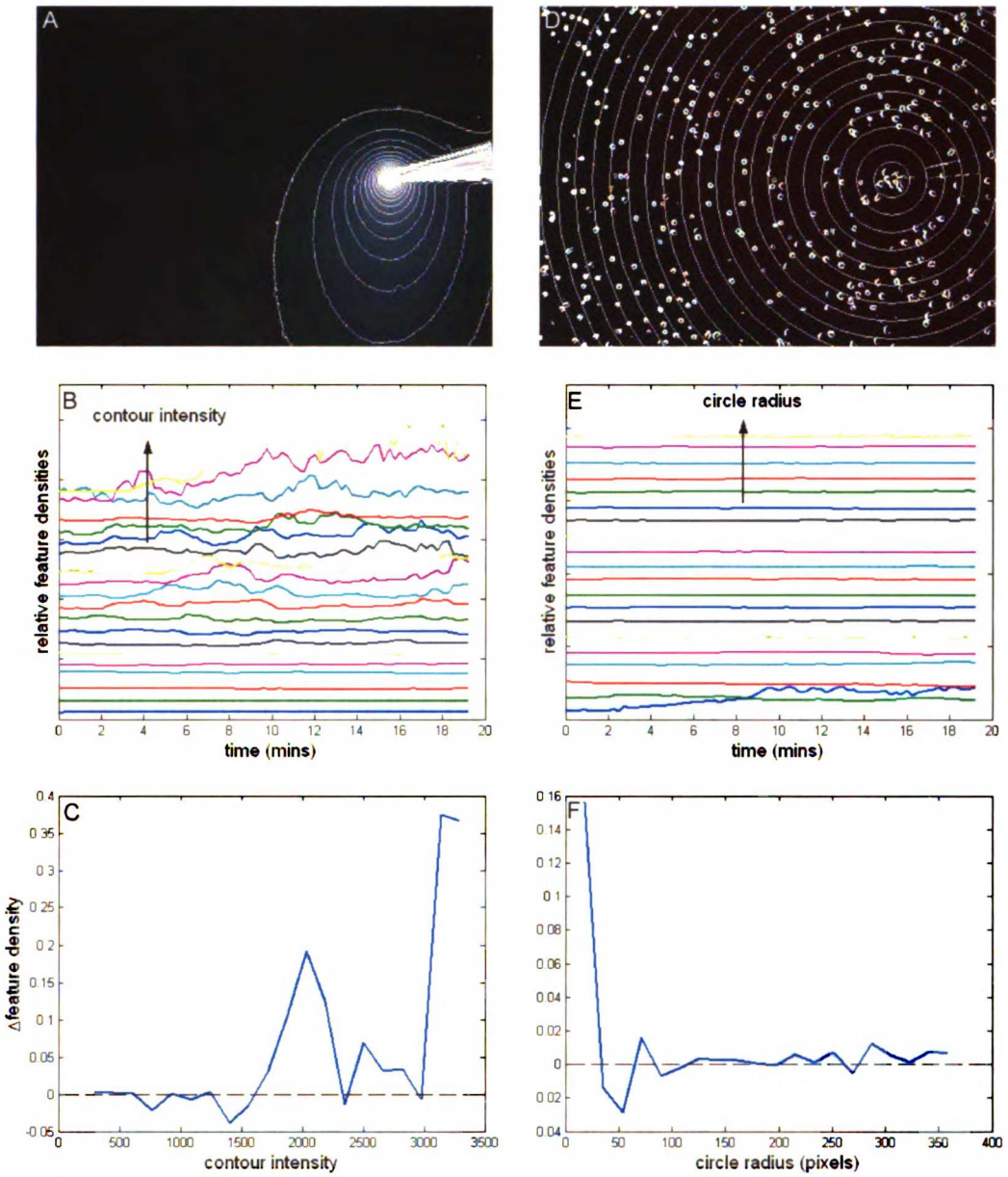

Figure 3.10: Results from an experiment to measure neutrophil migration to a micropipette releasing 100 pM fMLP. A) A contour plot of the fluorescence intensity superimposed on the average of 77 frames. B) The density of cells (features) over time in each of the contours. The ordinate is not absolute but is designed to enable easy visualization of the relative changes in densities. The lowest line corresponds to the weakest intensity contour, and the highest corresponds to the strongest intensity contour. C) The change in feature density between the first and last frames for each contour. D) The annular regions superimposed on the final thresholded image of the sequence. E) The density of features over time in each of annular regions. F) The change in feature density between the first and last frames for each annular region. Note that the behavior mirrors that in (C) because of how the regions are defined.

highest line tracks the density in the strongest intensity region. Notice that the biggest changes in density occur in the high intensity regions at the micropipette tip. This indicates that cells accumulated here. The total density change between the first and last frames in each region is plotted in (C). This figure shows more clearly that the cells accumulated in the region at the micropipette tip. There is also a significant density increase in a slightly weaker intensity region corresponding to 2000. This illustrates one of the difficulties in using this method: we are unsure of the position of this contour in the field without making a more detailed examination.

Figure 3.10 D-F shows the results when using the annular regions. In (D) the annular regions are superimposed over the final thresholded image. Notice that the feature (or cell) density in the smallest region at the micropipette tip appears to be high. The density in each annular region is plotted over time in (E) using the same style ordinate as in (B), except that the lowest line corresponds to the annular region with the smallest diameter near the micropipette tip and the highest line corresponds to the annular region with the largest diameter. Notice that the density in every region is relatively flat over time, except for the one with the smallest diameter. In (F), the density change between the first and last frame is plotted as a function of the radius of the circle defining the annular region. The result is an approximate mirror image of (C) because of the definitions of the regions in each case. This is perhaps the clearest figure, showing that the cell density increases right near the tip. There is also a slight decrease in the densities of a few regions just outside that may correspond to cells leaving these regions to crawl to the tip. In the regions farther from the tip there is a negligible response. The key result from this experiment is that at this concentration the response is confined to an area right

near the tip where the gradient and concentration is sufficiently large enough to generate a response. This was the lowest concentration in which we observed a response.

Figure 3.11, on the following page, displays the density changes between the first and last frames in the annular regions for four experiments in which different concentrations of fMLP were used in a micropipette. The plot in (D) for 1 mM of fMLP is representative of three different experiments using this same concentration. Notice that the y-axes are scaled differently in each plot. There appears to be an increasing trend between 10 nM and 100 nM and then a drop for the remaining experiments. Although this may be of significance, indicative of some sort of sensitivity of neutrophils, we did not perform enough replicates to predict a trend with any confidence. The plot in Figure 3.10F, above, uses a lower concentration than Figure 3.11A and shows a larger change in feature density, throwing off the small trend that we observe here. We did notice, however, that the response seemed to be the greatest when using 100 nM. This will be important in the next chapter. Note also that the total elapsed times over which the densities were tracked were different for each experiment. The results displayed above using 100 pM were measured from a time-lapse sequence over 19 minutes. The results displayed below were measured from sequences over 100 minutes for 10 nM, 86 minutes for 100 nM, 48 minutes for 1 μM, and 68 minutes for 1 mM. In general, we noticed a qualitative trend suggesting that the responses were faster at lower concentrations. This may be related to the increase in the number of bound receptors, as discussed in [Zigmond and Sullivan, 1979].

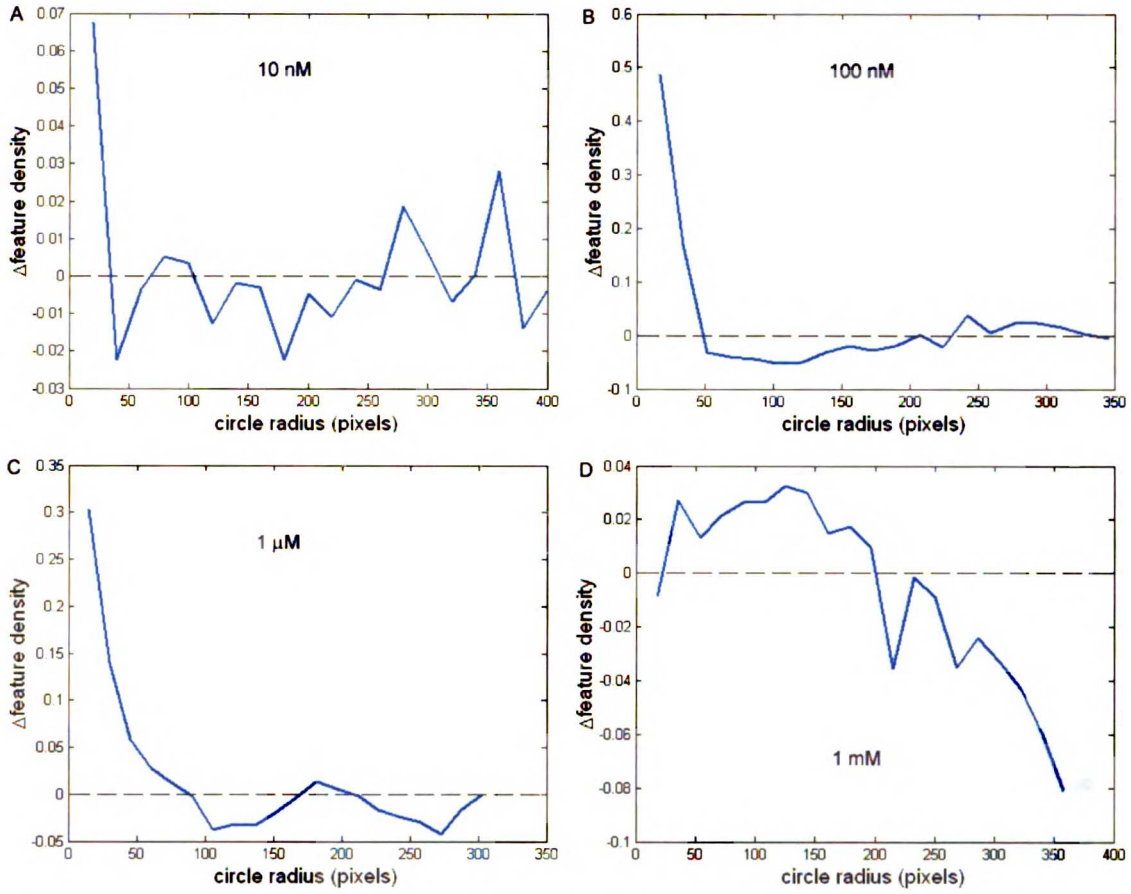

Figure 3.11: The changes in feature densities between the first and last images in the annular regions for four different experiments using A) 10 nM, B) 100 nM, C) 1 μM, and D) 1 mM of fMLP in a micropipette.

The trend we focused on in analyzing these sequences and developing the model is the region of sensitivity. At low concentrations, cells near the source crawled to the micropipette tip, while cells farther away ruffled but had little or no displacement. This can be seen in Figure 3.11A, B, and C where the peak density change occurs in the smallest annular region. As the concentration increases, the region in which the cells responded moved outward. This can be seen above by comparing the points where the largest peak first crosses the x-axis. At the highest concentration tested, 1 mM, the cells near the source either did not move or migrated in random directions, while the cells that

were farther away migrated inward. These inwardly migrating cells would seem to lose their sense of direction or stop when they got within a certain distance of the micropipette tip. Notice that the greatest response in (D) occurs in the region farthest from the micropipette tip, while there is a low response at the tip. The reason for the low response may be due to receptor saturation. Figure 3.12, below, shows the final thresholded images from the experiments using 100 nM (A) and 1 mM (B) with the annular regions superimposed and further demonstrates the trend we observe. The smallest circle is very dense with cells in (A) and nearly empty in (B). The maximum density in (B) appears to fall in the 6th region from the micropipette tip.

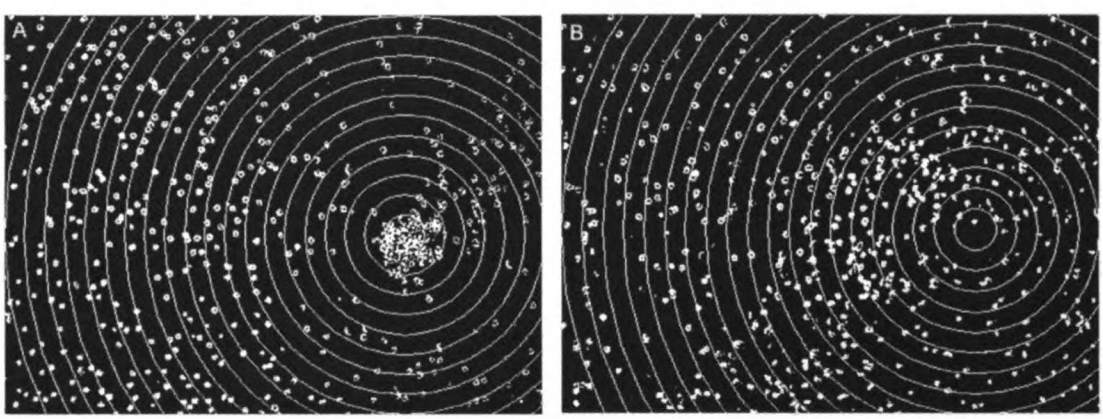

Figure 3.12: The final thresholded images from the sequences using A) 100 nM and B) 1 mM fMLP with the annular regions superimposed.

We could only observe a response to ChaCha at the highest concentration tested, which was 10 mM. This may indicate that the optimal concentration is actually higher. There is some indication in the literature that other C5a analogues sharing a similar sequence to ChaCha can act as partial agonists or even antagonists. This would indicate that they have a lower affinity for the C5a receptor, which would explain our results. The

response consisted of cells near the source crawling to the micropipette tip, much as they did for the lower fMLP concentrations used above.

3.4 Model and Simulation

In this section we develop the OU process to account for chemotaxis in a single chemoattractant gradient. We begin with a model of the chemoattractant gradient and compare this model to experimental data. We then present several models for the chemotactic bias term, looking strictly at the deterministic behavior in light of the physics involved in receptor-ligand binding. Finally, we add the bias term to the OU process and simulate migration paths of cells in a chemoattractant gradient.

3.4.1 The concentration profile

Chemoattractant release from a micropipette can be modeled as a point source of in three dimensions. For this model, we will neglect any effect on the concentration by the presence of the micropipette or by convection. Due to spherical symmetry, we only consider the radial dimension. To describe the resulting concentration profile and gradient we start with the steady state diffusion equation in spherical coordinates, given by

$$\frac{\partial}{\partial r}\left(r^2 \frac{\partial L}{\partial r}\right) = 0 \qquad (3.4.1)$$

where L (nM) is the chemoattractant concentration and r (μm) is the radial distance from the source. The concentration is L_0 (nM) within the point of radius a_0 (μm) and decays to

zero in the limit as the radius goes to infinity. Under these boundary conditions, the solution to Eq. (3.4.1) is

$$L = \frac{L_0 a_0}{r} \qquad (3.4.2)$$

If we define q (mole/s) as the rate of flow of chemoattractant from the micropipette and set it equal to $4\pi D L_0 a_0$, where D ($\mu m^2/s$) is the chemoattractant diffusivity, we get the equivalent statement [Berg, 1993]

$$L = \frac{q}{4\pi D r} \qquad (3.4.3)$$

We are interested in finding the concentration and concentration gradient experienced by a cell that is crawling in a plane within the three dimensional field. To account for the barrier to diffusion caused by this plane we use the Method of Reflection and Superposition [Crank, 1975]. This method, which is outlined in Figure 3.13 on the following page, places an imaginary point source on the opposite side of and equidistant from the plane, i.e. the reflection of the real source within the plane. The concentration at any point is then found by summing the concentrations resulting from the real and imaginary point sources. The net result is that Eqns. (3.4.2) and (3.4.3) are multiplied by a factor of 2. Since we only consider the two dimensional plane, we will fix z, the distance between the source and the plane, so that r varies only with the x and y coordinates.

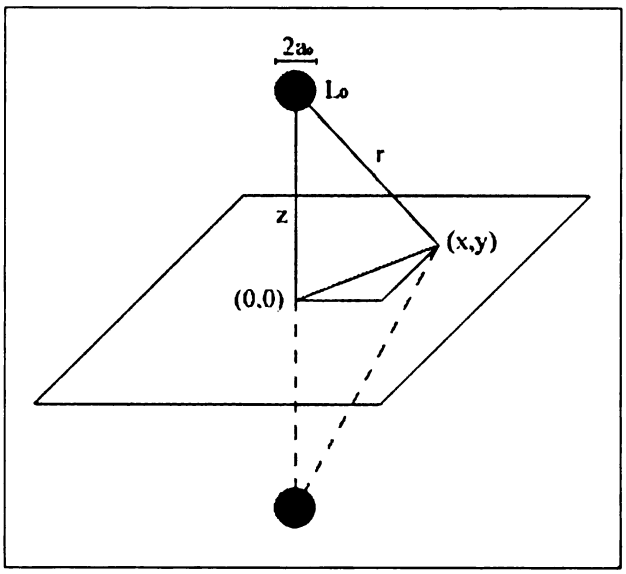

Figure 3.13: Method of mirror images used to calculate the chemoattractant concentration and concentration gradient on a plane resulting from a point source above the plane.

For clarity, we will limit our examination at this point to a line within the plane. We define this line as the x-axis and place the origin of the axis directly below the source so that $r = \sqrt{x^2 + z^2}$ along the line. Figure 3.14 on the following page, shows a diagram of this model. The ligand concentration along the line is then given by

$$L = \frac{2L_0 a_0}{\sqrt{x^2 + z^2}} \qquad (3.4.4)$$

The gradient of ligand along the line is found by differentiating Eq. (3.4.4) to give

$$\frac{dL}{dx} = -\frac{2L_0 a_0 x}{\left(\sqrt{x^2 + z^2}\right)^3} \qquad (3.4.5)$$

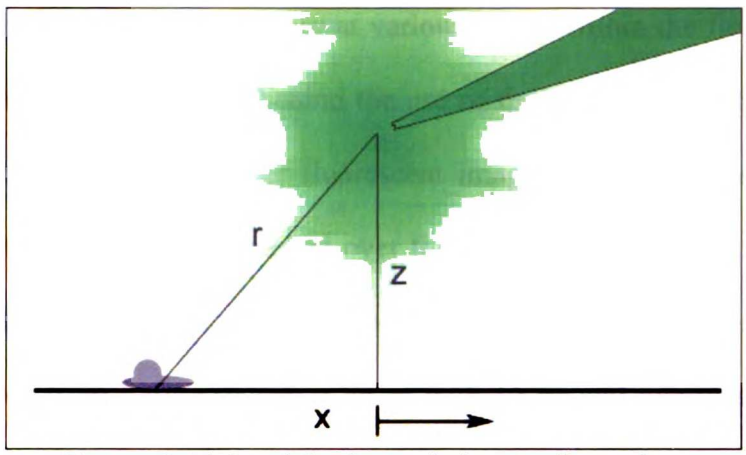

Figure 3.14: Model schematic in one dimension.

Before proceeding, we validate this model against experimental data obtained from a fluorescent image. Figure 3.15A, below, shows an image with a vertical line drawn through the intensity peak. The intensity along this vertical line (with the background intensity subtracted) is plotted as a solid blue line in Figure 3.15b. The dashed red line superimposed over the blue line is the intensity predicted by Eq. (3.4.4) when we substitute I (the intensity) for L and set a_0 to 4.5 μm and z to 9 μm. The peak intensity I_0, determined from the data, is equal to 3567.

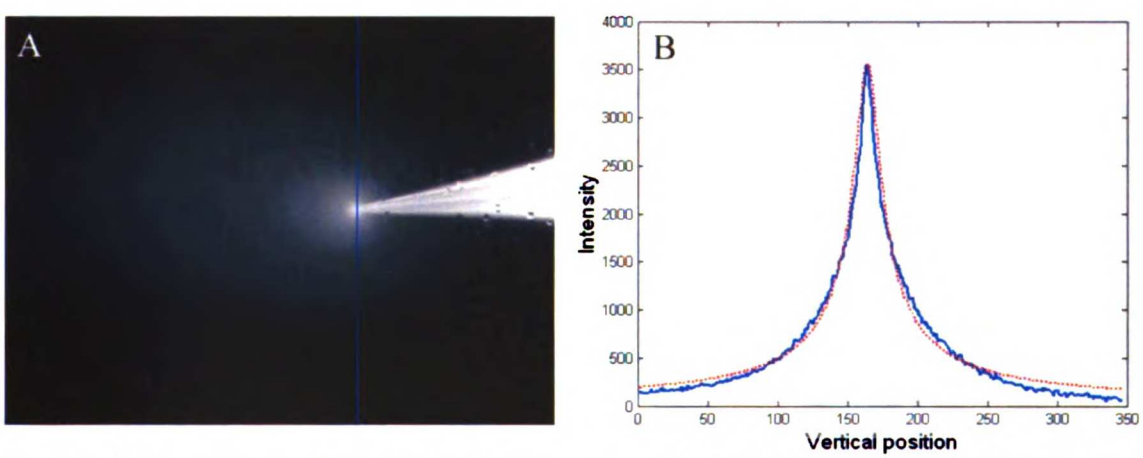

Figure 3.15: A) A fluorescent image of carboxyfluorescein diffusing from a micropipette. The vertical blue line is drawn through the intensity peak. B) The intensity along the vertical line in (A) is plotted against the vertical position as a solid blue line. The dashed red line is the intensity predicted by the model.

By measuring the fluorescence intensity at various points within the field over time, we can also examine the assumptions behind the use of the steady state diffusion equation. Figure 3.16A, below, shows another fluorescent image. The intensities at four points, each marked by a colored x, are tracked over the time course of an experiment and the results are plotted using corresponding colors in Figure 3.16B. The x-axis in this figure is the frame number from a time sequence taken with 15 second intervals. As shown, we see that there is no significant buildup of fluorescence over time, indicating that the dimensions of the device in which these images were taken are large enough to justify diffusion to an infinite radius. Notice the point and corresponding line marked by the number 1 in this figure. The fluctuations in the intensity correspond to convection that occurred over the course of this time sequence. As mentioned above, we neglect this convection in the model.

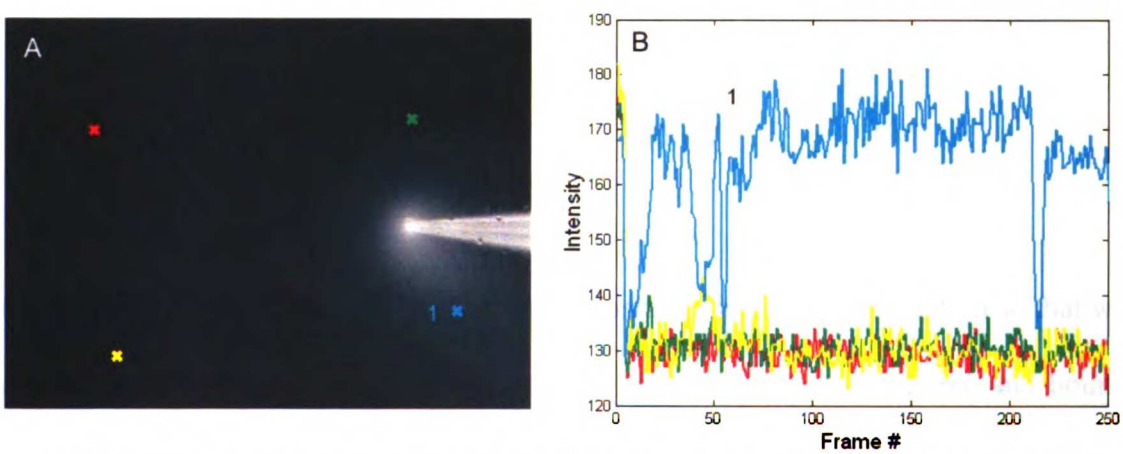

Figure 3.16: A) A fluorescent image of carboxyfluorescein released from a micropipette. B) The intensities at each of the four points marked in (A) are plotted for each frame of a time-lapse sequence of images taken at 15 second intervals.

3.4.2 Models for chemotactic bias

To model gradient sensing by neutrophils we use a simple description of receptor-ligand binding, as follows

$$R + L \underset{k_u}{\overset{k_b}{\rightleftharpoons}} C \qquad (3.4.6)$$

where R (#/cell) is the number of free receptors, L (nM) is the concentration of ligand, C (#/cell) is the number of bound receptors, and k_b ($nM^{-1}\ s^{-1}$) and k_u (s^{-1}) are the binding and unbinding rate constants, respectively. The species in this reaction depend on both time and space. Since we only consider one spatial dimension, the number of bound receptors is technically described as $C(x,t)$. For simplicity we will drop this explicit description.

The rate of change in the number of bound receptors is described using mass-action kinetics to give

$$\frac{\partial C}{\partial t} = k_b RL - k_u C \qquad (3.4.7)$$

We neglect other dynamics such as receptor desensitization and internalization so that we can describe the total number of receptors, R_{tot} (#/cell), as the sum of free and bound receptors, as follows

$$R_{tot} = R + C \qquad (3.4.8)$$

Using the initial condition that $C(x,0)=0$, we solve Eq. (3.4.7) to give

$$C = \frac{k_b R_{tot} L}{k_b L + k_u}\left(1 - e^{-(k_b L + k_u)t}\right) \qquad (3.4.9)$$

The time constant, $(k_b L + k_u)^{-1}$ (s), gives the time at which the number of bound receptors is equal to 63% of its steady state value. Given values for k_b on the order of 0.1 nM^{-1} s^{-1}, k_u on the order of 1 s^{-1} [Adams et al., 1998], and L on the order of 100 nM, we calculate a time constant of 0.1 s. The average speed of a neutrophil is 10 μm/min and its diameter is 10 μm, so we expect that it will crawl about $1/600^{th}$ of its diameter in one time constant. With this small value we are justified in neglecting transients in the species concentrations, and we can thus describe the number of bound receptors as

$$C = \frac{R_{tot} L}{K_D + L} \qquad (3.4.10)$$

where we have used the dissociation constant $K_D = k_u / k_b$ (nM).

We assume that the cell detects the chemoattractant gradient by measuring the difference in the number of bound receptors across its length, as discussed in [Zigmond, 1981]. We will define the magnitude of this difference as the sensitivity and use both terms interchangeably. To determine the difference, the gradient of receptors along the x-

axis is first found by differentiating Eq. (3.4.10) with respect to L and then multiplying by the ligand gradient given in Eq. (3.4.5) above. The result is

$$\frac{\partial C}{\partial x} = \frac{\partial C}{\partial L}\frac{dL}{dx} = -\frac{2R_{tot}K_D L_0 a_0 x}{\left(K_D + L\right)^2 r^3} \qquad (3.4.11)$$

The difference is then found by multiplying this equation by the diameter of the cell, d_{cell}, to give

$$\Delta C = d_{cell}\frac{\partial C}{\partial x} \qquad (3.4.12)$$

The sensitivity is just the absolute value of the difference defined by this equation. The diameter of the cell acts here as an amplification factor and suggests that larger cells can detect smaller gradients. Small cells, such as bacteria, may not be able to detect a spatial gradient across their diameters and may use a temporal sensing mechanism instead [Berg and Purcell, 1977; Dusenbery, 1998; Thar and Kuhl, 2003].

Figure 3.17A on the following page, shows the resulting difference in the number of bound receptors across a cell at different positions along the x-axis for three different source concentrations of chemoattractant. The parameter values we used are presented in Table 3.1 (Matlab code can be found in appendix A.3). We assume that the cell migrates in the direction indicated by the difference: when the difference is positive, as occurs to the left of the origin, the cell migrates in the positive x direction; when the difference is negative, as occurs to the right of the origin, the cell migrates in the negative x direction.

By examining this figure in light of the experiments discussed in section 3.3, above, we find a partial similarity with our desired outcome. On the low end of concentrations we see that there is a small region around the origin that directs cells to the source. Although not pictured here, at even lower concentrations the difference in bound receptors is reduced so that eventually it will be so small that the cell will be unable to accurately sense the gradient. Based on observations in [Zigmond, 1977], we assume that the minimum difference in the number of bound receptors is approximately equal to 10. As the concentration is increased to 100 nM, the region around the source expands outward and the difference increases.

Table 3.1: Parameter values used in the models of chemotactic bias.

Parameter	Value	Parameter	Value
L_0	1 nM, 100 nM, 10 μM	R_0	1000/cell
a_0	4.5 μm	K_D	10 nM
z	9 μm	d_{cell}	10 μm
α_L	0.0008 μm^{-2}	n	1.2

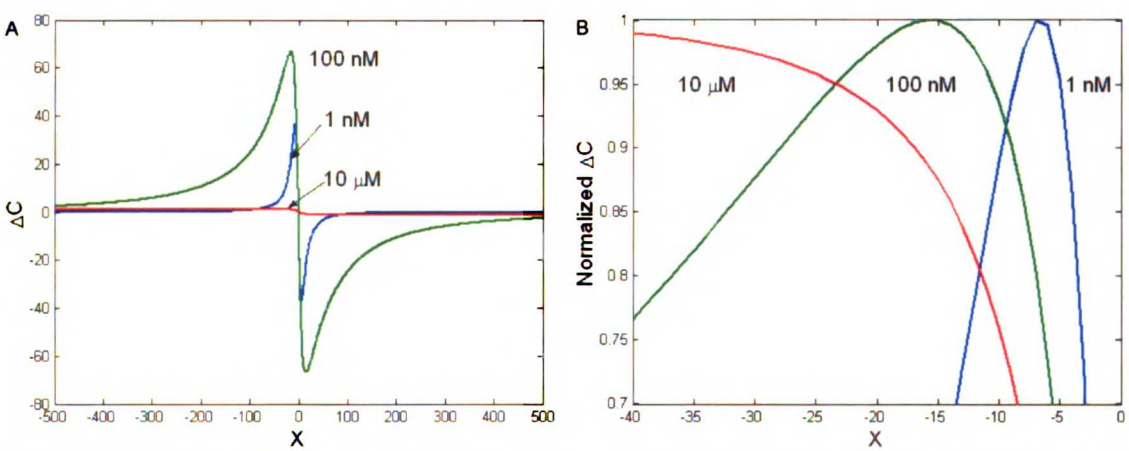

Figure 3.17: A) The difference in the number of bound receptors that would occur across a cell located at points along the x-axis for three different source ligand concentrations. B) The normalized difference from (A) for the same three concentrations in a smaller region along the x-axis.

We do not find agreement with experimental results at higher concentrations. We expect the sensitivity to be low near the source due to receptor saturation and higher with a larger range away from the source. We see instead that the sensitivity decreases uniformly and may fall below the minimum detectable level. Figure 3.17B shows a portion of the x-axis with sensitivities for the different concentrations normalized by dividing through by their maximum values along the axis. Although we do not know of a mechanism by which this normalization would occur, we see that this gives greater similarity with experimental observations. If, for instance, the cell requires a minimum normalized difference of 0.7, the smallest value on the ordinate in this figure, then the sensitivity is lower near the source and higher with a larger range away from the source. The sensitivity near the source is still too high, however, and as the concentration is increased even further in the model, an asymptotic limit is reached that is close to the line shown for 10 μM in Figure 3.17B.

Another model that was suggested in [Zigmond, 1981] suggests that neutrophils perform gradient detection by sensing the relative difference in the number of bound receptors across their length. The relative difference is found by dividing the absolute difference from Eq. (3.4.12) by the total number of bound receptors from Eq. (3.4.10), giving

$$\frac{\Delta C}{C} = -\frac{2K_D x}{(K_D + L)r^2} \qquad (3.4.13)$$

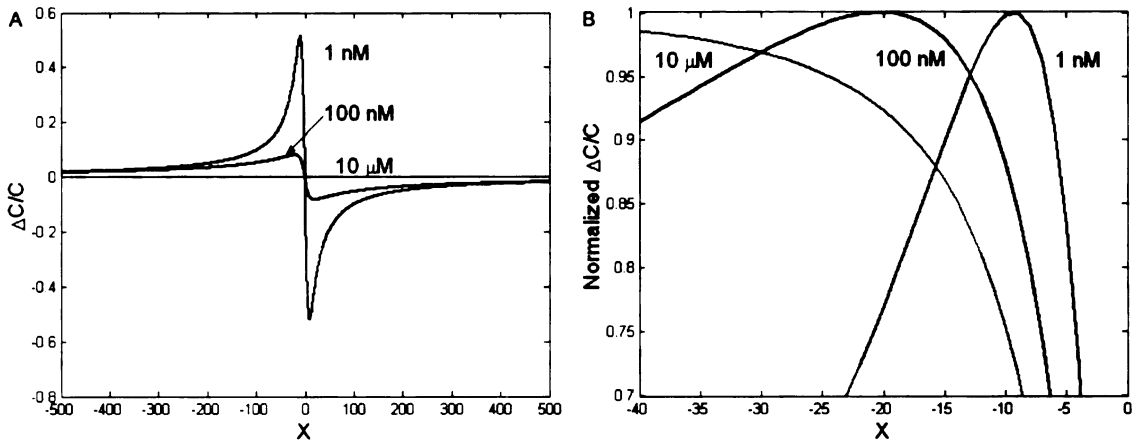

Figure 3.18: A) The relative difference in the number of bound receptors that would occur across a cell located at points along the x-axis for three different source ligand concentrations. B) The normalized relative difference from (A) for the same three concentrations in a smaller region along the x-axis.

Figure 3.18A shows the relative difference along the x-axis for the same three chemoattractant concentrations used previously. We see here that the sensitivity is highest at the lowest concentration and decreases as the concentration increases. The region of sensitivity follows a similar trend. This does not agree with experimental results. Figure 3.18B shows a portion of the axis with normalized relative sensitivities. In comparing this with Figure 3.17B, we see that this normalization again achieves greater similarity with experimental observations. Note also that the locations of the peaks have shifted away from the source relative to those in Figure 3.17B. While we may be safe in rejecting gradient detection via a strictly relative difference, the normalized relative difference remains a viable option. As above, we do not know of a mechanism by which this can occur.

Another consideration for possible models of gradient detection is similar to the first model with an additional mechanism for receptor desensitization. We replace R_{tot} in Eq. (3.4.10) with R_0 (#/cell), the number of available receptors for binding, given by

$$R_0 = \frac{R_{tot} K^n}{K^n + L^n} \qquad (3.4.14)$$

This functional form is based on intuition: at high chemoattractant concentrations we expect more receptors to become desensitized so that fewer are available for binding and downstream signaling. The Hill coefficient, n, allows us to tune the level of desensitization. The number of bound receptors in this desensitization model, C_d, is then given by

$$C_d = \frac{R_0 L}{K_D + L} \qquad (3.4.15)$$

The gradient of bound receptors is found here, as above, by differentiating Eq. (3.4.15) with respect to L and multiplying by the chemoattractant concentration gradient to give

$$\frac{\partial C_d}{\partial x} = -\frac{R_{tot} K^n L x \left[K_D K^n - (n-1) K_D L^n - n L^{n+1} \right]}{(K_D + L)^2 \left(K^n + L^n\right)^2 r^2} \qquad (3.4.16)$$

The absolute difference is then found by multiplying by d_{cell}.

Figure 3.19A shows the difference in the number of bound receptors across the cell along the x-axis with desensitization for the three different chemoattractant concentrations examined above. We see here an odd twist that is not surprising on further examination of this model. At low concentrations we get the expected behavior: cells

near the origin migrate inward. As the concentration is raised, however, the direction of migration is reversed; cells will move away from the source. Figure 3.19B shows the normalized results over a smaller region of the axis. The reason this reversal is not surprising is that the end of the cell closest to the source is exposed to a higher chemoattractant concentration and will have fewer receptors that are available for binding and signaling due to greater desensitization. The gradient of bound receptors is thus inverted, causing the cells to migrate away from the source. The concentration at which this inversion occurs depends on the particular value for n that we choose. Unlike the previous results, the normalized difference in Figure 3.19B does not provide greater similarity with experimental observation.

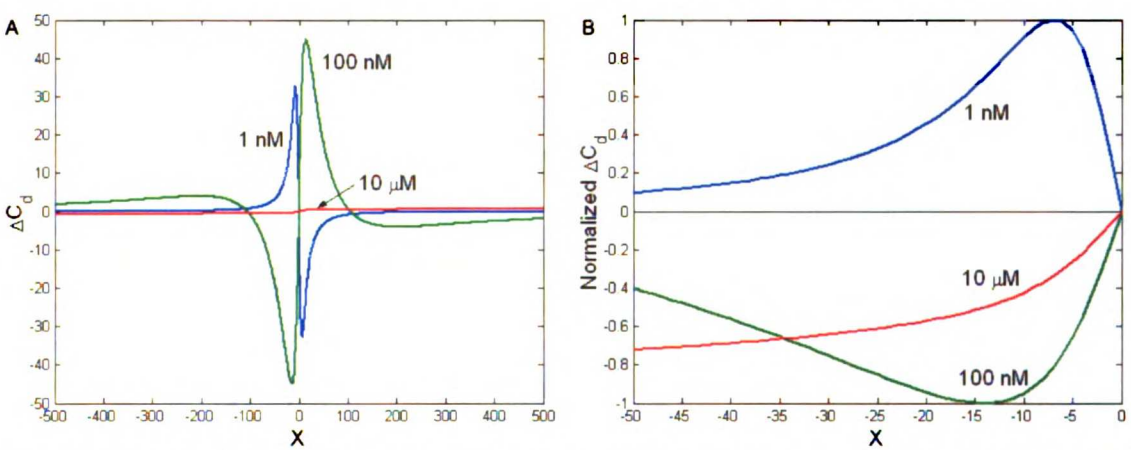

Figure 3.19: A) The difference in the number of bound receptors that would occur across a cell located at points along the x-axis for three different source ligand concentrations when a simple sigmoid function for receptor desensitization is included. B) The normalized difference with desensitization from (A) for the same three concentrations in a smaller region along the x-axis.

The final model we consider here uses the first receptor-ligand binding scheme described by Eq. (3.4.10) with a modified description of the ligand concentration. The ligand concentration is given by

$$L = L_0 \, e^{-\alpha_L r^2} \qquad (3.4.17)$$

where α_L (μm^{-2}) is a scaling factor related to the chemoattractant diffusivity. Although this equation does not solve the diffusion equation and does not provide the best fit with experimental data from the fluorescent images, it does roughly approximate our previous description of the ligand concentration, as shown in Figure 3.20, below. Notice that the peak has a greater spread and the concentration decays more quickly.

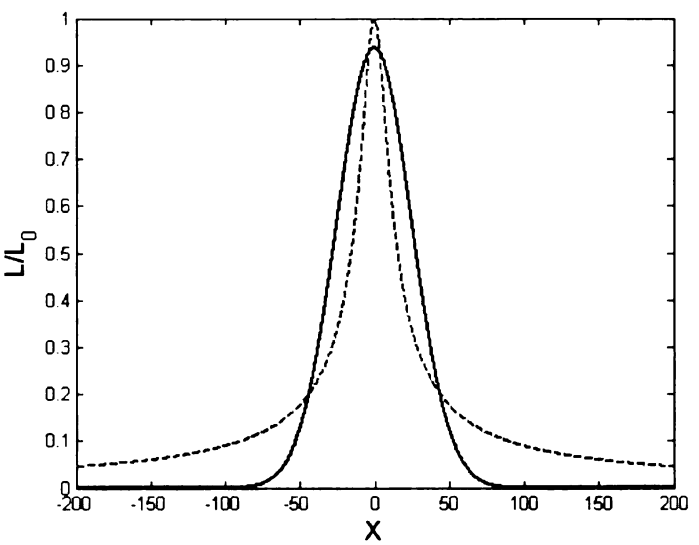

Figure 3.20: Comparison of two models for the chemoattractant concentration profile. The dashed red line is the model derived from the diffusion equation. The blue line is the exponential approximation.

The difference and normalized difference in the number of bound receptors across the cell for this model are displayed in Figure 3.21. This model agrees with experimental results in that the sensitivity increases with increasing concentration. There should, however, be an upper limit on this sensitivity based on the number of receptors; this limit is exceeded at very high concentrations (not shown). Nevertheless, the region of sensitivity does move outward at higher concentrations and is low near the source. This is caused by the inflection point in the exponential model for the chemoattractant concentration. The peak in the sensitivity actually occurs at the same position as the inflection point. While this model does not entirely agree with the experimental results, it does provide important insight that can be used in future development. A combination of this result with the relative difference or desensitization models described above may provide better agreement.

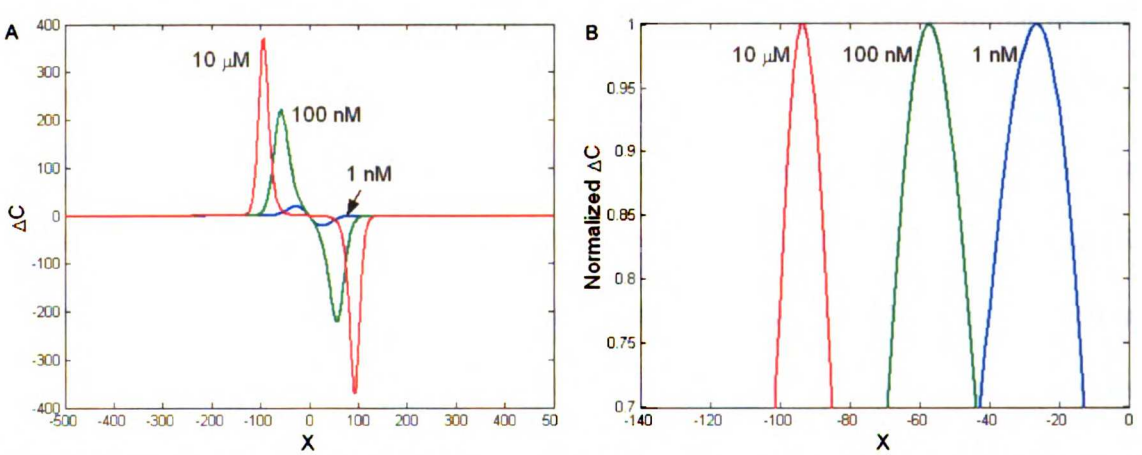

Figure 3.21: A) The difference in the number of bound receptors that would occur across a cell located at points along the x-axis for three different source ligand concentrations that have exponential profiles. B) The normalized difference from (A) for the same three concentrations in a smaller region along the x-axis.

The ligand concentration described by Eq. (3.4.17) cannot be derived from the steady state diffusion equation and does not agree with the fluorescence data, but the assumptions we made in developing the first concentration model may be incorrect. It is possible that we need to account for differences between the fluorescence and chemoattractant profiles. We may also need to account for effects on the concentration caused by the micropipette, convection, and/or injection of chemoattractant.

3.4.3 Simulating chemotaxis using the OU process

In spite of the difficulties discussed in the previous section for achieving agreement between the model for the chemotactic bias and the experimental results, we develop here a simulation of the modified OU process described by Eq. (3.1.1). While we do not make a detailed examination, it is possible that closer agreement can be attained by accounting for a dependence of the speed and persistence time on the chemoattractant concentration. The basic framework presented here enables an integrated exploration of the effects of the physical processes presented thus far on chemotaxis.

The basic steps for simulating the modified OU process are fairly similar to those steps used for simulating the simple OU process. In Chapter 2, we used Eqs. (2.2.6) and (2.2.7) to update the x components of the velocity and position, respectively, and similar equations to update the y components of the velocity and position. In the modified OU process, we include updating equations for the states involved in the chemotactic bias term. These states include the chemoattractant concentration, the number of bound receptors, and the x and y components of the chemoattractant concentration gradient and bound receptor gradient. Depending on the model we use for the chemotactic bias we might also include the number of available receptors. While the velocity and position

depend on their previous values, these additional states depend only on the current position of the cell. The values of the states are calculated based on the equations described above and the result is fed into the modified OU process via the chemotactic bias.

Figure 3.22, on the following page, shows the results of simulations run using the above algorithm for 10 cells in three different chemoattractant concentrations over 17 minutes (Matlab code can be found in appendix A.4). The model is the normalized bound receptor gradient resulting from an exponential chemoattractant concentration, as shown in Figure 3.21B, above. The parameter values correspond to the speed and persistence used in the simulations in the previous chapter and those displayed in Table 3.1. The value for the chemotactic responsiveness was set to 2×10^{-6} μm/s/#/cell. The cells started from the green dot in each plot and the sources were located at the red dot. Note the concentration dependence on the cell migration paths. At the lowest concentration of 1 nM (A), the cells seem to be unable to sense the gradient and migrate randomly. At the middle concentration of 100 nM (B), most of the cells sense and migrate up the gradient. At the highest concentration of 10 μM (C), the cells from (B) that migrated to the point do not migrate as closely due to receptor saturation. Those cells that remained at a distance from the source in (B) are more attracted to the higher concentration in (C) because they are located within the range of greatest sensitivity which has moved outward at this higher concentration.

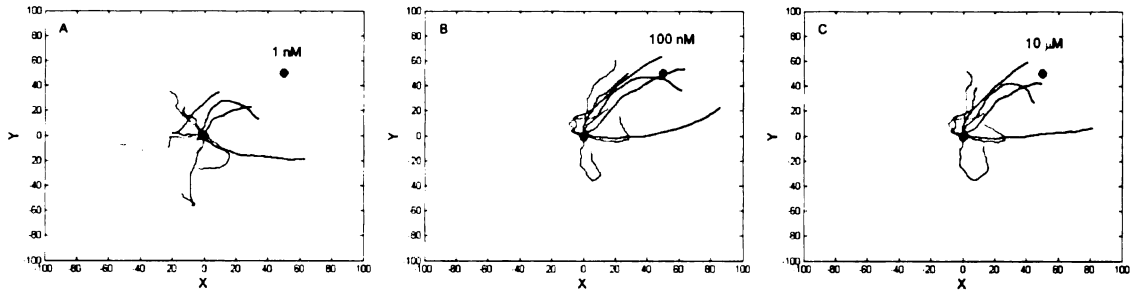

Figure 3.22: Simulated migration paths of 10 cells over 17 minutes in three different chemoattractant concentrations using the OU process with chemotactic bias. The green dots are the starting locations and the red dots are the chemoattractant source locations. The model for the chemotactic bias is the normalized bound receptor gradient resulting from an exponential chemoattractant concentration.

3.5 Conclusions

In this chapter we have developed the modeling framework based on the OU process to account for neutrophil chemotaxis in single chemoattractant gradients using a combination of experiments and models. We presented three different experimental assays that can be used to study chemotaxis: microfluidics devices, the Zigmond chamber, and the micropipette assay. While we were unable to use the microfluidics devices and Zigmond chamber for reasons we discussed, we have outlined their operation and have characterized fluorescent gradients generated within them. We focused our experimental lens on the micropipette assay, developing novel image processing methods for quantifying cell density changes and relating these changes to the chemoattractant gradient as monitored by inclusion of a fluorescent tracer. Although we were unable to track individual cells in these experiments, we present several methods for estimating model parameters based on cell migration paths that may be of use in the future. Using the experimental results which we obtained using the density tracking methods we examined several hypotheses for gradient sensing based on the physical principles

involved in receptor-ligand binding. While we were unable to achieve complete agreement between the experiments and the models, we did show partial agreement that provides important insight toward future development. Finally, we added a model of chemotactic bias to the OU process and demonstrated how simulations can be performed.

Chapter 4

Neutrophil Chemotaxis in Multiple Chemoattractant Gradients

4.1 Introduction

As discussed in Chapter 1, neutrophils are able to process and respond to conflicting gradients of chemoattractants in search of primary sites of inflammation. While much of the focus of research in this field has been on the molecular interactions and signaling pathways involved in the response to single gradients, how these pathways process multiple signals to effect migration in the appropriate direction is not understood and is an important line of questioning for understanding the organization and functioning of these signaling pathways. Although there are still numerous questions about how neutrophils respond to single gradients, as discussed in Chapter 3, we present here our efforts to expand the OU process to enable an examination of possible mechanisms behind multiple signal processing. In particular, we focus on effects on the direction of migration caused by differences in receptor-ligand binding parameters between two different chemoattractants. We assume that the chemotactic response is generated along the vector sum of bound receptor gradients and that this vector sum is weighted by differences in receptor-ligand binding.

The organization of this chapter largely parallels that of Chapter 3. We describe experimental methods for generating conflicting chemoattractant gradients and adapt

techniques presented earlier for processing experimental images. We demonstrate the application of these techniques and interpret the results from a couple of experiments. We then present models for the chemotactic bias and explore the effects of different binding parameters on the vector sum migration. Finally, we add the chemotactic bias to the OU process and simulate cell migration paths in multiple chemoattractant gradients. We discuss questions arising from this examination and make recommendations on how to further develop this modeling framework.

4.2 Materials and Methods

Most of the methods described in the previous chapter were used here without modification. The exceptions were in the micropipette assay and the image processing techniques, as discussed below.

4.2.1 Chemoattractant gradients

Microfluidics devices

Before discarding the microfluidics devices for reasons discussed in the previous chapter, we characterized opposing linear gradients of the fluorophores Texas Red and FITC. To generate opposing linear gradients, we fed 10 μM solutions of FITC and Texas Red into the opposite two outer entry ports of the device (see Figure 3.2), and a solution containing 5 μM of both fluorophores into the central entry port. The results are displayed in Figure 4.1. Note that, as in Figure 3.3, only a portion of the entire width of the main chamber is visible under 10x magnification. In (A), an overlay of two fluorescent images taken from different channels is displayed. The intensities are plotted across the width of the channel in (B).

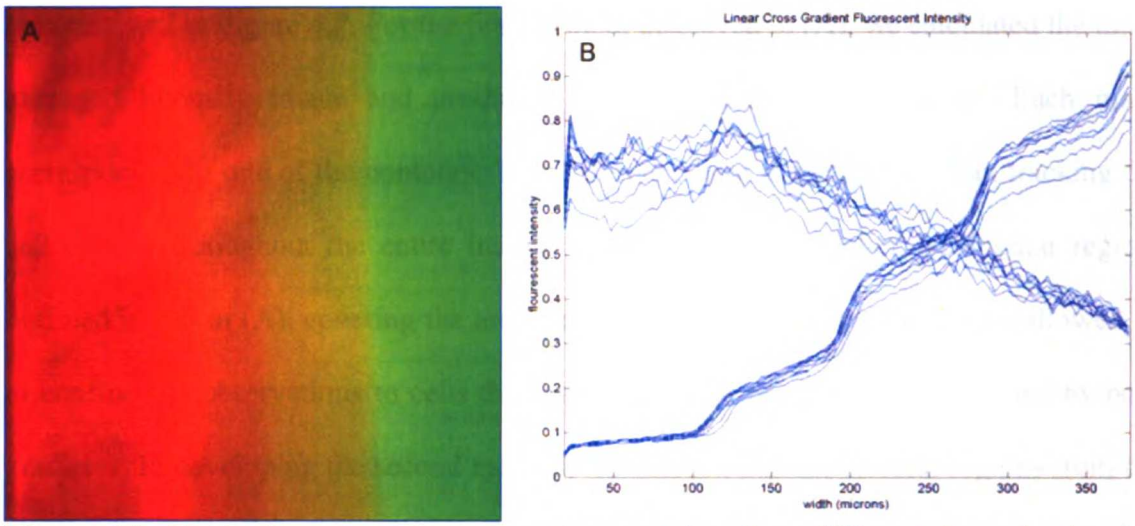

Figure 4.1: A) Overlay of two fluorescent images taken from different channels showing opposing gradients in a microfluidics device. B) The superimposed fluorescence intensity profiles measured from (A).

Micropipette assay

Micropipettes were pulled and loaded as described in the previous chapter. Micromanipulators were placed on either side of the microscope stage, and two micropipettes containing fMLP or ChaCha were positioned in the plane of focus. The release rates were controlled by separate pressure regulators. We occasionally increased or decreased the pressure on one or both lines to achieve good profiles that were fairly identical. We were also able to adjust the positions of the micropipettes dynamically, offering a significant advantage over previous assays used to study migration in multiple chemoattractant gradients. Although we do not examine these temporal effects here, the results presented below were obtained by actively positioning the micropipettes relative to each other until we were satisfied that a population of cells could sense both gradients.

4.2.2 Image processing

We used two methods, similar to the methods presented in the previous chapter, to generate masks to define regions for tracking cell densities. Examples of both methods

are presented in Figure 4.2. For the first method, displayed in (A), we calculated the time-averaged intensity image and produced a contour plot, just as above. Each mask corresponded to one of the contours. The difference here is that, rather than tracking the cell density throughout the entire image, we focused on a smaller rectangular region, outlined in red in (A), covering the area between the two micropipettes. This allowed us to confine our observations to cells that, we felt, would be more fully impacted by both gradients. In developing the second method, we decided that the circular regions from the previous chapter would be insufficient due geometrical constraints. Instead, we formed a series of rectangular regions between the two micropipettes, as displayed in (B). For both methods, we defined and tracked the cell density in each of 20 different regions. The density in each region was calculated as described in Chapter 3. Matlab code implementing these techniques is included in appendix A.1.

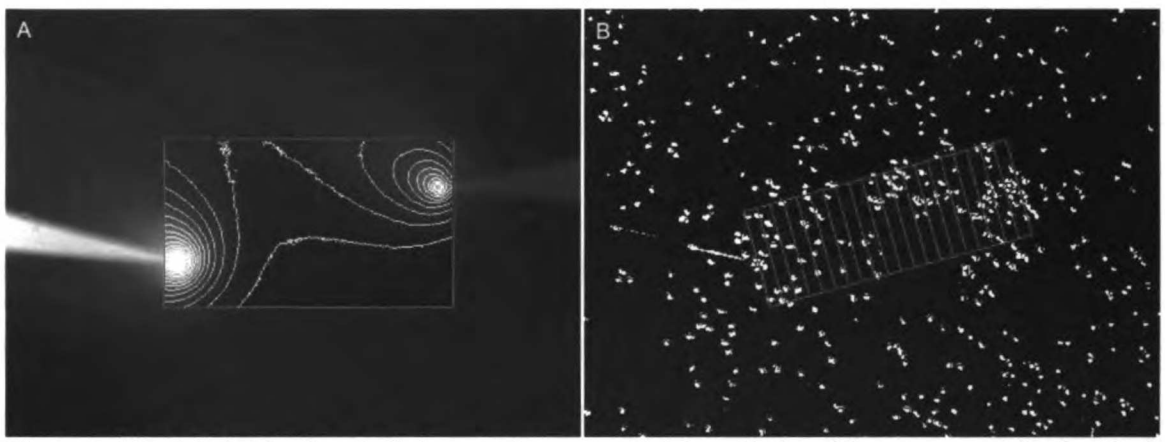

Figure 4.2: Methods for defining regions in which cell densities were tracked. A) A contour plot in a rectangular region covering the area between the micropipettes superimposed on a time-averaged fluorescence intensity image. Each contour defines one region. B) The area between the two micropipettes in (A) is divided into smaller horizontal rectangular regions that are approximately parallel to the gradients. These regions are superimposed on the final thresholded image in a time-lapse sequence.

4.3 Experimental Results

Figure 4.3 shows the results from an experiment using micropipettes containing 1 μM of fMLP and 10 mM of ChaCha, separated by a distance of approximately 400 μm. Each column corresponds to a method and image displayed in Figure 4.2. The fMLP was on the left and the ChaCha was on the right. In (A), the density is tracked in each contour over time. Note that these results come from a 20 minute experiment. The ordinate is not the absolute density but provides easy comparison between contours. The highest intensity contours, on the top, increased in density, and the lowest intensity contours stayed relatively flat. This indicates that cells crawled to one or both micropipettes. Figure 4.3B displays the density difference between the last and first frames for each contour. One of the issues in using this method is that it does not distinguish whether the cells crawled to the left or to the right, which is the primary information we desire. This is because many of the regions contain elements near both micropipette tips.

The second method solves this problem. Figure 4.3C shows the density difference over time in the rectangular regions. The ordinate is the same as in (A). The lower line indicates the rectangular region on the right in Figure 4.2, while the higher line indicates the region on the left. The density increases slightly on the ends and appears flat in the middle. The difference in each region is displayed in (D), where the behavior is more clearly observed. Since the density decreases in the middle and increases on both ends, we see that the cells crawled out of the middle and toward each chemoattractant. Since we do not observe prioritization of fMLP, as discussed in Chapter 1, we can conclude that it may not occur at all or that it may not occur over the distances used here. We will explore the distance variable in the models presented in the next section.

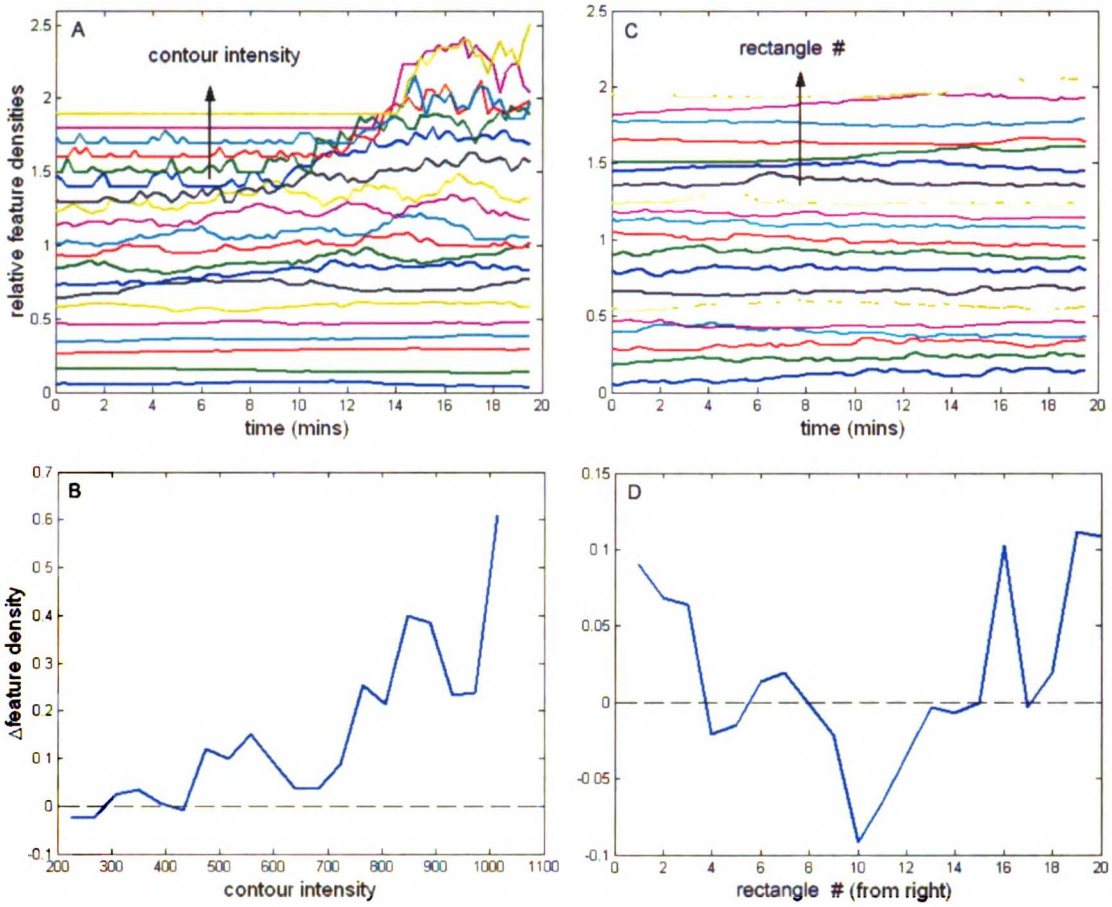

Figure 4.3: The cell feature densities measured from an experiment in opposing gradients generated from 1 μM of fMLP (on the left in Figure 4.2) and 10 mM ChaCha (on the right). A) The density over time for each contour. The highest fluorescence intensity contour corresponds to the top line. The ordinate does not give the absolute density but is designed to provide clarity in comparing density changes between regions. B) The difference in density between the last and first frames for each contour. C) The density changes over time for regions defined by rectangles. The ordinate is the same as in (A). D) The difference in the density between last and first frames for each rectangle.

Figure 4.4 shows the first (A) and last (B) thresholded images from the same experiment described in Figure 4.3, with the rectangular regions superimposed. In (A), we see a cluster of cells in the central region. In (B) this cluster seems to have divided, with some cells migrating toward the source of fMLP and some migrating toward the source of ChaCha.

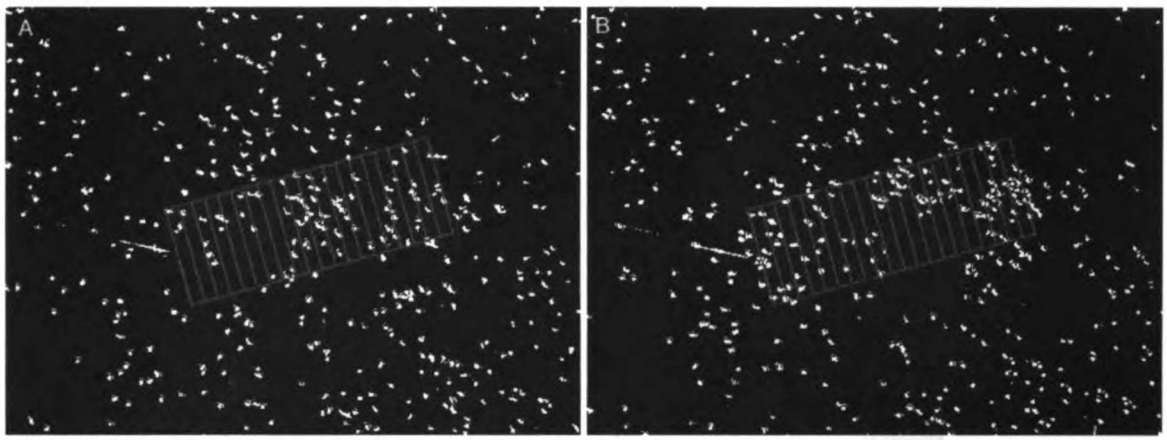

Figure 4.4: A) Rectangular regions superimposed over the first thresholded image from an experiment using 1 μM of fMLP (on the left) and 10 mM ChaCha (on the right). B) The final thresholded image from the same sequence.

Figure 4.5 shows the results from two experiments using different concentrations of fMLP and ChaCha, with the micropipettes separated by different distances. In (A), 1 mM of ChaCha is on the left and 100 μM of fMLP is on the right. The micropipettes are separated by about 295 μm and the elapsed time is 30 minutes. The general trend that we observe here and in a qualitative examination of the time-lapse sequence is that the cells appear to prioritize fMLP. Notice that the density in the region closest to the source of ChaCha decreases. As determined in Chapter 3, neutrophils do not migrate well to 1 mM ChaCha. The response observed here may be attributable to a weak signal rather than prioritization. This observation indicates another variable that we explore in the next section with the models. Figure 4.5B is the result from an experiment using optimal concentrations of fMLP and ChaCha as determined in Chapter 3. We placed 10 mM ChaCha on the left and 100 nM fMLP on the right, separated by a distance of 188 μm. The elapsed time is 22 minutes. We very clearly see an indication of prioritization in this figure. The density in the region near the source of ChaCha decreases, while the density near the fMLP increases. We turn now to an exploration of this behavior via modeling.

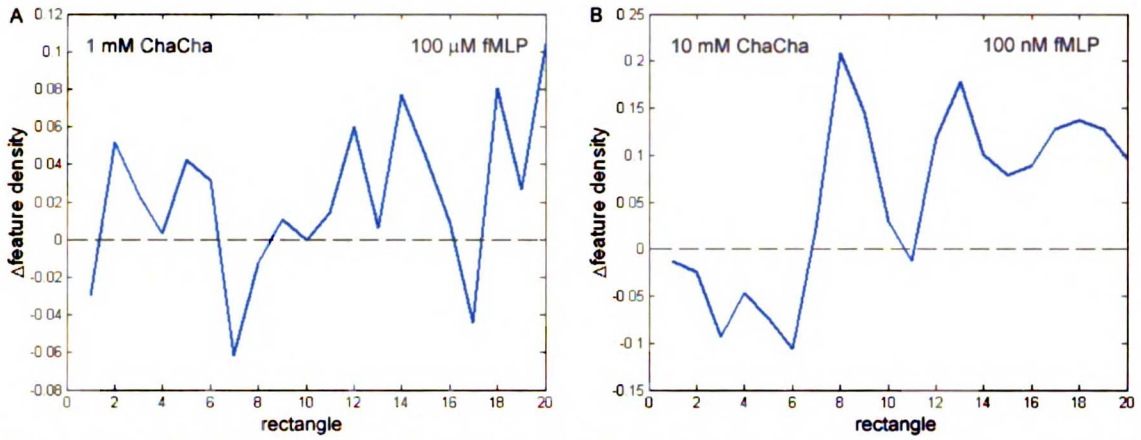

Figure 4.5: A) The difference in the density between the last and first frame for each rectangular region from an experiment using 1 mM ChaCha (on the left) and 100 μM of fMLP (on the right). B) The difference in density from an experiment using 10 mM ChaCha (on the left) and 100 nM fMLP (on the right).

4.4 Models and Simulation

Although we have not yet deduced a mechanism for gradient detection, as discussed in Chapter 3, we have developed several models based on the physics of receptor-ligand binding that enable a cursory exploration of the effects of binding parameters on migration direction. We extend these models here to account for multiple chemoattractant gradients.

4.4.1 Chemotactic bias

We will focus here on the chemotactic bias using the exponential model for the chemoattractant concentration profile in Eq. (3.4.17) and the steady state model for receptor-ligand binding in Eq. (3.4.10) (code can be found in appendix A.3). We include two forms of each equation, one for each chemoattractant. We will only consider one dimension. We assume that the direction of migration is given by the difference in the total number of bound receptors across the cell, ΔC_{tot} (#/cell). Each set of receptors will be exposed to different concentrations of their specific attractant, will have different

binding affinities, and will contain different quantities, so we need to account for them separately. Given these constraints, the direction of migration is given by

$$\Delta C_{tot} = d_{cell}\left(\nabla C_1 + \nabla C_2\right) \qquad (4.4.1)$$

where the individual bound receptor gradients are given by a form similar to Eq. (3.4.11), but modified to account for the exponential chemoattractant concentration profile. After expanding these we get

$$\Delta C_{tot} = -2\alpha d_{cell}\left(\frac{R_{tot1}K_{D1}L_1\left(x-x_{s1}\right)}{\left(K_{D1}+L_1\right)^2} + \frac{R_{tot2}K_{D2}L_2\left(x-x_{s2}\right)}{\left(K_{D2}+L_2\right)^2}\right) \qquad (4.4.2)$$

where most of the parameters are as defined above, and we have assumed that the diffusivity factor α, is equivalent between the two chemoattractants. In the models in Chapter 3, we assumed that the single source was located at the origin. We introduce two new variables here, x_{s1} and x_{s2}, to indicate the positions of the two sources. These parameters are implicitly included in the chemoattractant concentrations in Eq. (4.4.2).

The first variable we consider is the spatial separation of the chemoattractant sources. Figures 4.6A and C show the exponential concentration profiles along the x-axis for two different chemoattractants. In (A), the sources are located at -100 and 100, while in (C) they are located at -40 and 40. Figures 4.6B and D show the resulting differences in the total number of bound receptors across the cell. As in Chapter 3, we assume that

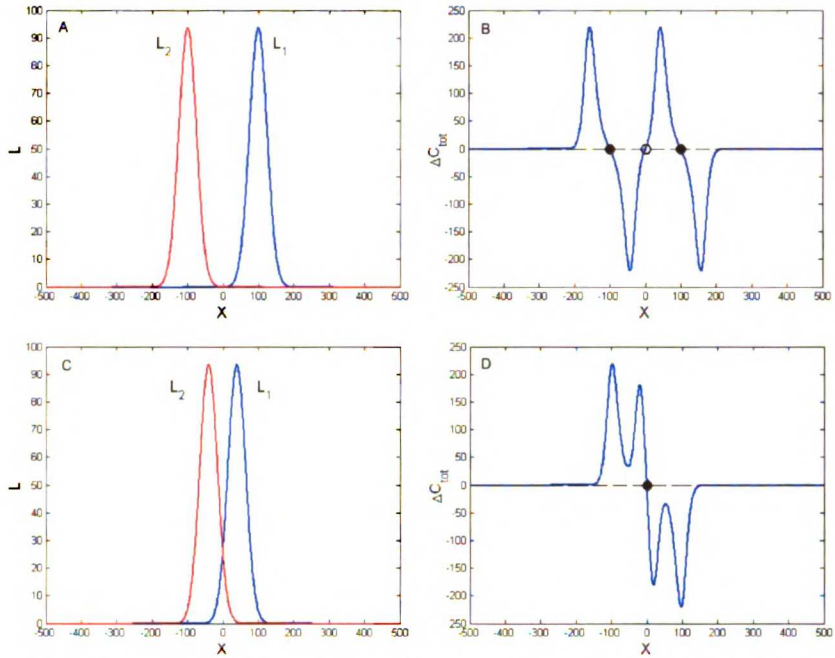

Figure 4.6: A) The exponential concentration profiles of two different chemoattractants with sources located at -100 and 100. B) The difference in the total number of bound receptors across a cell located at positions along the x-axis resulting from the profiles in (A). The black dots are stable fixed points where the cell will come to rest according to the migration model. The open black dot is an unstable fixed point. C) The exponential concentration profiles for sources located at -40 and 40. D) The resulting difference in the total number of bound receptors. Parameter values can be found in Table 3.1.

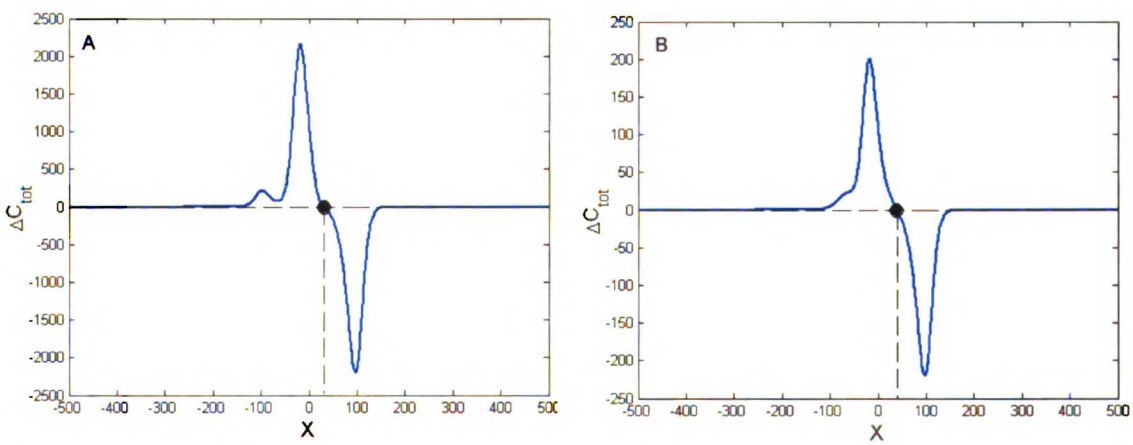

Figure 4.7: A) The difference in the total number of bound receptors across a cell exposed to the ligand profiles in Figure 4.6C when there are 10 times as many receptors for ligand 1. B) The difference across a cell when the dissociation constant for ligand 2 is 100 times greater.

the direction of migration is indicated by the sign on this difference; if it is positive, cells will migrate in the positive x direction; if it is negative, cells will migrate in the negative x direction. The parameter values are those presented in Table 3.1. The black circles in these figures indicate fixed points. The solid circles are stable fixed points to which cells will be attracted. The open circle is an unstable fixed point. Cells on either side of this point will move away from it. In (B), the sources are far enough apart that there is essentially no interaction and the cells will migrate to the closest source. This agrees with the results in Figure 4.3D. If the sources are closer then there will be interaction, as in (D). The cells here will move to a position halfway between the sources. This is where the attraction to each source is equally balanced. The optimum position for detecting the gradient is based on the dissociation constant, as discussed in [Zigmond, 1977]. On either side of the central point in (D), the balance between the attractions to each source, based on the optimum position, shifts to drive the cells back to the center.

Figure 4.7 demonstrates how a cell may prioritize certain chemoattractants based on binding parameters. In (A), there are 10 times as many receptors for the chemoattractant on the right. Every other parameter is exactly as in Figure 4.6D. Notice that the stable fixed point moves to the right, indicating a prioritization of the signal on the right. In (B), the dissociation constant for the ligand on the left is 10 times higher. Since the dissociation constant approximates the concentration at which the cells will optimally detect the gradients and the maximum concentration for the ligand on the left is 100 nM, this chemoattractant is essentially ignored. The fixed point is located almost exactly at the source of the ligand on the right. Based on our observations discussed above and in Chapter 3, we determined that the optimal source concentrations for fMLP

and ChaCha are 100 nM and greater that 10 mM, respectively. Clearly the dissociation constant for ChaCha is much higher or there is a similar effect caused somewhere downstream in the signaling pathway. Given higher concentrations of ChaCha, we could easily test the predictions of this model. If the concentrations are optimal for both chemoattractants and the sources are close enough, we should not observe prioritization.

4.4.2 Chemotaxis in multiple chemoattractant gradients using the OU process

To simulate cell migration in multiple chemoattractant gradients using the OU process, we use the method outlined in Section 3.4.3, with additional states to account for each chemoattractant (see appendix A.4). Since we wish to limit the exploration to the effects caused by differences in the binding parameters, we assume that there is a single chemotactic responsiveness term that is multiplied by the vector sum of bound receptor gradients to give the chemotactic bias. In future work, this chemotactic responsiveness can be parsed among the two chemoattractants. The relative difference in the chemotactic responsiveness for each gradient may then provide a certain measure of prioritization.

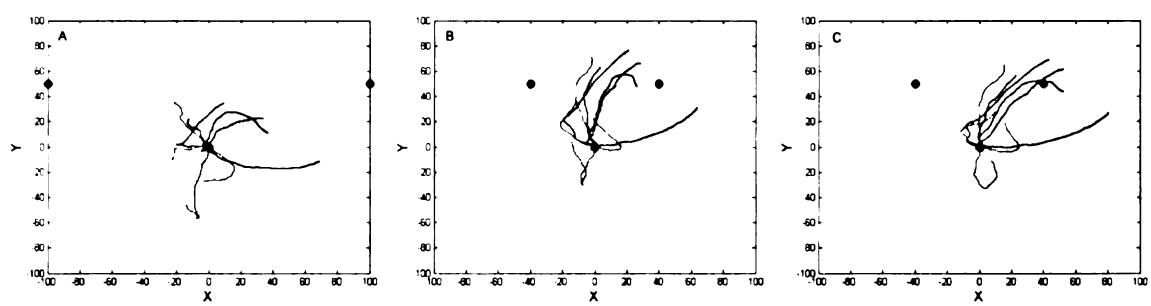

Figure 4.8: Simulated migration paths of cells exposed to two different chemoattractants. The chemoattractant sources are indicate by the red dots. The starting position of the cells is indicated by the green dot. Parameter values are those used in Chapter 3. A) The sources are far away from the cell starting point. B) The cells migrate toward the center of the sources similar to that depicted in Figure 4.6D. C) With 10 times the number of receptors for the source on the right, the vector sum is biased in this direction. The results are similar if the dissociation constant for the ligand on the left is increase 10 times (not shown).

Figure 4.8 shows the results of simulations performed using the same parameters as before, with Eq. (4.4.2) substituted into the chemotactic bias term. In (A), the sources, indicated by red dots, are too far apart to have any noticeable effect on the migration paths. Cells, starting at the green dot, migrate randomly exactly as in Figure 3.22A since the same seed for the random number generator was used. In (B), the sources are closer together and the cells bias their migration toward the stable fixed point residing between the sources, as predicted in Figure 4.6D. Noise in the migration paths prevents the cells from reaching the exact center and several cells migrate farther away, potentially out of range of any useful interaction between the chemoattractants. In (C), there are 10 times as many receptors for the ligand on the right, just as in Figure 4.7A. The cells bias their migration toward this source and signal prioritization occurs. The results are similar if the dissociation constant for the ligand on the left is 10 times higher.

4.5 Conclusions

In this chapter, we presented our final extension of the modeling framework based on the OU process to account for neutrophil chemotaxis in multiple chemoattractant gradients. We demonstrated the use of the micropipette assay to these studies, and we adapted the novel image processing techniques for tracking cell density developed in Chapter 3 toward quantifying the experimental results. Using these techniques, we presented the results of three experiments designed to highlight specific behaviors that were amenable to further exploration via a mathematical model. We developed a model of the chemotactic bias based on the physics of receptor-ligand binding and examined the

model predictions in light of the experimental results. We incorporated this model into the OU process and simulated cell migration paths.

Key conclusions include: 1. the spatial separation of two chemoattractant sources relative to their dissociation constants plays an important role in determining the degree of interaction between two signals by setting the positions at which cells are optimally attracted to each source. 2. The relative values for the receptor-ligand binding parameters between two chemoattractants can have a significant impact in the chemotactic bias, even effecting signal prioritization. Studies designed to measure the neutrophil chemotactic response in multiple chemoattractant gradients need to account for this phenomenon. 3. The micropipette assay is superior to the under-agarose assay for performing these types of studies. It enables dynamic positioning of chemoattractant gradients, allows for real-time monitoring of the gradient, and is fairly reproducible and easy to use. This technique is especially suited for performing experiments designed to study heterologous desensitization. Neutrophils would first be made to migrate up a gradient of fMLP. The micropipette would then be switched to ChaCha or another chemoattractant and the response would be measured.

The main obstacles in further developing this framework for studies in multiple gradients include the disagreement between the model predictions and experimental results with single chemoattractants, and the placement and estimation of the chemotactic responsiveness in relation to the separate terms for each chemoattractant. The results presented here offer a solid foundation on which to explore these issues and pursue a more detailed understanding of the engineering principles behind multiple signal processing in neutrophil chemotaxis.

Chapter 5

Conclusions and Recommendations

As discussed in Chapter 1, the application of mathematical models towards describing neutrophil chemotaxis has largely paralleled experimental advances in the field. Earlier phenomenological models focused on understanding the migratory behavior of cells or populations of cells, while more recent models have delved into the biochemical mechanisms behind signal amplification and polarization. Except for a few noted exceptions, these two levels of models have largely remained disconnected. We have expanded on one of the exceptions here to develop a modeling framework to relate experimentally observable cell migration paths to the physical principles involved in receptor-ligand binding. This framework is based on a modification of the OU process to describe persistent random walks biased by chemoattractant gradients.

In Chapter 2, we presented and applied methods for determining the migration speeds and persistence times of neutrophils crawling in uniform chemoattractant concentrations. We demonstrated the use of these parameters in the OU process to simulate cell migration paths that are indistinguishable from experimentally observed paths. While we were unable to determine if the parameters play a role in chemotaxis, the methods can easily be applied to future experiments designed to study these effects.

In Chapter 3, we expanded the OU process by including a term describing the chemotactic bias toward a chemoattractant gradient. We performed experiments using the micropipette assay and developed novel image processing techniques to extract useful

information describing the resulting responses. We used this information to examine a number of models of chemotactic bias based on the physics of receptor-ligand binding. Using the speeds and persistence times from Chapter 2, we simulated the OU process with chemotactic bias and suggested methods for comparing results. While we were unable to achieve agreement between the experimental results and model predictions, we highlighted key aspects that show potential for further development. These include an examination of the dependence of the speeds and persistence times on the chemoattractant concentration and a more detailed derivation of the model for the ligand concentration profile.

Finally, in Chapter 4, we modified the OU process to account for chemotaxis in multiple chemoattractant gradients. We assumed that neutrophils respond to the vector-sum of the gradients of bound receptors that form as a result of the individual chemoattractant gradients, and we showed how differences in receptor-ligand binding parameters between the two chemoattractants can affect the direction of migration. The results indicate that a cell can prioritize chemoattractants by increasing the number of receptors or decreasing the binding affinity relative to competing chemoattractants. After adapting the micropipette assay and image processing techniques, we were able to produce a qualitative agreement between experimental results and model predictions. An important product of this work is the novel application of the micropipette assay for studying chemotaxis in multiple chemoattractant gradients. This presents a number of opportunities for future experiments that are impossible using previous assays. In particular, the responses to temporal changes in chemoattractant gradients can be studied.

The primary motivation behind the work presented here has been to understand how neutrophils are engineered to process and respond to multiple chemoattractant gradients. As presented in Chapter 1, there have been a number of studies on neutrophil chemotaxis dating back more than 30 that have advanced our knowledge of how the signaling pathways enable neutrophils to amplify shallow chemoattractant gradients and organize their motile machinery to move in the appropriate direction. The vast majority of this work has focused on the response to single chemoattractants. In vivo, neutrophils are confronted with complex arrays of multiple chemoattractants and other signals that direct them to their targets. By focusing on the mechanisms behind multiple-signal processing, we highlight not only conditions more relevant to their natural environment, but also the organizing principles of signaling pathways that are responsible for simultaneously affecting multiple cellular functions. Key questions that arise include: Where in the pathways do the signals converge? How are the signals prioritized and processed to produce the appropriate responses? What happens when this processing machinery goes awry? While we have not answered these questions here, we have developed a modeling framework to study neutrophil chemotaxis in multiple chemoattractant gradients and pursue these questions more deeply.

Nomenclature

Symbol	Definition	Typical Units
$\vec{v}$	two-dimensional velocity vector	μm/min
$\vec{W}$	two-dimensional Weiner process	$min^{-1/2}$
S	speed	μm/min
P	persistence time	min
$\vec{x}$	two-dimensional position vector	
$\langle D^2 \rangle$	mean-square cell displacement	μm^2
T	interval time	min
x	position x axis	
y	position on y axis	
t	Time	min
δ	cell displacement	μm
τ	time interval	min
ϕ	angle between displacements at different times	
μ	random motility coefficient	μm^2/min
Δt	time step	min
$N(0,1)$	normally distributed random number	
$V_{x,i}$	velocity in x direction at time step i	μm/min
X_i	x position at time step i	
$d\vec{W}$	differential Weiner process vector	$min^{-1/2}$
$d\vec{v}$	differential change in velocity vector	μm/min
d_{cell}	diameter of cell	μm
∇C	gradient of bound receptors	#/cell/ μm
κ	chemotactic responsiveness	μm/min/#/cell
L	chemoattractant concentration	nM
L_0	source chemoattractant concentration	nM
r	radial distance from chemoattractant source	μm
a_0	radius of chemoattractant source	μm
q	flow rate of chemoattractant from micropipette	μmole/s
D	chemoattractant diffusivity	μm^2/s
z	distance between plane and point source	μm
I	fluorescence intensity	
I_0	maximum fluorescence intensity	
R	free receptors	#/cell
C	bound receptors	#/cell
k_b	receptor-ligand binding rate constant	$nM^{-1}s^{-1}$
k_u	unbinding rate constant	s^{-1}
R_{tot}	total number of receptors	#/cell

K_D	dissociation constant	nM
ΔC	difference in bound receptors across cell	#/cell
R_0	free receptors after desensitization	#/cell
n	Hill coefficient	
C_d	bound receptors after desensitization	#/cell
α_L	chemoattractant diffusivity factor	μm^{-2}
ΔC_{tot}	total difference in bound receptors across cell	#/cell
∇C_1	gradient in bound receptors for ligand 1	#/cell/ μm
∇C_2	gradient in bound receptors for ligand 2	#/cell/ μm
x_{s1}	x position of source of ligand 1	
x_{s2}	x position of source of ligand 2	

Bibliography

Adams, J. A., G. M. Omann, et al. (1998). "A mathematical model for ligand/receptor/G -protein dynamics and actin polymerization in human neutrophils." J Theor Biol 193(4): 543-60.

Alberts, B., A. Johnson, et al. (2002). Molecular Biology of the Cell. New York, Garland Science.

Alt, W. (1980). "Biased random walk models for chemotaxis and related diffusion approximations." J Math Biol 9(2): 147-77.

Berg, H. C. and E. M. Purcell (1977). "Physics of chemoreception." Biophys J 20(2): 193-219.

Berg, H. C. (1993). Random Walks in Biology. Princeton, NJ, Princeton University Press.

Bourne, H. R. and E. C. Meng (2000). "Structure. Rhodopsin sees the light." Science 289(5480): 733-4.

Boyden, S. (1962). "The chemotactic effect of mixtures of antibody and antigen on polymorphonuclear leucocytes." J Exp Med 115: 453-66.

Campbell, J. J., E. F. Foxman, et al. (1997). "Chemoattractant receptor cross talk as a regulatory mechanism in leukocyte adhesion and migration." Eur J Immunol 27(10): 2571-8.

Collins, S. J., R. C. Gallo, et al. (1977). "Continuous growth and differentiation of human myeloid leukaemic cells in suspension culture." Nature 270(5635): 347-9.

Crank, J. (1975). Mathematics of Diffusion. Oxford, Oxford University Press.

Devreotes, P. N. and S. H. Zigmond (1988). "Chemotaxis in eukaryotic cells: a focus on leukocytes and Dictyostelium." Annu Rev Cell Biol 4: 649-86.

Devreotes, P. and C. Janetopoulos (2003). "Eukaryotic chemotaxis: distinctions between directional sensing and polarization." J Biol Chem 278(23): 20445-8.

Doob, J. L. (1942). "The brownian movement and stochastic equations." Ann Math 43: 351-69.

Dunn, G. A. (1983). "Characterising a kinesis response: time averaged measures of cell speed and directional persistence." Agents Actions Suppl 12: 14-33.

Dunn, G. A. and A. F. Brown (1987). "A unified approach to analysing cell motility." J Cell Sci Suppl 8: 81-102.

Dusenbery, D. B. (1998). "Spatial sensing of stimulus gradients can be superior to temporal sensing for free-swimming bacteria." Biophys J 74(5): 2272-7.

Farrell, B. E., R. P. Daniele, et al. (1990). "Quantitative relationships between single-cell and cell-population model parameters for chemosensory migration responses of alveolar macrophages to C5a." Cell Motil Cytoskeleton 16(4): 279-93.

Foxman, E. F., J. J. Campbell, et al. (1997). "Multistep navigation and the combinatorial control of leukocyte chemotaxis." J Cell Biol 139(5): 1349-60.

Foxman, E. F., E. J. Kunkel, et al. (1999). "Integrating conflicting chemotactic signals. The role of memory in leukocyte navigation." J Cell Biol 147(3): 577-88.

Funamoto, S., K. Milan, et al. (2001). "Role of phosphatidylinositol 3' kinase and a downstream pleckstrin homology domain-containing protein in controlling chemotaxis in dictyostelium." J Cell Biol 153(4): 795-810.

Funamoto, S., R. Meili, et al. (2002). "Spatial and temporal regulation of 3

-phosphoinositides by PI 3-kinase and PTEN mediates chemotaxis." Cell 109(5): 611-23.

Gillespie, D. T. (1996). "Exact numerical simulation of the Ornstein-Uhlenbeck process and its integral." Physical Review. E. Statistical Physics, Plasmas, Fluids, and Related Interdisciplinary Topics 54(2): 2084-2091.

Hauert, A. B., S. Martinelli, et al. (2002). "Differentiated HL-60 cells are a valid model system for the analysis of human neutrophil migration and chemotaxis." Int J Biochem Cell Biol 34(7): 838-54.

Heit, B., S. Tavener, et al. (2002). "An intracellular signaling hierarchy determines direction of migration in opposing chemotactic gradients." J Cell Biol 159(1): 91-102.

Iijima, M., Y. E. Huang, et al. (2002). "Temporal and spatial regulation of chemotaxis." Dev Cell 3(4): 469-78.

Iijima, M. and P. Devreotes (2002). "Tumor suppressor PTEN mediates sensing of chemoattractant gradients." Cell 109(5): 599-610.

Iijima, M., Y. E. Huang, et al. (2004). "Novel mechanism of PTEN regulation by its phosphatidylinositol 4,5-bisphosphate binding motif is critical for chemotaxis." J Biol Chem 279(16): 16606-13.

Ionides, E. L., K. S. Fang, et al. (2004). "Stochastic models for cell motion and taxis." J Math Biol 48(1): 23-37.

Janetopoulos, C., L. Ma, et al. (2004). "Chemoattractant-induced phosphatidylinositol 3,4,5-trisphosphate accumulation is spatially amplified and adapts, independent of the actin cytoskeleton." Proc Natl Acad Sci U S A 101(24): 8951-6.

Keller, E. F. and L. A. Segel (1971). "Model for chemotaxis." J Theor Biol 30(2): 225 -34.

Lauffenburger, D. A., R. T. Tranquillo, et al. (1988). "Concentration gradients of chemotactic factors in chemotaxis assays." Methods Enzymol 162: 85-101.

Lauffenburger, D. A. and J. J. Linderman (1993). Receptors: models for binding, trafficking, and signaling. New York, Oxford University Press.

Lefkowitz, R. J., J. Inglese, et al. (1992). "G-protein-coupled receptors: regulatory role of receptor kinases and arrestin proteins." Cold Spring Harb Symp Quant Biol 57: 127-33.

Lefkowitz, R. J. (2004). "Historical review: a brief history and personal retrospective of seven-transmembrane receptors." Trends Pharmacol Sci 25(8): 413-22.

Lemons, D. S. (2002). An Introduction to Stochastic Processes in Physics. Baltimore, The Johns Hopkins University Press.

Levchenko, A. and P. A. Iglesias (2002). "Models of eukaryotic gradient sensing: application to chemotaxis of amoebae and neutrophils." Biophys J 82(1 Pt 1): 50-63.

Li, Z., X. Dong, et al. (2005). "Regulation of PTEN by Rho small GTPases." Nat Cell Biol 7(4): 399-404.

Li Jeon, N., H. Baskaran, et al. (2002). "Neutrophil chemotaxis in linear and complex gradients of interleukin-8 formed in a microfabricated device." Nat Biotechnol 20(8): 826-30.

McCutcheon, M. (1946). "Chemotaxis in leucocytes." Physiol Rev 26: 319-336.

Meili, R., C. Ellsworth, et al. (1999). "Chemoattractant-mediated transient activation and

membrane localization of Akt/PKB is required for efficient chemotaxis to cAMP in Dictyostelium." Embo J 18(8): 2092-105.

Meinhardt, H. (1999). "Orientation of chemotactic cells and growth cones: models and mechanisms." Journal of Cell Science 112((Pt 17)): 2867-74.

Moghe, P. V. and R. T. Tranquillo (1994). "Stochastic model of chemoattractant receptor dynamics in leukocyte chemosensory movement." Bull Math Biol 56(6): 1041-93.

Narang, A., K. K. Subramanian, et al. (2001). "A mathematical model for chemoattractant gradient sensing based on receptor-regulated membrane phospholipid signaling dynamics." Ann Biomed Eng 29(8): 677-91.

Nelson, R. D., P. G. Quie, et al. (1975). "Chemotaxis under agarose: a new and simple method for measuring chemotaxis and spontaneous migration of human polymorphonuclear leukocytes and monocytes." J Immunol 115(6): 1650-6.

Othmer, H. G., S. R. Dunbar, et al. (1988). "Models of dispersal in biological systems." J Math Biol 26(3): 263-98.

Parent, C. A., B. J. Blacklock, et al. (1998). "G protein signaling events are activated at the leading edge of chemotactic cells." Cell 95(1): 81-91.

Parent, C. A. and P. N. Devreotes (1999). "A cell's sense of direction." Science 284(5415): 765-70.

Postma, M. and P. J. Van Haastert (2001). "A diffusion-translocation model for gradient sensing by chemotactic cells." Biophys J 81(3): 1314-23.

Postma, M., J. Roelofs, et al. (2003). "Uniform cAMP stimulation of Dictyostelium cells induces localized patches of signal transduction and pseudopodia." Mol Biol Cell 14(12): 5019-27.

Rappel, W. J., P. J. Thomas, et al. (2002). "Establishing direction during chemotaxis in eukaryotic cells." Biophys J 83(3): 1361-7.

Riccobene, T. A., G. M. Omann, et al. (1999). "Modeling activation and desensitization of G-protein coupled receptors provides insight into ligand efficacy." J Theor Biol 200(2): 207-22.

Richardson, R. M., H. Ali, et al. (1995). "Cross-desensitization of chemoattractant receptors occurs at multiple levels. Evidence for a role for inhibition of phospholipase C activity." J Biol Chem 270(46): 27829-33.

Rickert, P., O. D. Weiner, et al. (2000). "Leukocytes navigate by compass: roles of PI3Kgamma and its lipid products." Trends Cell Biol 10(11): 466-73.

Ridley, A. J., M. A. Schwartz, et al. (2003). "Cell migration: integrating signals from front to back." Science 302(5651): 1704-9.

Rivero, M. A., R. T. Tranquillo, et al. (1989). "Transport models for chemotactic cell populations based on individual cell behavior." Chem Eng Sci 44(12): 2881-2897.

Servant, G., O. D. Weiner, et al. (1999). "Dynamics of a chemoattractant receptor in living neutrophils during chemotaxis." Mol Biol Cell 10(4): 1163-78.

Servant, G., O. D. Weiner, et al. (2000). "Polarization of chemoattractant receptor signaling during neutrophil chemotaxis." Science 287(5455): 1037-40.

Srinivasan, S., F. Wang, et al. (2003). "Rac and Cdc42 play distinct roles in regulating PI(3,4,5)P3 and polarity during neutrophil chemotaxis." J Cell Biol 160(3): 375-85.

Stokes, C. L., D. A. Lauffenburger, et al. (1991). "Migration of individual microvessel endothelial cells: stochastic model and parameter measurement." J Cell Sci 99 (Pt 2): 419-30.

Thar, R. and M. Kuhl (2003). "Bacteria are not too small for spatial sensing of chemical gradients: an experimental evidence." Proc Natl Acad Sci U S A **100**(10): 5748-53.

Tranquillo, R. T., D. A. Lauffenburger, et al. (1988). "A stochastic model for leukocyte random motility and chemotaxis based on receptor binding fluctuations." J Cell Biol 106(2): 303-9.

Tranquillo, R. T. and W. Alt (1990). Glossary of terms concerning oriented movement. Biological Motion. W. Alt and G. Hoffman. Berlin, Springer-Verlag.

Trzeciakowski, J. P. (1996). "Analysis of stimulus-response chains using nonlinear dynamics." J Pharmacol Toxicol Methods 36(2): 103-21.

Wang, F., P. Herzmark, et al. (2002). "Lipid products of PI(3)Ks maintain persistent cell polarity and directed motility in neutrophils." Nat Cell Biol 4(7): 513-8.

Weiner, O. D., G. Servant, et al. (1999). "Spatial control of actin polymerization during neutrophil chemotaxis." Nat Cell Biol 1(2): 75-81.

Weiner, O. D., P. O. Neilsen, et al. (2002). "A PtdInsP(3)- and Rho GTPase-mediated positive feedback loop regulates neutrophil polarity." Nat Cell Biol 4(7): 509-13.

Xiao, Z., N. Zhang, et al. (1997). "Dynamic distribution of chemoattractant receptors in living cells during chemotaxis and persistent stimulation." J Cell Biol 139(2): 365-74.

Xu, J., F. Wang, et al. (2003). "Divergent signals and cytoskeletal assemblies regulate

self-organizing polarity in neutrophils." Cell 114(2): 201-14.

Zigmond, S. H. (1977). "Ability of polymorphonuclear leukocytes to orient in gradients of chemotactic factors." J Cell Biol 75(2 Pt 1): 606-16.

Zigmond, S. H. and S. J. Sullivan (1979). "Sensory adaptation of leukocytes to chemotactic peptides." J Cell Biol 82(2): 517-27.

Zigmond, S. H. (1981). "Consequences of chemotactic peptide receptor modulation for leukocyte orientation." J Cell Biol 88(3): 644-7.

Zigmond, S. H., H. I. Levitsky, et al. (1981). "Cell polarity: an examination of its behavioral expression and its consequences for polymorphonuclear leukocyte chemotaxis." J Cell Biol 89(3): 585-92.

Zigmond, S. H., J. L. Slonczewski, et al. (1988). "Polymorphonuclear leukocyte locomot locomotion is insensitive to lowered cytoplasmic calcium levels." Cell Motil Cytoskeleton 9(2): 184-9.

Appendices

Matlab Code

A.1 Image processing

Downsample images from uniform concentration experiments

```
%function out = SampleLargeTiffs()
%UNTITLED1 Summary of this function goes here
%  Detailed explanation goes here
cd c:\Data\Keith\Keith051112\control2

time=[11*3600+39*60+36:((13*3600+3*60+42)-(11*3600+39*60+36))/502:13*3600+3*60+42];

Is=zeros(384,512);
for i=1:503
   num=floor(10000*floor(time(i)/3600)+100*floor(mod(time(i),3600)/60)+mod(mod(time(i),3600),60));
   while (~exist(['Keith051112-',num2str(num,'%06d'),'.tif']))
      num=num+1;
   end

%num=floor(10000*floor(time(i)/3600)+100*floor(mod(time(i),3600)/60)+mod(mod(time(i),3600),60));
   I=imread(['Keith051112-',num2str(num,'%06d')],'tif');
   %else
   %   time(i)=time(i)+1;
   %
num=floor(10000*floor(time(i)/3600)+100*floor(mod(time(i),3600)/60)+mod(mod(time(i),3600),60));
   %   I=imread(['Keith051112-',num2str(num,'%06d')],'tif');
   %end

   for j=0:383
      for k=0:511
         Is(j+1,k+1)=sum(sum(I(4*j+1:4*j+4,4*k+1:4*k+4)))/16;
      end
   end

   Is=uint16(Is);

   savefile=['UControl2_',num2str(i,'%03d'),'.tif'];
   cd c:\Data\Keith\Keith051112\control2\Sampled
   imwrite(Is,savefile,'tif','Compression','none');
   cd c:\Data\Keith\Keith051112\control2
end
```

Cell tracking

```
%function [ output_args ] = TrackCells( input_args )
%TRACKCELLS Get x,y coordinates of cell paths
%  Set directory, numframes, and sample rate (f).
%  Code reads in each frame (check for cells migrating on or off over the
```

```
% course of the stack and start from end or begining accordingly), adjusts
% contrast, and waits for user input consisting of right mouse click on center
% of cell to be tracked. One cell is tracked at a time.
% For first track, uncomment store=[] line and comment out load store.mat
% For subsequent tracks, reverse this.
clear all

cd c:\Docu'ments and Settings\'kaerickson\My' Documents\'Research\Images\103105\100uM

numframes=505;
filename='U100uMpaths.mat';
%for initial cell tracked in sequence, comment out load store.mat
%and uncomment store=[]. For subsequent cells, reverse this
store=[];
%load U100uMpaths.mat;

storex=zeros(numframes,1);
storey=zeros(numframes,1);

for i=2:1:numframes%:-1:1
   I=imread(['U100uM',num2str(i,'%03d')],'tif');
   h=figure(2);imshow(I,[]);
   truesize(h,[2*size(I)]);
   hold
   plot(storex(1:i-1),storey(1:i-1))
   title(num2str(i))
   [x y p]=impixel
   hold

   storex(i)=x;
   storey(i)=y;

end

store=[store storex storey];

I=imread(['U100uM',num2str(numframes,'%03d')],'tif');
figure(3),imshow(I,[])
hold
plot(store(end,[1:2:end]),store(end,[2:2:end]),'gx','MarkerSize',12, 'LineWidth', 3);
hold

Is=imread('U100uM002','tif');
figure(4),clf,figure(4),imshow(Is,[]),hold
plot(store(2,1:2:end),store(2,2:2:end),'gx','MarkerSize',12,'LineWidth',3)
hold

save(filename, 'store');
```

Smooth experimental cell tracks

```
function out = Smooth1nMUniform()
%SMOOTH1NMUNIFORM Summary of this function goes here
% Detailed explanation goes her
```

```
%0.35 um/pixel independent of binning since binning doesn't appear to work
%in labview, the labview images are then sampled so that 1 pixel on image
%used to track cells equals 4 pixels on raw image

cd c:\Docu'ments and Settings\'kaerickson\My' Documents\'Research\Images\C'ell Paths\'Uniform

load U1nMpathsraw.mat
U=store(1:361,:);
U=U(2:end,:)-repmat(U(2,:),size(U,1)-1,1);
t=[0:10:360*10-10]';

%smoothing
window=25;
half=floor(window/2);
for cell=1:10
  for frame=1:360
    if frame<=half                % Polynomial fit of X and Y position over time
      polyx=polyfit(t(1:window), U(1:window,2*cell-1), 2);
      Us(frame,2*cell-1)=polyval(polyx, t(frame));
      polyy=polyfit(t(1:window), U(1:window,2*cell), 2);
      Us(frame,2*cell)=polyval(polyy,t(frame));
    elseif frame<=(360-half)
      polyx=polyfit(t(frame-half:frame+half), U(frame-half:frame+half,2*cell-1), 2);
      Us(frame,2*cell-1)=polyval(polyx, t(frame));
      polyy=polyfit(t(frame-half:frame+half), U(frame-half:frame+half,2*cell), 2);
      Us(frame,2*cell)=polyval(polyy,t(frame));
    else
      polyx=polyfit(t(360-window:360), U(360-window:360,2*cell-1), 2);
      Us(frame,2*cell-1)=polyval(polyx, t(frame));
      polyy=polyfit(t(360-window:360), U(360-window:360,2*cell), 2);
      Us(frame,2*cell)=polyval(polyy,t(frame));
    end
  end
end

Us=Us*4*0.35;  %account for calibration of pixel size in ccd


%figures
figure,plot(U(:,1:2:end),U(:,2:2:end),0,0,'ko','MarkerSize',15,'LineWidth',2)
xlabel('X','FontSize',14),ylabel('Y','FontSize',14)
figure,plot(t/60,U(:,1:2:end),'LineWidth',2)
xlabel('time (mins)','FontSize',14),ylabel('X','FontSize',14)
figure,plot(t/60,U(:,2:2:end),'LineWidth',2)
xlabel('time (mins)','FontSize',14),ylabel('Y','FontSize',14)
figure,plot(Us(:,1:2:end),Us(:,2:2:end),0,0,'ko','MarkerSize',15,'LineWidth',2)
axis([-150 150 -150 150])
xlabel('X','FontSize',14),ylabel('Y','FontSize',14)
figure,plot(t/60,Us(:,1:2:end),'LineWidth',2)
xlabel('time (mins)','FontSize',14),ylabel('X','FontSize',14)
figure,plot(t/60,Us(:,2:2:end),'LineWidth',2)
xlabel('time (mins)','FontSize',14),ylabel('Y','FontSize',14)

U1nMUniformsmooth=Us;

save U1nMUniformsmooth U1nMUniformsmooth;
```

```
out=Us;
```

Image processing for single chemoattractant gradients

```
%function [ output_args ] = densitycircles( input_args )
%DENSITYCIRCLES Summary of this function goes here
%  Detailed explanation goes here

cd c:\Docu'ments and Settings\'kaerickson\My' Documents\'Research\Images\101705
[Si, numframes] = tiffread('neut1mMfMLP87sil101705fitc2.stk');
[Sp, numframes] = tiffread('neut1mMfMLP87sil101705phase2.stk');

%numsq=10;
%varea=floor(size(S(1).data,1)/numsq);
%harea=floor(size(S(1).data,2)/numsq);


Iiavg=zeros(size(Si(1).data));
for i=5:271
   Ii=Si(i).data;
   Ii=double(Ii);
   Iiavg=Iiavg+Ii;
end
Iiavg=Iiavg/(271-5+1);

numregs=20;
maxIi=max(max(Iiavg));
minIi=min(min(Iiavg));
[maxxIi maxyIi]=find(Iiavg==maxIi);
fracIi=(maxIi-minIi)/numregs;
V=[minIi:fracIi:maxIi];

contmask=zeros([size(Sp(1).data),numregs]);
for j=1:size(Sp(1).data,1)
   for k=1:size(Sp(1).data,2)
      Ijk=Iiavg(j,k);
      fr=find(abs(V-Ijk)==min(abs(V-Ijk)));
      contmask(j,k,fr)=1;
   end
end

numcirc=20;
drcirc=maxyIi/numcirc;
circrads=[drcirc:drcirc:numcirc*drcirc];
theta=[0:pi/20:pi];
xcirc=circrads'*cos(theta);
xcirc=[xcirc fliplr(xcirc)]+maxyIi;
ycirc=circrads'*sin(theta);
ycirc=[ycirc -ycirc]+maxxIi;

circmask=zeros([size(Sp(1).data),numcirc]);
for i=1:numcirc
   for j=1:size(Sp(1).data,1)
      for k=1:size(Sp(1).data,2)
```

```
        bigcirc=circrads(i);
        if i==1;
          smallcirc=0;
        else
          smallcirc=circrads(i-1);
        end
        circmask(j,k,i)=(((k-maxyIi)^2+(j-maxxIi)^2)<bigcirc^2)&(((k-maxyIi)^2+(j-
maxxIi)^2)>smallcirc^2);
      end
    end
end

Ipdcont=zeros(numregs,271-5+1);
Ipdcirc=zeros(numcirc,271-5+1);

for i=5:271
    Ip=Sp(i).data;
    Ip=double(Ip);
    Ip=mat2gray(Ip);
    Ip=imadjust(Ip,stretchlim(Ip),[0 1]);
    background=imopen(Ip,strel('disk',5));
    Ipb=Ip-background;
    Ipt=Ipb>0.3;
    %imshow(Ipt)
    %flick(i-4)=getframe
    for j=1:numregs
      Ipdcont(j,i-4)=sum(sum(Ipt.*contmask(:,:,j)))/sum(sum(contmask(:,:,j)));
    end
    for j=1:numcirc
      Ipdcirc(j,i-4)=sum(sum(Ipt.*circmask(:,:,j)))/sum(sum(circmask(:,:,j)));
    end
    if (i==5)
      Ip1=Ip;
      Ipb1=Ipb;
      Ipt1=Ipt;
    elseif (i==271)
      Ipend=Ip;
      Ipbend=Ipb;
      Iptend=Ipt;
    end
end

Ipddiffcont=Ipdcont(:,end)-Ipdcont(:,1);
Ipddiffcirc=Ipdcirc(:,end)-Ipdcirc(:,1);

figure,imshow(Ipbend),hold on,contour(Iiavg,V,'w'),hold off
figure,imshow(Ipbend),hold on,plot(xcirc',ycirc','w'),hold off

figure,plot([1:271-5+1],Ipdcont)
figure,plot([1:271-5+1],Ipdcirc)

figure,plot(circrads,Ipddiffcirc);
figure,plot(V(1:size(Ipddiff,1))',Ipddiff)
```

Image processing for multiple chemoattractant gradients

```
%function [ output_args ] = densitycircles( input_args )
%DENSITYCIRCLES Summary of this function goes here
%  Detailed explanation goes here

cd c:\Docu'ments and Settings\'kaerickson\Desktop\Complete\MultipleGradient\MGMovies
[Si, numframes] = tiffread('neut10mMCha100nMfMLP102005fitc.stk');    %load fluorescent stack
[Sp, numframes] = tiffread('neut10mMCha100nMfMLP102005phase.stk');   %load phase stack

in1=72;   %first frame
in2=161;   %last frame

%calculate average intensity over frames of interest
Iiavg=zeros(size(Si(1).data));
for i=in1:in2
   Ii=Si(i).data;
   Ii=double(Ii);
   Iiavg=Iiavg+Ii;
end
Iiavg=Iiavg/(in2-in1+1);

%get positions of highest intensity to draw line between sources
%need to left mouse click on first and then right mouse click on second
figure,imshow(Iiavg,[])
[tipx tipy p]=impixel

numregs=20; %number of regions in which to track density

%get coordinates of line connecting sources (defines midpts on ends of roi)
roilx=min(tipx);
roirx=max(tipx);
roiuy=min(tipy);
roily=max(tipy);

L=sqrt((roirx-roilx)^2+(roily-roiuy)^2); %length of roi
thL=-acos((roirx-roilx)/L);  %angle of line connecting pts wrt horizontal

th1=(thL-pi/2);          %- accounts for flip of y-axis in images
w=40;                    %width of roi

%box defining roi
llcx=roilx+w*cos(th1);
llcy=roiuy-w*sin(th1);
ulcx=roilx-w*cos(th1);
ulcy=roiuy+w*sin(th1);

dx=roirx-roilx;
dy=roily-roiuy;

lrcx=llcx+dx;
lrcy=llcy+dy;
urcx=ulcx+dx;
urcy=ulcy+dy;
```

```
x1=linspace(llcx,lrcx);
x2=linspace(lrcx,urcx);
x3=linspace(urcx,ulcx);
x4=linspace(ulcx,llcx);

y1=linspace(llcy,lrcy);
y2=linspace(lrcy,urcy);
y3=linspace(urcy,ulcy);
y4=linspace(ulcy,llcy);

ms=(llcy-ulcy)/(llcx-ulcx);  %slope of lines dividing regions
ml=(urcy-ulcy)/(urcx-ulcx);

%make masks
sqmask=zeros(size(Iiavg,1),size(Iiavg,2),numregs);
for i=1:numregs
   for x=llcx:urcx
      for y=ulcy:lrcy
         ys=(y>(ms*(x-(ulcx+(i-1)*dx/numregs))+ulcy+(i-1)*dy/numregs))&(y<(ms*(x-
(ulcx+i*dx/numregs))+ulcy+i*dy/numregs));
         yl=(y>(ml*(x-ulcx)+ulcy))&(y<(ml*(x-llcx)+llcy));
         sqmask(y,x,i)=ys&yl;
      end
   end
end

%define contour regions
Iiavgs=Iiavg(ulcy:lrcy,llcx:urcx)
maxIi=max(max(Iiavgs));
minIi=min(min(Iiavgs));
maxxIi=tipx(1);
maxyIi=tipy(1);
fracIi=(maxIi-minIi)/numregs;
V=[minIi:fracIi:maxIi];

%make contour masks
contmask=zeros(size(Iiavg,1),size(Iiavg,2),numregs);
for j=ulcy:ulcy+size(Iiavgs,1)
   for k=llcx:llcx+size(Iiavgs,2)
      Ijk=Iiavg(j,k);
      fr=find(abs(V-Ijk)==min(abs(V-Ijk)));
      contmask(j,k,fr)=1;
   end
end

Ipdcont=zeros(numregs,in2-in1+1);
Ipdsq=zeros(numregs,in2-in1+1);

%process images and track density
for i=in1:in2
   Ip=Sp(i).data;
   Ip=double(Ip);
   Ip=mat2gray(Ip);
   Ip=imadjust(Ip,stretchlim(Ip),[0 1]);
   background=imopen(Ip,strel('disk',5));
   Ipb=Ip-background;
```

```
  Ipt=Ipb>0.3;
  %track density
  for j=1:numregs
    Ipdcont(j,i-in1+1)=sum(sum(Ipt.*contmask(:,:,j)))/sum(sum(contmask(:,:,j)));
    Ipdsq(j,i-in1+1)=sum(sum(Ipt.*sqmask(:,:,j)))/sum(sum(sqmask(:,:,j)));
  end
  if (i==in1)
    Ip1=Ip;
    Ipb1=Ipb;
    Ipt1=Ipt;
  elseif (i==in2)
    Ipend=Ip;
    Ipbend=Ipb;
    Iptend=Ipt;
  end
end

%difference in densities between first and last images
Ipddiffcont=Ipdcont(:,end)-Ipdcont(:,1);
Ipddiffsq=Ipdsq(:,end)-Ipdsq(:,1);

%plot final images with contours or circles
figure,imshow(Iiavg,[]),hold on,contour(Iiavg(ulcy:lrcy,llcx:urcx),V,'w'),hold off
figure,imshow(Iptend),hold on,plot(x1,y1,'r',x2,y2,'r',x3,y3,'r',x4,y4,'r')
for i=1:numregs
  xt=linspace(ulcx+i*dx/numregs,llcx+i*dx/numregs);
  yt=ms*(xt-(ulcx+i*dx/numregs))+ulcy+i*dy/numregs
  plot(xt,yt,'r')
end
hold off

%plot differences in densities versus square # (for squares) or intensity (for contours)
figure,plot([1:numregs],Ipddiffsq,'LineWidth',2),xlabel('square # (from
right)','FontSize',14),ylabel('\Deltafeature density','FontSize',14)
figure,plot(V(1:size(Ipddiffcont,1))',Ipddiffcont,'LineWidth',2),xlabel('contour
intensity','FontSize',14),ylabel('\Deltafeature density','FontSize',14)

%plot densities over time
figure,plot([0:15/60:(in2-in1)*15/60],Ipdsq+repmat([0:0.1:1.9]',1,size(Ipdsq,2)),'LineWidth',2);
xlabel('time (mins)','FontSize',14),ylabel('relative feature densities','FontSize',14)
figure,plot([0:15/60:(in2-in1)*15/60],Ipdcont+repmat([0:0.1:1.9]',1,size(Ipdcont,2)),'LineWidth',2);
xlabel('time (mins)','FontSize',14),ylabel('relative feature densities','FontSize',14)
```

A.2 Parameter Estimation

Estimation of speeds and persistence times

```
function out = FitEqns1nM()
%FITEQNS1NM Summary of this function goes here
%  Detailed explanation goes here
cd c:\Docu'ments and Settings\'kaerickson\My' Documents\'Research\Images\C'ell Paths\'Uniform

load U1nMUniformsmooth.mat
Us=U1nMUniformsmooth;
```

```
t=[0:10:360*10-10]';

%Calculate speeds and persistence times from data
seglenP=sqrt((Us(2:end,1:2:end)-Us(1:end-1,1:2:end)).^2+(Us(2:end,2:2:end)-Us(1:end-1,2:2:end)).^2);
phiP=acos((Us(2:end,1:2:end)-Us(1:end-1,1:2:end))./(seglenP+0.000000001));
phiP=-1*((Us(2:end,2:2:end)-Us(1:end-1,2:2:end))<0).*phiP+((Us(2:end,2:2:end)-Us(1:end-
1,2:2:end))>=0).*phiP;

phidiff=phiP(2:end,:)-phiP(1:end-1,:);

S=sqrt(mean(mean(seglenP.^2)))/10;
stdS=std(reshape(seglenP,size(seglenP,1)*size(seglenP,2),1))/10;

P=2*10/mean(mean(phidiff.^2));
stdP=2*10/std(reshape(phidiff,size(phidiff,1)*size(phidiff,2),1));

%variance in x and y positions
xs=Us(:,1:2:end);
meanxs=mean(xs')';
varxs=mean(xs.^2')'-meanxs.^2;
ys=Us(:,2:2:end);
meanys=mean(ys')';
varys=mean(ys.^2')'-meanys.^2;

%determine mean squared displacement
dT=[10:10:t(end)]';
meansqD=zeros(size(dT,1),1);
for i = 1:size(dT,1)
   meansqD(i)=mean(mean((Us(i+1:end,1:2:end)-Us(1:end-i,1:2:end)).^2+((Us(i+1:end,2:2:end)-Us(1:end-
i,2:2:end))).^2));
end

%mean squared displacement nonlinear parameter estimation
fun=inline('2*beta(1)^2*beta(2)^2*(x/beta(2)-1+exp(-x/beta(2)))','beta','x');
[fit,r,J]=nlinfit(dT(1:180),meansqD(1:180),fun,[0.1667 180]);
msdCI=nlparci(fit,r,J);
msdpred=2*fit(1)^2*fit(2)^2*(dT/fit(2)-1+exp(-dT/fit(2)));

%variance fit nonlinear parameter estimation
fun2=inline('beta2(1)^2*beta2(2)^2*(x/beta2(2)-2*(1-exp(-x/beta2(2)))+(1/2)*(1-exp(-
2*x/beta2(2))))','beta2','x');
[fit2x,r2x,J2x]=nlinfit(t,varxs,fun2,[0.1667 180]);
[fit2y,r2y,J2y]=nlinfit(t,varys,fun2,[0.1667 180]);
varxCI=nlparci(fit2x,r2x,J2x);
varyCI=nlparci(fit2y,r2y,J2y);
varxpred=fit2x(1)^2*fit2x(2)^2*(t/fit2x(2)-2*(1-exp(-t/fit2x(2)))+(1/2)*(1-exp(-2*t/fit2x(2))));
varypred=fit2y(1)^2*fit2y(2)^2*(t/fit2y(2)-2*(1-exp(-t/fit2y(2)))+(1/2)*(1-exp(-2*t/fit2y(2))));

%figures
figure,plot(dT/60,meansqD,'k-',dT/60,msdpred,'k--','LineWidth',2)
xlabel('Interval time (mins)','FontSize',14),ylabel('<D^2>','FontSize',14)
figure,plot(t/60,varxs,'k-',t/60,varxpred,'k--','LineWidth',2)
xlabel('time (mins)','FontSize',14),ylabel('var X','FontSize',14)
figure,plot(t/60,varys,'k-',t/60,varypred,'k--','LineWidth',2)
xlabel('time (mins)', 'FontSize',14),ylabel('var Y','FontSize',14)
```

```
%convert to um/min and min
fit(1)=fit(1)*60;
fit(2)=fit(2)/60;
msdCI(1,:)=msdCI(1,:)*60;
msdCI(2,:)=msdCI(2,:)/60;
msdstd(1)=fit(1)-msdCI(1,1);
msdstd(2)=fit(2)-msdCI(2,1);

fit2x(1)=fit2x(1)*60;
fit2x(2)=fit2x(2)/60;
varxCI(1,:)=varxCI(1,:)*60;
varxCI(2,:)=varxCI(2,:)/60;
varxstd(1)=fit2x(1)-varxCI(1,1);
varxstd(2)=fit2x(2)-varxCI(2,1);

fit2y(1)=fit2y(1)*60;
fit2y(2)=fit2y(2)/60;
varyCI(1,:)=varyCI(1,:)*60;
varyCI(2,:)=varyCI(2,:)/60;
varystd(1)=fit2y(1)-varyCI(1,1);
varystd(2)=fit2y(2)-varyCI(2,1);

out=[fit msdstd'; fit2x varxstd'; fit2y varystd'; S*60 stdS*60; P/60 stdP/60]
```

Correlation of experimental and simulated cell tracks in uniform concentrations

```
%function [ output_args ] = ExpSimStats( input_args )
%EXPSIMSTATS Summary of this function goes here
%  Detailed explanation goes here

load U100nMUniformsmooth.mat;
load U100nMUniformOU.mat;
load U100nMUniformOUhalf.mat

%parse x and y values to ease calculations
xse=U100nMUniformsmooth(:,1:2:end);
yse=U100nMUniformsmooth(:,2:2:end);

xss=U100nMUniformOU(:,1:2:end);
yss=U100nMUniformOU(:,2:2:end);

xssh=U100nMUniformOUhalf(:,1:2:end);
yssh=U100nMUniformOUhalf(:,2:2:end);

%correlation coefficients
rx12=zeros(size(xse,1),1);
ry12=zeros(size(yse,1),1);

rx13=zeros(size(xse,1),1);
ry13=zeros(size(yse,1),1);

rx23=zeros(size(xse,1),1);
ry23=zeros(size(yse,1),1);

%calculate the correlation coefficients
```

```
for i=1:size(xse,1)
   sortxe=sort(xse(i,:));
   sortxs=sort(xss(i,:));
   sortxsh=sort(xssh(i,:));

   sortye=sort(yse(i,:));
   sortys=sort(yss(i,:));
   sortysh=sort(yssh(i,:));

   numrx12=sum(sortxe.*sortxs)-(1/10)*sum(sortxe)*sum(sortxs);
   numry12=sum(sortye.*sortys)-(1/10)*sum(sortye)*sum(sortys);

   denrx12=sqrt(sum(sortxe.^2)-(1/10)*(sum(sortxe))^2)*sqrt(sum(sortxs.^2)-(1/10)*(sum(sortxs))^2);
   denry12=sqrt(sum(sortye.^2)-(1/10)*(sum(sortye))^2)*sqrt(sum(sortys.^2)-(1/10)*(sum(sortys))^2);

   rx12(i)=numrx12/denrx12;
   ry12(i)=numry12/denry12;

   numrx13=sum(sortxe.*sortxsh)-(1/10)*sum(sortxe)*sum(sortxsh);
   numry13=sum(sortye.*sortysh)-(1/10)*sum(sortye)*sum(sortysh);

   denrx13=sqrt(sum(sortxe.^2)-(1/10)*(sum(sortxe))^2)*sqrt(sum(sortxsh.^2)-(1/10)*(sum(sortxsh))^2);
   denry13=sqrt(sum(sortye.^2)-(1/10)*(sum(sortye))^2)*sqrt(sum(sortysh.^2)-(1/10)*(sum(sortysh))^2);

   rx13(i)=numrx13/denrx13;
   ry13(i)=numry13/denry13;

   numrx23=sum(sortxs.*sortxsh)-(1/10)*sum(sortxs)*sum(sortxsh);
   numry23=sum(sortys.*sortysh)-(1/10)*sum(sortys)*sum(sortysh);

   denrx23=sqrt(sum(sortxs.^2)-(1/10)*(sum(sortxs))^2)*sqrt(sum(sortxsh.^2)-(1/10)*(sum(sortxsh))^2);
   denry23=sqrt(sum(sortys.^2)-(1/10)*(sum(sortys))^2)*sqrt(sum(sortysh.^2)-(1/10)*(sum(sortysh))^2);

   rx23(i)=numrx23/denrx23;
   ry23(i)=numry23/denry23;

end

figure,plot([1:size(xse,1)],[rx12 ry12]),xlabel('time','FontSize',14),ylabel('Corr','FontSize',14)
figure,plot([1:size(xse,1)],[rx13 ry13]),xlabel('time','FontSize',14),ylabel('Corr','FontSize',14)
figure,plot([1:size(xse,1)],[rx23 ry23]),xlabel('time','FontSize',14),ylabel('Corr','FontSize',14)
figure,plot(0,0,'ko',xse,yse,'MarkerSize',10,'LineWidth',2),xlabel('X','FontSize',14),ylabel('Y','FontSize',14)
figure,plot(0,0,'ko',xss,yss,'MarkerSize',10,'LineWidth',2),xlabel('X','FontSize',14),ylabel('Y','FontSize',14)
figure,plot(0,0,'ko',xssh,yssh,'MarkerSize',10,'LineWidth',2),xlabel('X','FontSize',14),ylabel('Y','FontSize',1
4)
```

A.3 Models

Model of chemotactic bias in single gradient

```
%function out = ChemotaxisModel()
%CHEMOTAXISMODELV2 examines three methods for detecting gradients
%based on receptor-ligand binding:
%1. the gradient in bound receptors at the center of the cell
```

```
%2. the absolute difference in bound receptors across the cell
%3. the percent difference in bound receptors across the cell
%The results are plotted for each method along side the normalized values for
%easy comparison between three different source values of chemoattractant concentrations.
%An additional model is plotted using #1, above, with an exponential concentration

%Micropipette parameters
L0=[1 100 10000]';  %max ligand concentration
a0=4.5;          %radius of point source
z=9;             %distance between point source and plane

dcell=10;        %diameter of cell

x=[-500:1:500];    %defines the plane
r=sqrt(x.^2+z^2);  %distance from pt source for each pt in plane

L=2*L0*a0*(1./r);    %ligand concentration at each pt in plane
dLdx=-2*L0*a0*x./repmat(r.^3,size(L0,1),1); %x gradient of ligand at each point in plane

%Alternative chemoattractant concentration model
alpha=0.0008;
La=L0*exp(-alpha*r.^2);
dLadx=-2*alpha*La.*repmat(x,size(La,1),1);

%Receptor binding parameters
Rtot=1000;       %total number of receptors
Kd=10;           %dissociation constant

C=Rtot*L./(Kd+L);  %steady state number of bound receptors

%simple difference%%%%%%%%%%%%%%%%%%%%%%%%%%%%%%%%%%%%
dCdx=Rtot*Kd./((Kd+L).^2).*dLdx;
dCdxnorm=dCdx./repmat(max(dCdx')',1,size(x,2));
dC=dcell*dCdx; %absolute difference in bound receptors

%relative difference%%%%%%%%%%%%%%%%%%%%%%%%%%%%%%%%%%%%
dCnorm=dC./repmat(max(dC')',1,size(x,2));%normalized difference in bound receptors
dCpd=dC./C;      %percent difference in bound receptors
dCpdnorm=dCpd./repmat(max(dCpd')',1,size(x,2));   %normalized percent difference

%desensitization%%%%%%%%%%%%%%%%%%%%%%%%%%%%%%%%%%%%%%%%
n=1.2;   %hill coefficient
K=10;  %
R0=Rtot*L.^n./(K.^n+L.^n);
Cd=R0.*L./(Kd+L);
dCddx=-Rtot*K^n./((Kd+L).^2.*(K^n+L.^n).^2).*(Kd*K^n-(n-1)*Kd*L.^n-
n*L.^(n+1)).*L.*repmat((x./r.^2),size(L0,1),1);
dCd=dcell*dCddx;
dCdnorm=dCd./repmat(max(dCd')',1,size(x,2));

%alternative ligand model%%%%%%%%%%%%%%%%%%%%%%%%%%%%%%%%
dCadx=Rtot*Kd./((Kd+La).^2).*dLadx;
dCa=dcell*dCadx;
dCanorm=dCa./repmat(max(dCa')',1,size(x,2));

%figures%%%%%%%%%%%%%%%%%%%%%%%%%%%%%%%%%%%%%%%%%%%%%%%%
```

```
figure,plot(x,L,x,La,'LineWidth',2)
figure,plot(x,C,'LineWidth',2)

figure,plot(x,dC,'LineWidth',2),xlabel('X','FontSize',14),ylabel('\DeltaC','FontSize',14)
figure,plot(x,dCnorm,'LineWidth',2),axis([-40 0 0.7 1]),xlabel('X','FontSize',14),ylabel('Normalized
\DeltaC','FontSize',14)

figure,plot(x,dCpd,'LineWidth',2),xlabel('X','FontSize',14),ylabel('\DeltaC/C','FontSize',14)
figure,plot(x,dCpdnorm,'LineWidth',2),axis([-40 0 0.7 1]),xlabel('X','FontSize',14),ylabel('Normalized
\DeltaC/C','FontSize',14)

figure,plot(x,dCd,'LineWidth',2),xlabel('X','FontSize',14),ylabel('\DeltaC_d','FontSize',14)
figure,plot(x,dCdnorm,'LineWidth',2),axis([-50 0 -1 1]),xlabel('X','FontSize',14),ylabel('Normalized
\DeltaC_d','FontSize',14)

figure,plot(x,dCa,'LineWidth',2),xlabel('X','FontSize',14),ylabel('\DeltaC','FontSize',14)
figure,plot(x,dCanorm,'LineWidth',2),axis([-140 0 0.7 1]),xlabel('X','FontSize',14),ylabel('Normalized
\DeltaC','FontSize',14)
```

Model for chemotactic bias in multiple chemoattractant gradients

```
%function out = ChemotaxisModelMultiple()
%CHEMOTAXISMODELMULTIPLE examines gradient detection
%based on receptor-ligand binding in two chemoattractant gradients
%using an exponential model for the chemoattractant concentration and
%a steady state receptor-ligand binding scheme

%Micropipette parameters
L01=100;  %max ligand 1 concentration
xs1=100;  %ligand 1 location

L02=100;  %max ligand 2 concentration
xs2=-100;  %ligand 2 location

a0=4.5;          %radius of point sources
z=9;             %distance between point sources and plane

alpha=0.0008;

%Receptor binding parameters
Rtot1=1000;        %total number of receptors for 1
Kd1=10;            %dissociation constant for 1

Rtot2=1000;        %total number of recptors for 2
Kd2=10;            %dissociation constant for 2

dcell=10;          %diameter of cell

x=[-500:1:500];    %defines the plane
r1=sqrt((x-xs1).^2+z^2);  %distance from pt source 1 for each pt in plane
r2=sqrt((x-xs2).^2+z^2);  %distance from pt source 2 for each pt in plane

L1a=L01*exp(-alpha*r1.^2);
dL1adx=-2*alpha*L1a.*(x-xs1);
```

```
L2a=L02*exp(-alpha*r2.^2);
dL2adx=-2*alpha*L2a.*(x-xs2);

C1a=Rtot1*L1a./(Kd1+L1a);
C2a=Rtot2*L2a./(Kd2+L2a);

%bound receptor difference%%%%%%%%%%%%%%%%%%%%%%%%%%%%
dC1adx=Rtot1*Kd1./((Kd1+L1a).^2).*dL1adx;
dC1adxnorm=dC1adx./repmat(max(dC1adx')',1,size(x,2));
dC1a=dcell*dC1adx; %absolute difference in bound receptors

dC2adx=Rtot2*Kd2./((Kd2+L2a).^2).*dL2adx;
dC2adxnorm=dC2adx./repmat(max(dC2adx')',1,size(x,2));
dC2a=dcell*dC2adx; %absolute difference in bound receptors

%vector sum %%%%%%%%%%%%%%%%%%%%%%%%%%%%%%%%%%%%%%%%%%%
dCtota=dcell*(dC1adx+dC2adx);
dCtotanorm=dCtota./repmat(max(dCtota')',1,size(x,2));

%figures%%%%%%%%%%%%%%%%%%%%%%%%%%%%%%%%%%%%%%%%%%%%%%%
figure,plot(x,L1a,'b',x,L2a,'r','LineWidth',2),xlabel('X','FontSize',14),ylabel('L','FontSize',14)

figure,plot(x,dCtota,'LineWidth',2),hold on,plot(x,zeros(1,size(x,2)),'k--
'),xlabel('X','FontSize',14),ylabel('\DeltaC_t_o_t','FontSize',14)
plot(0,0,'ko','MarkerSize',10,'LineWidth',2),plot(-
100,0,'ko','MarkerSize',10,'MarkerFaceColor','k'),plot(100,0,'ko','MarkerSize',10,'MarkerFaceColor','k'),hol
d off
```

A.4 Simulation

Simulation of OU process in uniform concentration

```
function out = OUUniform()
%OUUniform Summary of this function goes here
%  Detailed explanation goes here
S=4.2/60;   %speed in um/min converted to um/second
P=6.5*60;       %persistence time in min converted to seconds

maxtime=60*60;     %minutes converted to seconds
dt=.001;
randn('seed',1);   %seed random number generator
numcells=10;

time=[0:dt:maxtime-dt;
v=zeros(maxtime/dt,2*numcells); %vx vy
xy=zeros(maxtime/dt,2*numcells);%x y

i=1;

nx=randn(maxtime/dt,1); %random numbers on x
ny=randn(maxtime/dt,1); %random number on y

while i*dt<maxtime
```

```
    %velocities
    v(i+1,1:2:end)=v(i,1:2:end)*(1-dt/P)+S*sqrt(dt/P)*nx(i); %vx
    v(i+1,2:2:end)=v(i,2:2:end)*(1-dt/P)+S*sqrt(dt/P)*ny(i); %vy

    %positions
    xy(i+1,1:2:end)=xy(i,1:2:end)+v(i,1:2:end)*dt;          %x
    xy(i+1,2:2:end)=xy(i,2:2:end)+v(i,2:2:end)*dt;          %y

    i=i+1;
end

xys=xy(1:10000:end,:);  %sample every  10 seconds

figure,plot(xys(:,1:2:end),xys(:,2:2:end),0,0,'ko','MarkerSize',15,'LineWidth',2)

U100nMUniformOU=xys;

save U100nMUniformOU U100nMUniformOU;

out=xys;
```

Simulation of OU process with chemotactic bias

```
%function out = OUbias(numcells)
%OUBIAS simulates OU process in 2D modified to include chemotactic bias term
%Chemotactic bias is based on receptor-ligand binding
%Each dimension has a separate white noise process

numcells=10;

%speed and persistence time
S=4.2/60; %um/s
P=6.5*60;  %s

%time parameters
maxtime=1000;   %s
dt=0.01;
randn('seed',2);
i=1;          %loop counter
time=[0:dt:maxtime-dt]';    %elapsed time

%parameters for concentration model
L0=10000;       %chemoattractant concentration in micropipette
xs=50;      %x location of source
ys=50;      %y location of source
zs=9;       %distance between source and chemotactic plane
a0=4.5;     %radius of source
alphaL=0.0008; %scaling factor on exponential gradient

%parameters for receptor-ligand binding
Rtot=1000;  %total number of receptors
Kd=10;      %dissociation constant
dcell=10;   %diameter of cell
thresh=10;  %minimum number of bound receptors across cell for gradient detection
kappa=.000002;   %chemotactic sensitivity
```

```
%preallocate arrays for velocities and positions in both dimensions
cellvxs=zeros(maxtime/dt,numcells);
cellvys=zeros(maxtime/dt,numcells);
cellxs=zeros(maxtime/dt,numcells);
cellys=zeros(maxtime/dt,numcells);

%preallocate receptor-ligand binding states
cellL=zeros(maxtime/dt,numcells);        %Ligand concentration
cellgradLx=zeros(maxtime/dt,numcells);    %ligand gradient in x direction
cellgradLy=zeros(maxtime/dt,numcells);    %ligand gradient in y direction
cellC=zeros(maxtime/dt,numcells);        %number of bound receptors
celldCdL=zeros(maxtime/dt,numcells);      %derivative of bound receptors wrt L
biasx=zeros(maxtime/dt,numcells);        %chemotactic bias in x
biasy=zeros(maxtime/dt,numcells);        %chemotactic bias in y
biasmag=zeros(maxtime/dt,numcells);      %magnitude of bias used to normalize

%precalculate random numbers
wnx=sqrt(dt)*randn(maxtime/dt,numcells);    %white noise in x component of velocity
wny=sqrt(dt)*randn(maxtime/dt,numcells);    %white noise in y component of velocity

i=1;   %loop counter

%main loop
while i*dt<maxtime
   cellL(i,:)=L0*exp(-alphaL*((cellxs(i,:)-xs).^2+(cellys(i,:)-ys).^2+zs^2)); %ligand concentration at
current position
   cellC(i,:)=Rtot*cellL(i,:)./(Kd+cellL(i,:));                    %number of bound receptors at current
position
   celldCdL(i,:)=Rtot*Kd./(Kd+cellL(i,:)).^2;                      %derivative wrt L
   cellgradLx(i,:)=-2*alphaL*cellL(i,:).*(cellxs(i,:)-xs); %current L gradient in x
   cellgradLy(i,:)=-2*alphaL*cellL(i,:).*(cellys(i,:)-ys); %current L gradient in y

   biasx(i,:)=dcell*celldCdL(i,:).*cellgradLx(i,:);   %x gradient in bound receptors
   biasx(i,:)=biasx(i,:).*(biasx(i,:)>thresh);        %check to see if threshold is met
   biasy(i,:)=dcell*celldCdL(i,:).*cellgradLy(i,:);   %y gradient in bound receptors
   biasy(i,:)=biasy(i,:).*(biasy(i,:)>thresh);        %threshold

   %this term is used to normalize the bound receptor gradient, the epsilon on end prevents divide by zero
error

%biasmag(i,:)=dcell*sqrt((celldCdL(i,:).*cellgradLx(i,:)).^2+(celldCdL(i,:).*cellgradLy(i,:)).^2)+0.000000
1;
   biasmag(i,:)=sqrt(biasx(i,:).^2+biasy(i,:).^2)+0.000000001;


   cellvxs(i+1,:)=cellvxs(i,:)*(1-dt/P)+S*sqrt(1/P)*wnx(i,:)+kappa*biasx(i,:)./biasmag(i,:);   %update x
velocity
   cellvys(i+1,:)=cellvys(i,:)*(1-dt/P)+S*sqrt(1/P)*wny(i,:)+kappa*biasy(i,:)./biasmag(i,:);   %update y
velocity
   cellxs(i+1,:)=cellxs(i,:)+cellvxs(i,:)*dt;        %update x position
   cellys(i+1,:)=cellys(i,:)+cellvys(i,:)*dt;        %update y position
   i=i+1;                                  %update counter
end

%figures
```

```
figure,plot(cellxs,cellys,'LineWidth',2),hold
on,plot(0,0,'go','MarkerFaceColor','g','MarkerSize',10),plot(xs,ys,'ro','MarkerFaceColor','r','MarkerSize',10),
hold off
axis([-100 100 -100 100])

%out=[time cellxs cellys];
```

Simulation of OU process in multiple chemoattractant gradients

```
%function out = OUbias(numcells)
%OUBIAS simulates OU process in 2D modified to include chemotactic bias term
%Chemotactic bias is based on receptor-ligand binding
%Each dimension has a separate white noise process

numcells=10;

%speed and persistence time
S=4.2/60; %um/s
P=6.5*60;  %s

%time parameters
maxtime=1000;  %s
dt=0.01;
randn('seed',2);
i=1;          %loop counter
time=[0:dt:maxtime-dt]';   %elapsed time

%parameters for concentration model
L01=100;      %chemoattractant concentration in micropipette
L02=100;
xs1=100;     %x location of source
ys1=50;     %y location of source
xs2=-100;
ys2=50;

zs=9;      %distance between source and chemotactic plane
a0=4.5;    %radius of source
alphaL=0.0008; %scaling factor on exponential gradient

%parameters for receptor-ligand binding
Rtot1=1000;  %total number of receptors
Kd1=10;     %dissociation constant
Rtot2=1000;
Kd2=10;

dcell=10;  %diameter of cell
thresh=10;  %minimum number of bound receptors across cell for gradient detection
kappa=.000002;  %chemotactic sensitivity

%preallocate arrays for velocities and positions in both dimensions
cellvxs=zeros(maxtime/dt,numcells);
cellvys=zeros(maxtime/dt,numcells);
cellxs=zeros(maxtime/dt,numcells);
cellys=zeros(maxtime/dt,numcells);
```

```
%preallocate receptor-ligand binding states
cellL1=zeros(maxtime/dt,numcells);        %Ligand concentration
cellgradL1x=zeros(maxtime/dt,numcells);    %ligand gradient in x direction
cellgradL1y=zeros(maxtime/dt,numcells);    %ligand gradient in y direction
cellC1=zeros(maxtime/dt,numcells);        %number of bound receptors
celldC1dL1=zeros(maxtime/dt,numcells);      %derivative of bound receptors wrt L

cellL2=zeros(maxtime/dt,numcells);        %Ligand concentration
cellgradL2x=zeros(maxtime/dt,numcells);    %ligand gradient in x direction
cellgradL2y=zeros(maxtime/dt,numcells);    %ligand gradient in y direction
cellC2=zeros(maxtime/dt,numcells);        %number of bound receptors
celldC2dL2=zeros(maxtime/dt,numcells);      %derivative of bound receptors wrt L

biasx=zeros(maxtime/dt,numcells);        %chemotactic bias in x
biasy=zeros(maxtime/dt,numcells);        %chemotactic bias in y
biasmag=zeros(maxtime/dt,numcells);       %magnitude of bias used to normalize

%precalculate random numbers
wnx=sqrt(dt)*randn(maxtime/dt,numcells);    %white noise in x component of velocity
wny=sqrt(dt)*randn(maxtime/dt,numcells);    %white noise in y component of velocity

i=1;   %loop counter

%main loop
while i*dt<maxtime
   cellL1(i,:)=L01*exp(-alphaL*((cellxs(i,:)-xs1).^2+(cellys(i,:)-ys1).^2+zs^2)); %ligand concentration at
current position
   cellC1(i,:)=Rtot1*cellL1(i,:)./(Kd1+cellL1(i,:));                    %number of bound receptors at
current position
   celldC1dL1(i,:)=Rtot1*Kd1./(Kd1+cellL1(i,:)).^2;                      %derivative wrt L
   cellgradL1x(i,:)=-2*alphaL*cellL1(i,:).*(cellxs(i,:)-xs1); %current L gradient in x
   cellgradL1y(i,:)=-2*alphaL*cellL1(i,:).*(cellys(i,:)-ys1); %current L gradient in y

   cellL2(i,:)=L02*exp(-alphaL*((cellxs(i,:)-xs2).^2+(cellys(i,:)-ys2).^2+zs^2)); %ligand concentration at
current position
   cellC2(i,:)=Rtot2*cellL2(i,:)./(Kd2+cellL2(i,:));                    %number of bound receptors at
current position
   celldC2dL2(i,:)=Rtot2*Kd2./(Kd2+cellL2(i,:)).^2;                      %derivative wrt L
   cellgradL2x(i,:)=-2*alphaL*cellL2(i,:).*(cellxs(i,:)-xs2); %current L gradient in x
   cellgradL2y(i,:)=-2*alphaL*cellL2(i,:).*(cellys(i,:)-ys2); %current L gradient in y

   biasx(i,:)=dcell*(celldC1dL1(i,:).*cellgradL1x(i,:)+celldC2dL2(i,:).*cellgradL2x(i,:));   %x gradient in
bound receptors
   biasx(i,:)=biasx(i,:).*(biasx(i,:)>thresh);       %check to see if threshold is met
   biasy(i,:)=dcell*(celldC1dL1(i,:).*cellgradL1y(i,:)+celldC2dL2(i,:).*cellgradL2y(i,:));   %y gradient in
bound receptors
   biasy(i,:)=biasy(i,:).*(biasy(i,:)>thresh);       %threshold

   %this term is used to normalize the bound receptor gradient, the epsilon on end prevents divide by zero
error

%biasmag(i,:)=dcell*sqrt((celldCdL(i,:).*cellgradLx(i,:)).^2+(celldCdL(i,:).*cellgradLy(i,:)).^2)+0.000000
1;
   biasmag(i,:)=sqrt(biasx(i,:).^2+biasy(i,:).^2)+0.000000001;
```

```
   cellvxs(i+1,:)=cellvxs(i,:)*(1-dt/P)+S*sqrt(1/P)*wnx(i,:)+kappa*biasx(i,:)./biasmag(i,:);   %update x
velocity
   cellvys(i+1,:)=cellvys(i,:)*(1-dt/P)+S*sqrt(1/P)*wny(i,:)+kappa*biasy(i,:)./biasmag(i,:);   %update y
velocity
   cellxs(i+1,:)=cellxs(i,:)+cellvxs(i,:)*dt;        %update x position
   cellys(i+1,:)=cellys(i,:)+cellvys(i,:)*dt;        %update y position
   i=i+1;                                  %update counter
end

%figures
figure,plot(cellxs,cellys,'LineWidth',2),hold
on,plot(0,0,'go','MarkerFaceColor','g','MarkerSize',10),plot(xs1,ys1,'ro',xs2,ys2,'ro','MarkerFaceColor','r','M
arkerSize',10),hold off
axis([-100 100 -100 100])

%out=[time cellxs cellys];
```

For reference

Not to be taken from the room.